Study of lattice, spin and charge dynamics in Cr- and Ni-based pnictide superconductors

Zur Erlangung des akademischen Grades eines
DOKTORS DER NATURWISSENSCHAFTEN (Dr. rer. nat)
von der KIT-Fakultät für Physik des
Karlsruher Instituts für Technologie (KIT)

genehmigte
Dissertation
von

M. Sc. Yi Yao

Tag der mündlichen Prüfung:	18. Dezember 2020
Referent:	Prof. Dr. Matthieu Le Tacon
Korreferent:	Prof. Dr. Jörg Schmalian

Contents

Abstract

Along the path to unravel the mysteries of unconventional superconductivity, the strong coupling effect between the electronic and lattice orders has proven itself to play a significant role in influencing the behavior of the superconductivity by effectively shifting the phase boundaries in the normal state of the material. Therefore, it is essential to obtain a deeper and more comprehensive understanding of these coupling effects in order to uncover the pairing mechanism of unconventional superconductors.

In this thesis work we have chosen two novel superconductors, *i.e.*, CrAs and $BaNi_2As_2$, which are strongly electron-lattice coupled systems, as our experimental subjects to study their rich dynamics by means of Raman scattering. CrAs shows a giant magnetoelastic effect across the first-order magnetic transition, which disappears upon pressure as superconductivity emerges. To shed more light on the responsible pairing mechanism, we were motivated to acquire a deeper understanding of the strong coupling of the lattice with the magnetic order in the normal state. To this aim, a detailed study of the lattice and magnetic excitations in single crystal CrAs by temperature-dependent Raman scattering was carried out.

$BaNi_2As_2$, on the other hand, is a nonmagnetic analogue of the well-studied $BaFe_2As_2$, and undergoes a first-order structural transition into a triclinic phase, where a commensurate charge density wave (C-CDW) develops. More importantly, a recently discovered unidirectional incommensurate charge density wave (IC-CDW) above the triclinic phase is a striking charge analogy of the spin density wave in the iron-based 122 superconductor, which raises the question whether electronic nematicity also plays an important role in the phase diagram of the Ni-based system. With the main objective to answer this question, we have performed detailed Raman scattering measurements on single crystals $BaNi_2(As,P)_2$ as functions of both temperature and doping.

Deutsche Zusammenfassung

In früheren Studien zur unkonventionellen Supraleitung hat sich gezeigt, dass der starke Kopplungseffekt zwischen der elektronischen Ordnung und der Gitterordnung die Phasengrenzen im Normalzustand eines Materials stark beeinflussen kann, was im Allgemeinen dann auch erhebliche Auswirkungen auf das Verhalten der Supraleitung hat. Daher ist es wichtig, ein tieferes und umfassenderes Verständnis dieser Kopplungseffekte zu erhalten, um den Paarungsmechanismus unkonventioneller Supraleiter zu vestehen.

In dieser Arbeit haben wir zwei neuartige Supraleiter, CrAs and $BaNi_2As_2$ - zwei stark elektronengittergekoppelte Systeme - zur Untersuchung ausgewählt. Das Ziel unserer Studie ist es ihre reiche Gitter- und elektronische Dynamik durch Ramanstreuung zu untersuchen. CrAs zeigt einen grossen magnetoelastischen Effekt in seinem magnetischen Phasenübergang erster Ordnung, welcher unter Druck verschwindet, wenn Supraleitung auftaucht. Um einen Einblick in den für die Supraleitung verantwortlichen Paarungsmechanismus zu erhalten, waren wir motiviert ein tieferes Verständnis der starken Kopplung des Gitters mit der magnetischen Ordnung im Normalzustand zu erhalten. Zu diesem Zweck wurde eine detaillierte Untersuchung der Gitter- und Magnetanregungen in einkristallinem CrAs durch temperaturabhängige Raman-Streuung durchgeführt.

$BaNi_2As_2$ ist hingegen ein nichtmagnetisches Analogon des gut untersuchten $BaFe_2As_2$ und durchläuft einen strukturellen Phasenübergang erster Ordnung in eine trikline Phase, in der sich eine kommensurable Ladungsdichtewelle (C-CDW) entwickelt. Noch wichtiger ist allerdings, dass eine kürzlich entdeckte unidirektionale inkommensurable Ladungsdichtewelle (IC-CDW) oberhalb der triklinen Phase eine bemerkenswerte Ladungsanalogie zu Spindichtewellen in eisenbasierten 122-Supraleiter darstellt, was die Frage aufwirft, ob elektronische Nematizität auch eine wichtige Rolle im Phasendiagramm des Ni-basierten Systems spielt. Mit dem Hauptziel diese Frage zu beantworten, haben wir detaillierte Raman-Streumessungen an $BaNi_2(As,P)_2$-Einkristallen als Funktionen sowohl der Temperatur als auch der Dotierung durchgeführt.

Chapter 1

Introduction

Ever since the discovery of superconductivity (SC) in mercury in 1911 [1], scientists have been dedicating years of hard work into explaining the mechanism behind such an exotic state, which is characterized by both zero resistivity and the Meissner effect. After almost half a century a rigorous theory was proposed by Bardeen, Cooper, and Schrieffer, in which electrons form Cooper pairs through a weak electron-phonon coupling (EPC) effect and behave as effective bosons. Multiple Cooper pairs are then allowed to occupy the same ground quantum state, which is responsible for the phenomenon of superconductivity [2, 3]. Superconducting systems that can be described by this BCS weak-coupling theory or later Eliashberg theory including stronger coupling [4] are thus categorized as conventional superconductors. As a contrast, unconventional superconductivity (UcS) is generally found in materials where the formation of Cooper pairs is believed to deviate from the EPC description [5, 6]. UcS was first discovered in the heavy-fermion systems [7, 8], and later in organic superconductors [9–12], then in the famous cuprates, in which T_c of 93 K was observed in $\mathrm{YBa_2Cu_3O_{7-\delta}}$ (YBCO) [13], completely refreshing the T_c record [5], and thus setting on the race of searching for higher T_c in cuprates with modified structures and also in other systems. Until now, many different UcS classes have been further uncovered, such as iron-based SCs, $\mathrm{Sr_2RuO_4}$, layered nitrides, *etc.* Although in these systems, EPC is believed to be no longer responsible for the superconductivity, numerous studies have shown that the coupling between the electronic and lattice degrees of freedom does play an important role in the normal state of the phase diagram, from which the unconventional superconductivity emerges.

Examples can be found in the well-studied high-T_c cuprates and iron-based superconductors (FeSCs.) It has been reported recently that in the underdoped YBCO, a novel charge density wave (CDW) state associated with a pronounced phonon softening can be induced in the normal state through lattice distortion [14]. This CDW order was found later to compete with SC below T_c, in agreement with other reported results [15–18]. In the phase diagrams of FeSCs, it has been demonstrated that charge doping is not the only factor that can determine the phase boundaries, isovalent substitution of the pnictogen atom can produce qualitatively the same effect on suppressing the coupled antiferromagnetism (AFM) and structural transition in the normal state, which leads to the emergence and enhancement of bulk superconductivity [19–23]. The phase diagrams of the iron-based ‘122’ system (AFe_2As_2 with A refers to alkaline-earth elements) is shown in Fig. 1.0.1.(a) as an example.

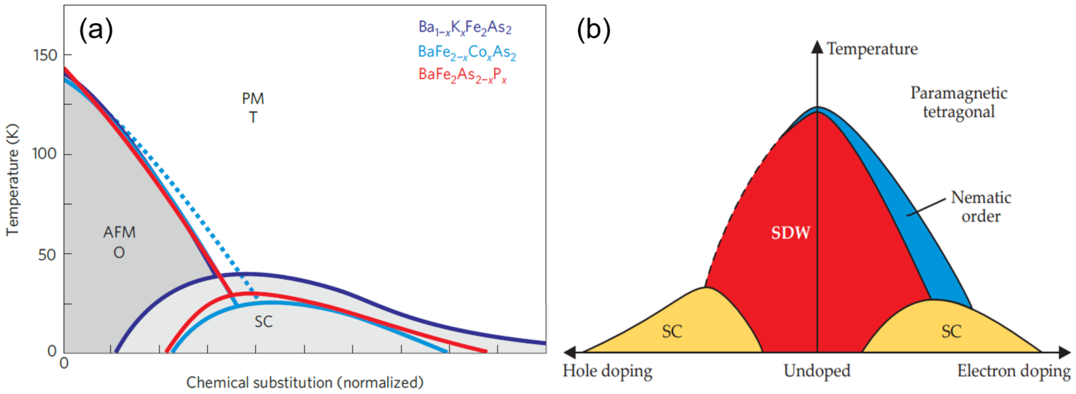

Figure 1.0.1: Schematic representation of the phase diagrams of $BaFe_2As_2$ system, with chemical substitutions of the alkaline-earth atom (Ba), transition-metal element (Fe) or pnictogen atom (As) by K, Co and P, respectively. The x-axis is normalized for different doping element. The dotted line represents the structural transition from tetragonal (T) to orthorhombic (O) in Co-doped system. The figure is taken from Ref. [23]. (b) Schematic phase diagram of the iron-based pnictides as functions of temperature and doping. Different phase and phase boundaries are marked correspondingly. The figure is taken from Ref. [24].

Another example that is more related to this thesis work is the electronic nematicity that is generally found in the iron-based ‘122’ and ‘1111’ (such as LaFeAsO) families. In these systems, the tetragonal to orthorhombic structural transition temperature T_s is often very close, if not the same, to the antiferromagnetic transition temperature T_N [25–27], which raises a question about the true origin of the lattice distortion. Theoretically, it has been suggested that these two transitions are coupled and the structural transition might not be driven by lattice degree of freedom, rather by electronic order which is related to the so-called electronic nematic phase [28–31]. In analogy to the nematic phase of liquid crystals, the nematicity, in this case, refers to a spontaneous broken rotational symmetry with the translational and time-reversal symmetry preserved. Differently from the scenario in isotropic liquid crystals, the associated order parameter in FeSCs is an Ising variable, pointing either along x or y directions. This order parameter becomes non-zero in the orthorhombic phase where the C_4 symmetry is broken. In the cases where $T_s > T_N$, the nematicity thus results in a finite temperature interval where the structural four-fold symmetry is lost while the system remains paramagnetic due to the preserved time-reversal symmetry. This nematic phase is represented by the blue region in Fig. 1.0.1.(b). The existence of nematicity has already been proven by numerous experiments including transport [32–36], optical conductivity [37–41], neutron scattering [42, 43], and angle-resolved photoemission spectroscopy (ARPES) [44, 45] measurements on mechanically detwinned crystals, where strong anisotropy of the electronic properties have been detected, with magnitude too large to be explained by lattice distortion alone, thus indicating a necessary involvement of electronic order. The electronic nematic susceptibility χ_{nem} can also be extracted directly by probing the nematic fluctuations in the high-temperature tetragonal phase. Softening of the shear modulus over a large temperature range above T_{nem}, which coincides with T_s, was found to be well described by phenomenological models for χ_{nem} [46, 47], implying the secondary character of the elastic degrees of freedom across the structural transition. Electronic Raman scattering is also proven to be an excellent tool to probe electronic nematicity with a characteristic signature of an enhanced quasi-elastic peak in the B_{2g} Raman spectra near T_{nem} [48], as will be introduced in Sec. 2.4. The electronic nematic order can have multiple microscopic origins. In FeSCs, both spin ordering and charge/orbital ordering can give rise to corresponding nematic orders. In the spin-fluctuation-driven nematic transition [34, 49], the spins of two Fe sublattices phase-lock, which breaks the C_4 symmetry with the system remains paramagnetic. One the other hand, with charge/orbital ordering, the occupations or the hopping matrix elements or both of them of the d_{xz} and d_{yz} orbitals of the Fe atom become nondegenerate [50, 51]. Disentangling these two scenarios experimentally is rather challenging as the emergence of one nematic order usually gives rise to the other, and they are all non-zero in the nematic phase. Regardless of the origin of the nematic order, it is generally found that upon doping, the superconducting critical temperature T_c increases as the nematic transition is suppressed in the same manner as the magnetic transition. Direct measurements of the orthorhombic distortion within the superconducting phase has revealed the competing relation between the two electronically driven orders for the same electronic states [52].

We can thus see from the above mentioned examples that the interplay between the lattice and electronic degrees of freedom has significant impacts on the normal state of the system, and understanding this coupling effect is crucial to fully unravel the paring mechanism of superconductivity. Therefore, in this thesis work, we have chosen the newly discovered Cr- and Ni-based superconductors, *i.e.*, CrAs and $BaNi_2As_2$, as our experimental probes, as they show exceptionally strong electron-lattice coupling effect, which is evident by dramatic structural distortions at the onset of the electronically ordered phases. CrAs exhibits a giant structural anomaly across the magnetic transition to a double-helical magnetic state [53–56]. This magnetic transition disappears under pressure as superconductivity emerges [57, 58]. The vicinity of SC to the magnetic order and the later found signatures of quantum critical behavior have suggested an unconventional pairing mechanism in this system [59]. $BaNi_2As_2$, on the other hand, can be viewed as a non-magnetic analogy to the well-studied $BaFe_2As_2$. Unlike the iron-based counterpart, $BaNi_2As_2$ undergoes a first-order structural transition from the tetragonal unit cell to triclinic phase [60, 61], with a unidirectional charge density wave (CDW) [62], instead of the unidirectional spin density wave (SDW), develops below the structural transition. In both systems, suppression of the density modulations induces or enhances superconductivity, thus raises fundamental questions of the phenomenologies of charge and spin orders and their relation to superconductivity [63]. Moreover, an incommensurate charge density wave (IC-CDW) has been recently discovered in $BaNi_2As_2$ [64], which is a striking charge analogy of the SDW in the iron-based 122 SCs, thus suggesting a possible existence of electronic nematicity in this system. To study such strongly-correlated systems Raman spectroscopy is an especially suitable tool, as it can simultaneously probe zone-center lattice and magnetic excitations as well as anisotropic charge density fluctuations.

In the next chapter, a detailed introduction of Raman spectroscopy is presented, with main focuses on three branches of this technique, *i.e.*, the phononic, magnetic, and electronic Raman scattering that are needed to understand the experimental data in the following chapters. Fundamental theories are illustrated, followed by typical experimental examples. Information regarding the data treatment and the specific instrumental set-up is also covered briefly. Raman scattering measurements on single crystals CrAs and phosphorus-doped $BaNi_2As_2$ are then presented in Chap. 3 and Chap. 4, respectively. Each chapter is composed of an introduction, which gives more complete background information regarding the system, experimental details, experimental results, followed by in-depth discussions, and finally conclusions and outlook. Some parts that are lengthy and not primarily essential for the context are put in the appendices, with the origin marked in the main text.

Chapter 2

Raman scattering

2.1 Overview of inelastic light scattering

When most of the incident light on a solid sample is reflected, transmitted or absorbed, a small part of it is scattered into different directions. When the monochromatic incident source is within the visible light range, the scattered light can have the same frequency as the incident light through the elastic or *Rayleigh* scattering, or different frequency through the inelastic or *Raman* scattering. Note that the inelastic part of the spectrum also includes the *Brillouin* scattering that results from scattering by sound waves and occurs close to the frequency of the incident light. As this is not concerned in our experiments, in the following parts we will restrict ourselves only to the case of Raman scattering.

The incident (i) and scattered (s) light is typically described by plane waves with frequency w_i, w_s, and wave vector $\mathbf{k}_i$, $\mathbf{k}_s$, respectively. During the scattering process, the energy and momentum must be conserved

$$\begin{aligned} \hbar w_s &= \hbar w_i \pm \hbar w \\ \mathbf{k}_s &= \mathbf{k}_i \pm \mathbf{q}, \end{aligned} \tag{2.1}$$

where w and $\mathbf{q}$ are the energy and momentum transferred to the system, respectively. The minus (plus) sign in Eq. 2.1 indicates the creation (annihilation) of an elementary excitation and an scattered photon with smaller (larger) energy than the incident photon, and is associated with the *Stokes* (anti-*Stokes*) process. Note that in Raman scattering experiments the incident light is in the visible range, the corresponding wave vector magnitude is then at the order of 10^7 cm^{-1}. By comparison, the maximum wave vector $|\mathbf{q_M}|$ for excitations in a crystal that lie in the Brillouin zone is at the order of π/d, where d is the lattice constant of several Å. Therefore, $|\mathbf{q_M}|$ is normally at the order of 10^{10} cm^{-1}, three orders of magnitude larger than the light-scattering excitation wave vectors, and $|\mathbf{q}|$ can usually be approximated to 0 in the first-order Raman scattering, *i.e.*, the first-order Raman scattering can only probe excitations near the Brillouin zone center.

A schematic spectrum of the scattered light is plotted in Fig. 2.1.1, where the contributions from both crystal vibrations (also known as phonon) and electronic

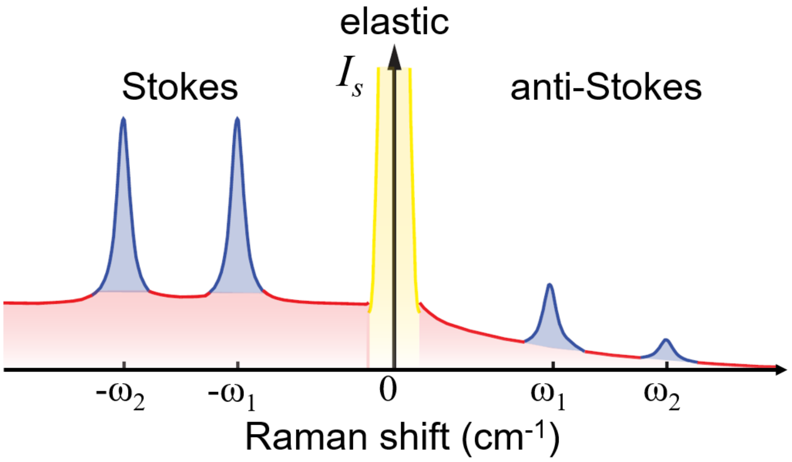

Figure 2.1.1: Schematic spectrum of the scattered light. The strong elastic line is at the center of the spectrum (yellow), the Raman spectrum with contributions from phonons (blue) and electrons (red) is shown in the Stokes and anti-Stokes channel. The figure is adapted from Ref. [65].

background are shown in the inelastic part. Several notes are required here. First, when the spectrum is being considered, it is standard to represent the intensity of the scattered light as a function of the *Raman shift*, which is the frequency shift of the scattered light with respect to the incident light. This Raman shift w is generally expressed in wavenumber cm^{-1}, which is obtained from $w = \frac{1}{\lambda_0} \pm \frac{1}{\lambda}$, where λ_0 and λ are the wavelength of the incident and scattered light, respectively. In addition, the elastically scattered light is typically $\sim 10^6$ - 10^8 times stronger than the inelastically scattered light, thus the use of an intense laser source is of high importance. Finally, the Stokes part and anti-Stokes part of the spectrum are related by the principle of detailed balance $I_{AS} = I_S \exp(-\hbar w/k_B T)$ [66], rendering two important indications. First, by measuring I_S/I_{AS} we can determine the sample temperature T, which can serve as a temperature calibration method. Second, at low temperatures, the anti-Stokes part of the spectrum has a much smaller strength than the Stokes part, therefore, it is usually much more convenient to measure just the latter. In this thesis, all Raman scattering measurements were focused only on the Stokes part of the spectrum.

Other than the inelastic scattering of light by lattice vibrations, the scattering by other excitations in solids, such as magnons, plasmons, excitons, can occur with the same mechanism [67]. In this chapter, we will briefly introduce the phononic [68–74], magnetic Raman scattering, and electronic Raman scattering, which are relevant to the results of the thesis. Information regarding the data treatment and instrumental set-up is also covered in the end.

2.2 Phononic Raman scattering

2.2.1 Classical description of phononic Raman scattering

We now consider an approach to the theory of Raman scattering in which both the electromagnetic radiation and the material system are treated classically. In a scattering experiment, electric dipole moments are induced by the incident monochromatic radiation, which is described by a plane wave $\mathbf{E}_i(\mathbf{k}_i, w_i) = \mathbf{E}_0\cos(\mathbf{k}_i \cdot \mathbf{r} - w_i t)$, where w_i is the frequency and $\mathbf{k}_i$ is the wave vector. All the individual atomic dipole moments combine to form a polarization vector which can be written as

$$\mathbf{P} = \varepsilon_0 \boldsymbol{\chi} \mathbf{E}_i, \tag{2.2}$$

where $\boldsymbol{\chi}$ is the electric susceptibility tensor of the material and ε_0 is the electric permittivity of free space. The susceptibility tensor describes the ability of a material to polarize in response to an applied electric field and is usually a function of the nuclear coordinates.

At finite temperatures, the atoms in a crystal vibrate. If the displacements $\mathbf{u}$ from their equilibrium positions $\mathbf{R_0}$ are small compared to the interionic spacing, the total potential energy of the crystal V can be expanded into a Taylor series around the equilibrium positions [75]

$$V(\mathbf{R}) = V(\mathbf{R}_0) + \left.\frac{\partial V(\mathbf{R})}{\partial \mathbf{u}}\right|_0 \mathbf{u} + \frac{1}{2}\left.\frac{\partial^2 V(\mathbf{R})}{\partial \mathbf{u}^2}\right|_0 \mathbf{u}^2 + \frac{1}{3!}\left.\frac{\partial^3 V(\mathbf{R})}{\partial \mathbf{u}^3}\right|_0 \mathbf{u}^3 + ... \tag{2.3}$$

$V(\mathbf{R}_0)$ is the equilibrium potential. The subscript “0” indicates to take the derivatives at the equilibrium positions, rendering the vanishing of the linear term and leaving the quadratic term as the first correction term to $V(\mathbf{R}_0)$. Within the *harmonic approximation*, the third and higher order terms in the expansion are neglected, therefore, the bond potentials can be approximated as parabolas and the restoring forces are proportional to the first power of the displacement. Any possible motions in the system can be described by its *normal modes.* In a normal mode, all the atoms oscillate sinusoidally with an angular frequency w and momentum $\mathbf{q}$, same as a harmonic oscillator, and the time-dependent displacement is given by

$$\mathbf{u} = \mathbf{u}_0\cos(\mathbf{q} \cdot \mathbf{r} - wt). \tag{2.4}$$

Due to the presence of lattice vibrations, the susceptibility tensor $\boldsymbol{\chi}$ is modulated, and the variation can be expressed by expanding each component $\chi_{\alpha\beta}$ of the tensor into a Taylor series with respect to the normal coordinates of vibration:

$$\chi_{\alpha\beta} = (\chi_{\alpha\beta})_0 + \sum_k \left(\frac{\partial \chi_{\alpha\beta}}{\partial \mathbf{u}_k}\right)_0 \mathbf{u}_k + \frac{1}{2}\sum_{k,l}\left(\frac{\partial^2 \chi_{\alpha\beta}}{\partial \mathbf{u}_k \partial \mathbf{u}_l}\right)_0 \mathbf{u}_k \mathbf{u}_l + ... \tag{2.5}$$

$(\chi_{\alpha\beta})_0$ is the value of $\chi_{\alpha\beta}$ at the equilibrium configuration, and $\mathbf{u}_k$, $\mathbf{u}_l$, ... are normal coordinates of vibration with vibrational frequencies w_k, w_l, ... The summations are taken over all normal coordinates. The subscript ”0” on the derivatives indicates that these are to be taken at the equilibrium configuration. If we assume the variation of the susceptibility in a vibration is only proportional to the first power of $\mathbf{u}_k$, based on the assumption that the displacements in lattice vibrations are very small in the harmonic oscillator approximation, and consider only one normal mode of vibration $\mathbf{u}_k$, we can then write Eq. 2.5 in the form

$$(\chi_{\alpha\beta})_k = (\chi_{\alpha\beta})_0 + \left(\frac{\partial \chi_{\alpha\beta}}{\partial \mathbf{u}_k}\right)_0 \mathbf{u}_k \tag{2.6}$$

As Eq. 2.6 is valid for all tensor components, we may write

$$\chi_k = \chi_0 + \left(\frac{\partial \chi}{\partial \mathbf{u}_k}\right)_0 \mathbf{u}_k = \chi_0 + \chi'_k \mathbf{u}_0 \mathrm{cos}(\mathbf{q} \cdot \mathbf{r} - wt) \tag{2.7}$$

Now we can calculate Eq. 2.2 using Eq. 2.7 and the expression for incident light as electric field, with the help of trigonometric identity:

$$\begin{aligned}
\mathbf{P} &= \varepsilon_0(\chi_0 + \chi'_k \mathbf{u}_0 \mathrm{cos}(\mathbf{q} \cdot \mathbf{r} - wt)) \cdot \mathbf{E}_0 \mathrm{cos}(\mathbf{k}_i \cdot \mathbf{r} - w_i t) \\
&= \varepsilon_0 \chi_0 \mathbf{E}_0 \mathrm{cos}(\mathbf{k}_i \cdot \mathbf{r} - w_i t) + \varepsilon_0 \chi'_k \mathbf{u}_0 \mathbf{E}_0 \mathrm{cos}(\mathbf{q} \cdot \mathbf{r} - wt) \mathrm{cos}(\mathbf{k}_i \cdot \mathbf{r} - w_i t) \\
&= \mathbf{P}_0 + \frac{1}{2} \varepsilon_0 \chi'_k \mathbf{u}_0 \mathbf{E}_0 \mathrm{cos}((\mathbf{k}_i - \mathbf{q}) \cdot \mathbf{r} - (w_i - w)t) \\
&+ \frac{1}{2} \varepsilon_0 \chi'_k \mathbf{u}_0 \mathbf{E}_0 \mathrm{cos}((\mathbf{k}_i + \mathbf{q}) \cdot \mathbf{r} - (w_i + w)t) \\
&= \mathbf{P}_0 + \mathbf{P}_{ind} \left[(\mathbf{k}_i - \mathbf{q}), (w_i - w)\right] + \mathbf{P}_{ind} \left[(\mathbf{k}_i + \mathbf{q}), (w_i + w)\right].
\end{aligned} \tag{2.8}$$

The first term in Eq. 2.8 corresponds to the polarization induced by the incident field in the absence of any lattice vibrations of the scattering medium, and the scattered light shows no change in frequency. The rest terms are the induced polarizations associated with Raman scattering with shifted frequencies and wave vectors. The second term with smaller frequency compared to w_i is the Stokes polarization, and the third term is the anti-Stokes polarization. These are results from the so-called first-order Raman scattering, as we only considered the first two terms in the susceptibility expansion in Eq. 2.5. When, for example, the third term $\frac{1}{2}\left(\frac{\partial^2 \chi_{ij}}{\partial \mathbf{u}_k \partial \mathbf{u}_l}\right)_0 \mathbf{u}_k \mathbf{u}_l$ which is quadratic in $\mathbf{u}$ is included, where $\mathbf{u}_k$, $\mathbf{u}_l$ are two normal modes with vibration frequency w_k and w_l, respectively, it will give rise to the second-order Raman scattering with scattering frequencies $w_i \pm w_k \pm w_l$. The intensity of the Raman lines associated to higher-order Raman scattering is, however, several orders of magnitude lower than that of the first-order scattering. This is usually true for phononic Raman scattering, but not necessary (and often not) the case for magnetic Raman scattering, as will be discussed in the next section.

The radiation energy emitted per unit time by the induced polarization can now be calculated according to the relation

$$\frac{d\Phi_s}{d\Omega} = \frac{w_s^4}{(4\pi)^2 \varepsilon_0 c_0^3} |\hat{\boldsymbol{\epsilon}}_s \cdot \mathbf{P}|^2, \tag{2.9}$$

where Φ_s is the scattered energy per unit area and unit time and $\hat{\boldsymbol{\epsilon}}_s$ is the unit vector parallel to the polarization of the scattered light selected by the point of observation. Replacing $\mathbf{P}$ using Eq. 2.2, we can write

$$\frac{d\Phi_s}{d\Omega} = \frac{w_s^4 \varepsilon_0}{(4\pi)^2 c_0^3} |\hat{\boldsymbol{\epsilon}}_s \cdot \boldsymbol{\chi} \cdot \hat{\boldsymbol{\epsilon}}_i|^2 \mathbf{E}_0^2. \tag{2.10}$$

The differential scattering cross section is defined as

$$\frac{d\sigma}{d\Omega} = \frac{1}{\Phi_i}\frac{d\Phi_s}{d\Omega} = \frac{w_s^4}{(4\pi)^2 c_0^4} |\hat{\boldsymbol{\epsilon}}_s \cdot \boldsymbol{\chi} \cdot \hat{\boldsymbol{\epsilon}}_i|^2, \tag{2.11}$$

with $\Phi_i = \varepsilon_0 c_0 \mathbf{E}_0^2$, the incident energy per unit area and per unit time. Replacing $\boldsymbol{\chi}$ by Eq. 2.6, we can write the differential cross section for Rayleigh and Raman scattering as

$$\frac{d\sigma_{Ray}}{d\Omega} = \frac{w_s^4}{(4\pi)^2 c_0^4} |\hat{\boldsymbol{\epsilon}}_s \cdot \boldsymbol{\chi}_0 \cdot \hat{\boldsymbol{\epsilon}}_i|^2, \quad \frac{d\sigma_{Ram}}{d\Omega} = \frac{w_s^4}{(4\pi)^2 c_0^4} \left| \hat{\boldsymbol{\epsilon}}_s \cdot \left[\left(\frac{\partial \boldsymbol{\chi}}{\partial \mathbf{u}} \right)_0 \mathbf{u} \right] \cdot \hat{\boldsymbol{\epsilon}}_i \right|^2, \tag{2.12}$$

respectively, where $\left(\frac{\partial \boldsymbol{\chi}}{\partial \mathbf{u}}\right)_0 \mathbf{u}$ is the *Raman tensor* $\boldsymbol{R}$. Experimentally, the scattering intensity of the Raman spectrum is proportional to the *spectral differential scattering cross section* $\frac{d^2\sigma}{d\Omega dw}$ which represents the probability of an incident photon to be inelastically scattered into a solid angle interval Ω and $\Omega + d\Omega$ with an energy interval w and $w + dw$ per unit time. We assume the observed Raman line will be a δ-function around the vibrational frequency w_v, following the definition of the spectral differential scattering cross section, we can then write

$$\frac{d^2\sigma}{d\Omega dw} = \frac{w_s^4}{(4\pi)^2 c_0^4} \left| \hat{\boldsymbol{\epsilon}}_s \cdot \boldsymbol{R} \cdot \hat{\boldsymbol{\epsilon}}_i \right|^2 \delta(w - w_v). \tag{2.13}$$

The scattering intensity associated with this vibrational frequency w_v is then

$$I \propto \left| \hat{\boldsymbol{\epsilon}}_s \cdot \boldsymbol{R} \cdot \hat{\boldsymbol{\epsilon}}_i \right|^2. \tag{2.14}$$

The classical theory gives the correct frequency dependence for Rayleigh and vibrational Raman scattering, it has, however, limitation over other types of excitations, such as spin waves. Also, the classical theory fails to give information on how the Raman tensor is related to the properties of the scattering medium. In the next part, we give a brief summary of the quantum mechanical theory of phononic Raman scattering, where both the material and radiation field are treated quantum mechanically.

2.2.2 Quantum mechanical theory of phononic Raman scattering

Within the quantum mechanical picture and the harmonic approximation, the energies of the lattice vibrations are quantized the same way as for a harmonic oscillator, *i.e.*, $E = \hbar w(n + \frac{1}{2})$, where n is an integer. Every energy quanta $\hbar w$ in a normal mode is called a *phonon*, and the integer n is the number of phonons in that normal mode.

Quantum mechanical treatment of the light scattering phenomena allows us to describe the inelastic Raman process with third-order (or higher) time-dependent perturbation theory. The Hamiltonian of the system then consists of three parts:

$$H = H_0 + H_{el-photon} + H_{el-phonon}, \tag{2.15}$$

where H_0 is the Hamiltonian of the unperturbed system, $H_{el-photon}$ describes the electron-photon interaction and $H_{el-phonon}$ describes the electron-phonon interaction. With the help of Fig. 2.2.1 we can then describe the Raman scattering process as follows:

- An electron is initially in a state $|i\rangle$ with energy E_i, and it is excited to a higher energy state $|m\rangle$ with energy E_m through the electron-photon interaction, described by Hamiltonian $H_{el-photon}$, by the absorption of a photon energy $\hbar w_i$.
- This electron is further scattered to another lower (higher) energy state $|n\rangle$ with energy E_n by creating (annihilating) a phonon with frequency w_q and momentum $q \approx 0$ (as explained in Sec. 2.1) through the electron-phonon interaction, described by Hamiltonian $H_{el-phonon}$. The creation and annihilation of a phonon corresponds to the Stokes and anti-Stokes process, respectively.
- Finally the electron decays back to the final state $|f\rangle$ (here we take the final state to be the same as the initial state) by emitting a second photon with energy w_s, again through the electron-photon interaction.

If we let $1/\tau$ be the transition rate between the initial and final states, the rate of removal of energy from the incident light by the scattering process can be expressed as $\hbar w_i/\tau$. Following the definition of cross section, it can be written as

$$\sigma = \frac{\hbar w_i}{I_i \tau}. \tag{2.16}$$

Thus, the spectral differential cross section, as well as the scattering intensity I_s is proportional to the transition rate $1/\tau$. To keep track of the various processes, we can make use of the Feynman diagrams. Note that phononic processes are symmetric under time reversal, therefore, the 3 steps described above can take place in arbitrary order, leading to 6 possible permutations. All diagrams for Raman process is given in Fig. 2.2.2 and is adapted from Ref. [76]. With the help from the Feynman diagram and the Fermi Golden Rule, we can then multiply the contribution from each vertex and calculate the transition rate $1/\tau$, often written as $\Gamma_{i\to f}$. We only write here the expression for the first scenario in Fig. 2.2.2, the

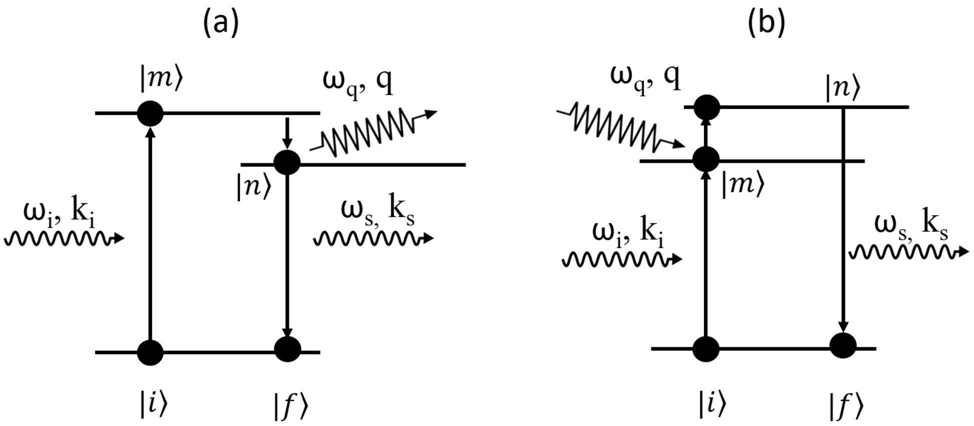

Figure 2.2.1: Schematic illustration of the first-order Raman scattering process. $|i\rangle$, $|f\rangle$ are the initial and final states, and $|m\rangle$, $|n\rangle$ are the intermediate states. (a) The demonstration of the Stokes process where a phonon is created. (b) The demonstration of the anti-Stokes process where a phonon is annihilated.

rest can be carried out similarly:

$$\begin{aligned}\Gamma_{i\to f} = \frac{2\pi}{\hbar}&\left|\sum_{m,n}\frac{\langle f|H_{el-photon}|n\rangle\langle n|H_{el-phonon}|m\rangle\langle m|H_{el-photon}|i\rangle}{[\hbar w_i - (E_m - E_i)][\hbar w_i - \hbar w_q - (E_n - E_i)]}\right|^2 \\ &\times \delta(\hbar w_i - \hbar w_q - \hbar w_s),\end{aligned} \tag{2.17}$$

where $\hbar w_i$, $\hbar w_s$ and $\hbar w_q$ are the energy of the incident photon, scattered photon and phonon, respectively. The δ-function ensures the energy conservation for the scattering process. Note that the intermediate states $|m\rangle$ and $|n\rangle$ do not need to be real. If, however, $|m\rangle$ or $|n\rangle$ is a real electronic state, and the incident or scattered photon energy matches the corresponding energy gap, then the photon absorption or emission process is resonant. Under this circumstance, the denominator in Eq. 2.17 turns to zero, and the transition rate would be strongly enhanced. This belongs to a special case called *resonant Raman scattering.*

Following Eq. 2.17, we now discuss the form of the two interaction Hamiltonians.

The incident electromagnetic radiation field can be quantized to vector-potential and electric-field operators

$$\mathbf{A}(\mathbf{r}) = \sum_k \sqrt{\frac{\hbar}{2\varepsilon_0 V w_{\mathbf{k}}}}\hat{\boldsymbol{\epsilon}}_{\mathbf{k}}\{a_{\mathbf{k}}\exp(i\mathbf{k}\cdot\mathbf{r}) + a^\dagger_{\mathbf{k}}\exp(-i\mathbf{k}\cdot\mathbf{r})\} \tag{2.18}$$

$$\mathbf{E}(\mathbf{r}) = i\sum_k \sqrt{\frac{\hbar w_{\mathbf{k}}}{2\varepsilon_0 V}}\hat{\boldsymbol{\epsilon}}_{\mathbf{k}}\{a_{\mathbf{k}}\exp(i\mathbf{k}\cdot\mathbf{r}) - a^\dagger_{\mathbf{k}}\exp(-i\mathbf{k}\cdot\mathbf{r})\}, \tag{2.19}$$

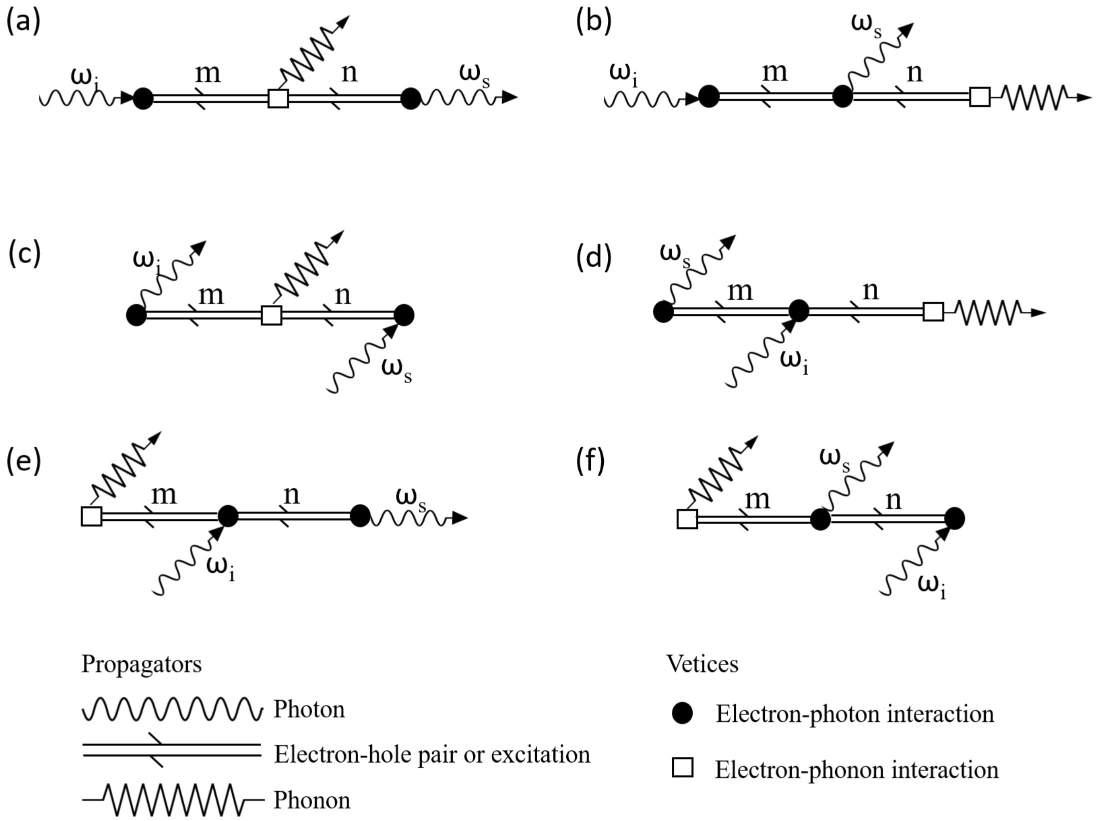

Figure 2.2.2: Feynman diagrams for the six scattering processes that contribute to the one-phonon Stokes Raman scattering. The figure is adapted from Ref.[76].

where the creation and destruction operators for a photon of wave vector $\mathbf{k}$, frequency $w_{\mathbf{k}}$, and polarization $\hat{\boldsymbol{\epsilon}}_{\mathbf{k}}$ satisfy

$$\begin{aligned} a^{\dagger}_{\mathbf{k}}|n_{\mathbf{k}}\rangle &= \sqrt{n_{\mathbf{k}}+1}|n_{\mathbf{k}}+1\rangle \\ a_{\mathbf{k}}|n_{\mathbf{k}}\rangle &= \sqrt{n_{\mathbf{k}}}|n_{\mathbf{k}}-1\rangle, \end{aligned} \tag{2.20}$$

with $n_{\mathbf{k}}$ the number of these photons. V is the volume of the scattering medium. In the presence of the electromagnetic field, the momentum operator of the jth electron of the scattering matter has to be substituted by $\mathbf{p}_j \rightarrow \mathbf{p}_j - e\mathbf{A}(\mathbf{r}_j)$. In the Coulomb gauge ($\nabla \cdot \mathbf{A} = 0$), the electron-photon Hamiltonian has the form

$$H_{el-photon} = \sum_j \left(-\frac{e}{m}\mathbf{p}_j \cdot \mathbf{A}(\mathbf{r}_j) + \frac{e^2}{2m}\mathbf{A}(\mathbf{r}_j) \cdot \mathbf{A}(\mathbf{r}_j) \right). \tag{2.21}$$

The summation index j runs over all electrons. Considering the electromagnetic fields that are not so strong, the second term in Eq. 2.21 can be neglected as it is quadratic in $\mathbf{A}$, therefore, the $\mathbf{p} \cdot \mathbf{A}$ term dominates the electron-photon coupling process.

Since the energy of the incident radiation is usually much larger than that of the phonon, direct coupling of the light to the vibrational excitation is very small, and the scattering process involving phonons is mainly depicted by the electron-phonon interaction, with the Hamiltonian given as

$$H_{el-phonon} = \sum_{\mathbf{k},\mathbf{q},\mu,\sigma} g^{\mu}_{\mathbf{k},\mathbf{q}} c^{\dagger}_{\mathbf{k}+\mathbf{q},\sigma} c_{\mathbf{k},\sigma} (b_{\mathbf{q},\mu} + b^{\dagger}_{-\mathbf{q},\mu}). \tag{2.22}$$

$g^{\mu}_{\mathbf{k},\mathbf{q}}$ is the electron-phonon interaction vertex with $\mathbf{k}$, $\mathbf{q}$ the wave vector of the electron and the phonon, respectively. $c^{\dagger}_{\mathbf{k}+\mathbf{q},\sigma}$ ($b^{\dagger}_{\mathbf{q},\mu}$) and $c_{\mathbf{k},\sigma}$ ($b_{\mathbf{q},\mu}$) are the creation and annihilation operators of electrons (phonons). μ denotes the phonon branch and σ represents the spin states of the electron.

Eq. 2.17 cannot be evaluated numerically for detailed comparison with the experiment, but it can still predict the variation of the cross section as the experimental parameters are changed, allowing us to have a deeper understanding of the connection between material properties and the experimental results.

2.2.3 Raman mode symmetry

When taking a look back at Eq. 2.14, we can clearly see two criteria for successful detection of any intensity in the Raman scattering spectrum. First, the derivative of the susceptibility tensor, corresponding to one normal mode of vibration, at the equilibrium configuration is not zero [69], and second, at least one combination of the incident and scattered light polarizations ($\hat{\epsilon}_i$ and $\hat{\epsilon}_s$) can result in a non-zero value of the product in Eq. 2.14 [71]. When both conditions are met, this normal mode is then Raman active.

Each normal mode of vibration consists of stretches, bends, and other displacements that form a basis for an irreducible representation in the character table of the point group with the same symmetry as that of the crystal [77, 78]. Irreducible representations are typically denoted by Mulliken symbols, and the meaning of each symbol can be found in Tab. 2.1. The complete set of normal modes can be divided into three categories: Raman active, infrared active, or silent. When the system is invariant under spatial inversion, the Raman-active modes are symmetric with $\chi_{\alpha\beta} = \chi_{\beta\alpha}$ (the susceptibility derivative has the same property), while infrared-active modes are antisymmetric with $\chi_{\alpha\beta} = -\chi_{\beta\alpha}$. This leads to an important rule of mutual exclusion, in that vibrational modes are not allowed to be Raman- and infrared-active at the same time, which will be of great importance for the interpretation of Raman scattering spectra in Chapter. 4.

There are several methods to analyze the unit cell and determine the selection rules of the first-order phonon spectrum ($q \approx 0$). Detailed elaboration and further references can be found in Ref. [79]. In our work, we used *nuclear site group analysis* to determine active Raman modes of the scattering systems. The method is straight forward, and can be followed by three steps:

1. Identify the space group of the crystal under investigation and subsequently the position and site symmetry of each atom in the unit cell.

Table 2.1: The meaning of Mulliken symbols for irreducible representation notation

Mulliken Symbols	Meaning
A	1D irreducible representation, symmetric with respect to the principle axis of symmetry
B	1D irreducible representation, antisymmetric with respect to the principle axis of symmetry
E	2D irreducible representation, doubly degenerate
g	symmetric with respect to a center of symmetry
u	antisymmetric with respect to a center of symmetry
For 1D irreducible representations	
Subscript 1	symmetric with respect to the most important perpendicular C_2 axis (if none, then to σ_v)
Subscript 2	antisymmetric with respect to the most important perpendicular C_2 axis (if none, then to σ_v)
For B irreducible representations, if there are 3 equally important perpendicular C_2 axes	
Subscript 1	symmetric with respect to the 1st C_2 axis
Subscript 2	symmetric with respect to the 2nd C_2 axis
Subscript 3	symmetric with respect to the 3rd C_2 axis

2. Derive the irreducible representations of the zone center phonons from the occupied atomic sites in the unit cell.
3. Based on the Raman tensor of each irreducible representation, Raman active normal modes can be determined.

In Chap. 3 and Chap. 4, we apply this method on CrAs and $BaNi_2As_2$, respectively, and plot out the corresponding Raman modes.

2.2.4 Phonon interactions

Within the harmonic approximation, the normal modes are the eigenvectors of the Hamiltonian for the ions of the crystal and have an infinite lifetime τ, which should be reflected by a δ-function-like lineshape based on the inversion relation between the phonon full-wave-half-maximum (FWHM) or more simply the phonon linewidth (Γ) and the phonon lifetime, $\Gamma \sim 1/\tau$. Experimental results, on the other side, show that phonons have finite linewidth, and it changes under external impacts, such as temperature or pressure. These phenomena are, in fact, results of the interactions between the zone-center optical phonon and other orders, such as other phonons, magnons, electrons, *etc.* In order to describe these phonon interactions one must go beyond the harmonic approximation and take higher oder terms of the potential energy expansion (Eq. 2.3) and interaction terms into account.

This can be treated as a perturbation effect in the framework of perturbation theory, where an interaction V is added to the unperturbed solvable H_0 to form the full Hamiltonian H of the system. The response of the system is expressed with Green's functions. For more detailed information one can refer to Ref. [67, 80]. The zero temperature bare ($V = 0$) phonon Green's function can be written as

$$D^{(0)}(\mathbf{q}, t_1 - t_2) = -i\langle 0\,|T\{A_{\mathbf{q}}(t_1)A_{\mathbf{q}}(t_2)\}|\,0\rangle, \tag{2.23}$$

where the phonon operators $A_{\mathbf{q}}$ are given by $A_{\mathbf{q}} = b_{\mathbf{q}} + b^{\dagger}_{-\mathbf{q}}$ with $b_{\mathbf{q}}$, $b^{\dagger}_{-\mathbf{q}}$ the annihilation and creation operators of phonon with momentum $\mathbf{q}$. $|0\rangle$ is the known ground state of the Hamiltonian H_0, and T is the time-ordering operator which places the operators with later times to the left and additionally adds a minus sign for each interchange of two fermionic operators. By applying Fourier transformation, we can express the Green's function in k-space as following

$$D^{(0)}(\mathbf{q}, w) = \frac{1}{w - w_{\mathbf{q}} + i\delta} - \frac{1}{w + w_{\mathbf{q}} - i\delta} = \frac{2w_{\mathbf{q}}}{w^2 - w_{\mathbf{q}}^2 + i\delta}, \tag{2.24}$$

where $\delta = 0^+$ is introduced as a convergence factor. This function has two poles, one at $w = w_{\mathbf{q}}$, slightly shifted to lower frequency, and the other at $w = -w_{\mathbf{q}}$, slightly shifted to higher frequency. Therefore, the bare phonon Green's function gives the phonon frequency in the unperturbed system.

When $V \neq 0$, the phonons interact with the environment, and the resulting phonon Green's function $D(\mathbf{q}, w)$ is given by the following *Dyson equation*:

$$D(\mathbf{q}, w) = D^{(0)}(\mathbf{q}, w) + D^{(0)}(\mathbf{q}, w)\Pi(\mathbf{q}, w)D^{(0)}(\mathbf{q}, w), \tag{2.25}$$

where phonon self-energy $\Pi(\mathbf{q}, w)$ is the sum of all interaction terms of different origins. Phonon self-energy is a complex function of the phonon frequency w: $\Pi(\mathbf{q}, w) = \Delta(w) - i\Gamma(w)$. Taking this form back into Eq. 2.25 gives

$$D(\mathbf{q}, w) = \frac{1}{w - (w_{\mathbf{q}} + \Delta(w)) + i(\delta + \Gamma(w))} + \frac{1}{w + (w_{\mathbf{q}} - \Delta(w)) - i(\delta - \Gamma(w))}. \tag{2.26}$$

From Eq. 2.26 we can see that the real part $\Delta(w)$ is associated with the frequency renormalization due to phonon interaction, and the imaginary part $\Gamma(w)$ describes the broadened phonon linewidth resulted from the now finite phonon lifetime. These two parts are related by Kramers-Kronig relations.

As mentioned before, phonons can interact with the environment through other phonons, electrons, or spins. The corresponding interaction Hamiltonian enters Eq. 2.26 and changes the phonon frequency and linewidth accordingly. An important and feasible tuning parameter of the interaction strength is temperature, therefore, it is very common to study the temperature dependence of the phononic

Raman spectrum. In the following part, we briefly introduce two types of interactions that are relevant to our work which are phonon-phonon interaction and electron-phonon interaction.

Phonon-phonon interaction

The main reason for the finite phonon linewidth is the so-called phonon-phonon interaction, which leads to the decay of the zone-center optical phonon to other two or more phonons. The decay process follows the energy and momentum conservation laws stated in Eq. 2.1. The anharmonic effect is described by the phonon self-energy (SE) mentioned above, where the real part $\Delta(w)$ is responsible for the temperature dependence of the phonon frequency, and the imaginary part $\Gamma(w)$ is responsible for the temperature dependence of the phonon linewidth.

Under the effect of the anharmonic interactions, the harmonic frequency w_0 is changed to [81]

$$w(\Omega) = w_0 + \Delta(\Omega) + i\Gamma(\Omega). \tag{2.27}$$

The Stokes Raman peak then has the form

$$I_s(\Omega) \propto \frac{\Gamma(\Omega)/2}{(w_0 + \Delta(\Omega) - \Omega)^2 + (\Gamma(\Omega)/2)^2} \times (n(\Omega) + 1), \tag{2.28}$$

where $n(\Omega)$ is the Bose-Einstein thermal occupation number $1/(\exp(\hbar w/k_B T) - 1)$. The determination of the phonon SE requires to solve the complicated interaction matrix and thus invoked several methods of approximation to simplify the calculation process [81–83]. One of the wildly accepted approaches was proposed by Klemens [82], where he assumes that the zone-center optical phonon with frequency w_0 at T = 0 decays into two acoustical phonons with opposite $\mathbf{q}$ belonging to the same branch. The assumption that the two acoustical phonons belong to the same branch leads directly to $w(\mathbf{q}) = w(-\mathbf{q}) = w_0/2$. A schematic representation of the decay process can be found in Fig. 2.2.3.

The resulting expressions for the phonon frequency w_{ph} and phonon linewidth Γ_{ph} can be written as:

$$\begin{aligned} w_{ph}(T) =& w_0 - A\left(1 + \frac{2}{\exp(\hbar w_0/2k_B T) - 1}\right) \\ \Gamma_{ph}(T) =& \Gamma_0 + \Gamma\left(1 + \frac{2}{\exp(\hbar w_0/2k_B T) - 1}\right), \end{aligned} \tag{2.29}$$

where A and Γ are positive constants, w_0 is the bare phonon frequency, and Γ is the linewidth of the spectrum. Γ_0 is a residual linewidth (independent of temperature) arising from, *e.g.*, impurities in the sample. Based on these expressions we can follow the temperature dependence of the phonon frequency and linewidth. The general trend is illustrated in Fig. 2.2.4, where the phonon frequency increases, while the phonon linewidth decreases, with decreasing temperature. At low temperatures, both values show little variation.

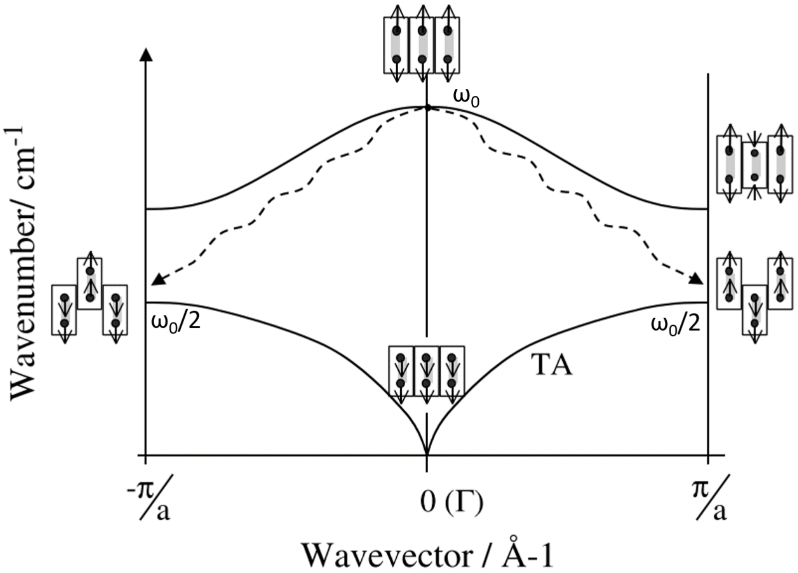

Figure 2.2.3: Schematic representation of the anharmonic decay of the zone-center optical phonon. The optical phonon of frequency w_0 decays to two acoustical phonons with opposite $\mathbf{q}$ from the same branch. The frequency of the acoustical phonons is $w_0/2$. The small figures beside the phonon dispersive curves are illustrations of the phonons of a linear assembly of diatomic molecules where atoms vibrate perpendicularly to the axis of the chain. The figure is taken from Ref. [75].

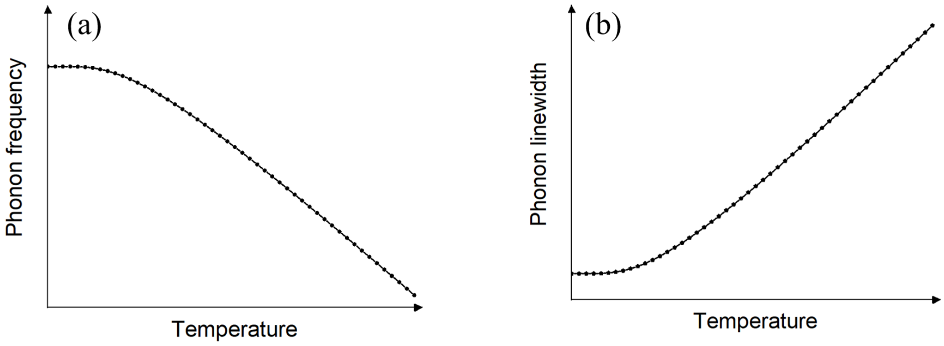

Figure 2.2.4: Schematic illustrations of the (a) phonon frequency and (b) phonon linewidth according to the Klemens decay expression. Following the anharmonic decay, the phonon frequency increases, while the phonon linewidth decreases, with decreasing temperature. Both values enter a platform at low temperatures.

Electron-phonon coupling

In addition to the phonon-phonon interaction where the optical phonon decays into other phonons, electron-phonon interaction provides an important decay channel where the phonon decays into electronic excitations. For systems which consist of one discrete phononic state ϵ_s close to one or more electronic continuum transitions, interference effects may occur and lead to not only renormalization of the phonon frequency but more importantly, distortion of the symmetric lineshape (typically Lorentzian as described by Eq. 2.28), thus resulting in an asymmetric emission lineshape, known as the *Fano lines*. Detailed derivation can be found in Ref. [84]. An illustration of the energy schedule is shown in Fig. 2.2.5.

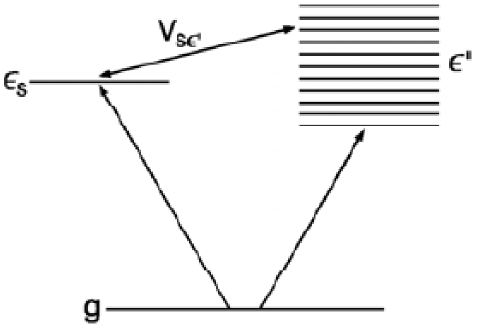

Figure 2.2.5: Schematic description of the interference between excitations from a ground state g to a single phononic state ϵ_s and to an electronic continuum ϵ'. The figure is taken from Ref. [85].

The superposition state consisting of the discrete phononic state ϵ_s (wavefunction ψ_s) and an electronic continuum ϵ' (wavefunction $\psi_{E'}$) can be written as:

$$\Psi_E = a\varphi_s + \int dE' b_{E'}\psi_{E'}, \tag{2.30}$$

where a and $b_{E'}$ are functions of E. The probability of excitation from the ground state g to the superposition state Ψ_E can thus be calculated by matrix $\langle \Psi_E |T| g\rangle$ where T is the transition operator. It is found that

$$|\langle \Psi_E |T| g\rangle|^2 \propto \frac{(q+\epsilon)^2}{1+\epsilon^2}, \tag{2.31}$$

where q indicates the strength of the electron-phonon coupling and is called the Fano asymmetry parameter. $\epsilon = (E - E_s - F(E))/\pi |V_E|^2$, with E_s the energy of the phononic state ϵ_s and $F(E)$ a quantity representing a shift of the phonon frequency. $\pi |V_E|^2$ equals to $\Gamma/2$, where $|V_E|^2$ is an index of the interaction strength, therefore, the phonon linewidth can also reflect the electron-phonon coupling strength. We can now describe the Fano lines by

$$I_F = C\frac{(q+\epsilon)^2}{1+\epsilon^2}. \tag{2.32}$$

An example of Fano lineshape with different values of the asymmetry parameter q is shown in Fig. 2.2.6. We can see that the smaller the q is, the more asymmetric the lineshape is, when q approaches to ∞, the Fano line recovers the Lorentzian shape. Therefore, commonly $1/q^2$ is used to reflect the line shape asymmetry.

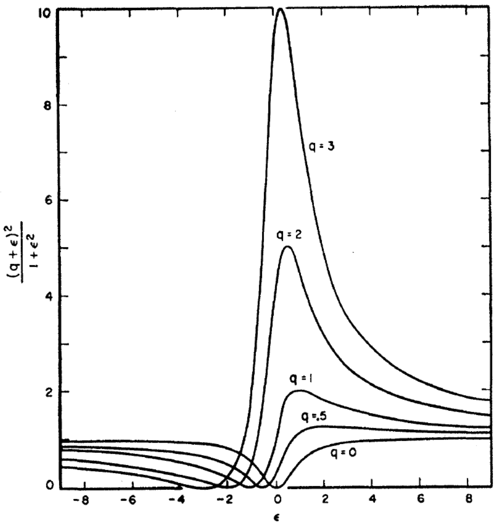

Figure 2.2.6: Fano lines with different values of the asymmetry parameter q. The smaller the q is, the more asymmetric the lineshape is. The figure is taken from Ref. [84].

2.3 Magnetic Raman scattering

In addition to lattice vibration, magnetic excitations can also be Raman active, which generally can be classified into two types—one-magnon and two-magnon excitations. One of the most wildly used theoretical approaches in magnetic Raman scattering is the Fleury-Loudon (FL) mechanism [67, 68, 86], which will be introduced here briefly.

Magnons are quantized excitations of a system from its magnetic ground state, which in a ferromagnetic system is realized when all spins are fully aligned, supposedly along the z axis, at zero temperature. At higher temperatures, each thermally excited magnon reduces the total z component of the spins by one. The magnetic state of the crystal can then be described by the number of excited magnons $n_{\mathbf{k}}$ with wave vector $\mathbf{k}$. We can write the spin Hamiltonian for a ferromagnetic system in second-quantized notations with the magnon creation and destruction operators $\alpha_{\mathbf{k}}$, $\alpha_{\mathbf{k}}^{\dagger}$ as

$$H = \sum_{\mathbf{k}} E_{\mathbf{k}} \alpha_{\mathbf{k}} \alpha_{\mathbf{k}}^{\dagger}, \tag{2.33}$$

where $E_{\mathbf{k}}$ is the magnon energy

$$E_{\mathbf{k}} = \hbar w_{\mathbf{k}} = g\beta[H_E(1-\gamma_{\mathbf{k}}) + H_0], \tag{2.34}$$

and

$$\gamma_{\mathbf{k}} = \frac{1}{Z} \sum_{j} \exp[i\mathbf{k} \cdot (\mathbf{r}_i - \mathbf{r}_j)]. \tag{2.35}$$

$g\beta$ is the gyromagnetic ratio. H_0 is a static external field pointing along the z axis. H_E is the exchange field whose effect is assumed to be restricted within Z nearest neighbors (as the sum in Eq. 2.35), and is given by $g\beta H_E = 2JZS$. J is the nearest-neighbor exchange coupling strength. Note that $\gamma_{\mathbf{k}}$ only depends on the geometric arrangement of the magnetic ions in the crystal and equals to unity at zone center ($\mathbf{k} = 0$), leading to $E_0 = g\beta H_0$. Of course, there are other factors contributing to the zone center magnon frequency such as dipole-dipole interaction or impurities [87].

Eq. 2.33 can be extended to antiferromagnetic systems. What is different is that in an antiferromagnet spins order in two sublattices with opposite directions, supposedly along $\pm z$ axis, and each magnon can either reduce or increase the spin z component of the entire crystal by one. These two types of magnon are shown in Fig. 2.3.1. The spin Hamiltonian is thus given by

$$H = \sum_{\mathbf{k}} \left(E_{\uparrow\mathbf{k}} \alpha_{\uparrow\mathbf{k}} \alpha^{\dagger}_{\uparrow\mathbf{k}} + E_{\downarrow\mathbf{k}} \alpha_{\downarrow\mathbf{k}} \alpha^{\dagger}_{\downarrow\mathbf{k}} \right), \tag{2.36}$$

where

$$w_{\downarrow\mathbf{k}} = w_{\mathbf{k}} + g\beta H_0, \quad w_{\uparrow\mathbf{k}} = w_{\mathbf{k}} - g\beta H_0, \tag{2.37}$$

and

$$w_{\mathbf{k}} = g\beta\sqrt{(H_E + H_A)^2 - (\gamma_{\mathbf{k}} H_E)^2}. \tag{2.38}$$

H_A is an anisotropy field that acts on the two sublattices in opposite directions. It is clear that the two types of magnons give the same energy in the absence of H_0, and the frequency of the zero-wavevector magnon is then $w_0 = g\beta\sqrt{H_A(2H_E + H_A)}$.

Note that both sublattices take part in both types of magnons. The degree of participation of the sublattices is described by two functions $\mu_{\mathbf{k}}$ and $v_{\mathbf{k}}$, respectively, and each magnon changes the total spin of one sublattice by $\pm\mu^2_{\mathbf{k}}$ and of the other by $\pm v^2_{\mathbf{k}}$. Thus the requirement to change the total spin z component by $\pm$ 1 is simply $\mu^2_{\mathbf{k}} - v^2_{\mathbf{k}} = 1$.

One-magnon excitation

One-magnon excitation can be simplified as a single spin-flip and belongs to the first-order Raman scattering, where the magnon energy and momentum follows Eq. 2.1, *i.e.*, wave vector $\mathbf{k}$ is close to Brillouin zone center. Two interaction mechanisms were proposed for the single magnon excitation in Raman scattering. One considers direct magnetic-dipole interaction between the spins and the electromagnetic field introduced by radiation source with the Hamiltonian $H = -g\beta \sum_i \mathbf{H}_i \cdot \mathbf{S}_i$, where i indicates ionic site. The cross section calculated with this Hamiltonian is, however, too small compared to the experimentally observed results, and is usually neglected [88].

The more efficient scattering mechanism is provided by Elliott and Loudon [89], in which they proposed that the scattering of light by magnons occurs through the electric-dipole coupling of the radiation to the crystal, which relies on the

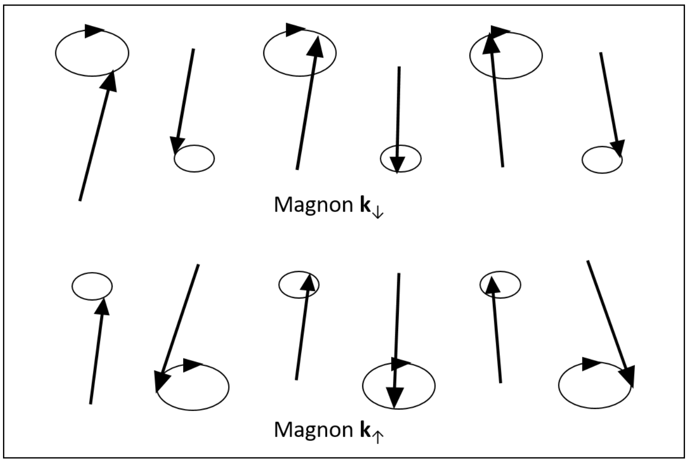

Figure 2.3.1: Schematic representations of the two types of antiferromagnetic magnons. The figure is adapted from Ref. [68].

indirect coupling of the spins and orbital motions. The magnetic ground state is assumed to have zero or quenched orbital angular momentum. An illustration for a ferromagnetic system is shown in Fig. 2.3.2. The transitions occur between the ionic ground state of spin S and zero orbital momentum L, which is split by an external field H_0, and the excited P state with the same spin S and $L = 1$, which is split by spin-orbital coupling $\lambda\mathbf{L}\cdot\mathbf{S}$. Fig. 2.3.2 shows pairs of the allowed electric-dipole transitions from $S^z = S$ to $S^z = S - 1$ component of the orbital ground state.

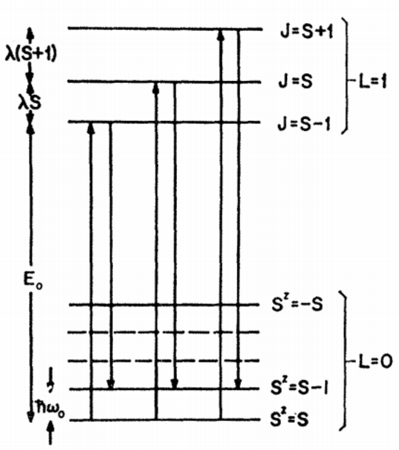

Figure 2.3.2: Schematic representation of the energy states in the electric-dipole Raman scattering mechanism. The figure is taken from Ref. [86]

Detailed calculations have already been well documented [68, 86], and the obtained differential cross section is given by

$$\frac{d\sigma}{d\Omega} \propto (n_{w_0} + 1)\Gamma^2|\epsilon_i^z\epsilon_s^+ - \epsilon_i^+\epsilon_s^z|^2. \tag{2.39}$$

$\Gamma \propto \lambda \cdot \langle \text{transition matrix} \rangle$, where λ is the spin-orbit coupling coefficient, and ϵ_i, ϵ_s are the polarizations of the incoming and scattered photon ($\epsilon^+ = \epsilon^x + i\epsilon^y$). $n_{w_0} + 1$ is the magnon thermal factor. Note that the antisymmetry of the polarizations in Eq. 2.39 is resulted from the assumption that the excited magnon imposes no change on the orbital states of the magnetic ground state, and therefore, may not hold in more general cases.

The expression for ferromagnet can be generalized to antiferromagnet systems. With contributions from both sublattices, the obtained cross section for the ↓ magnon is then

$$\frac{d\sigma}{d\Omega} \propto (n_{\downarrow w_0} + 1)\Gamma^2(\mu_0 + \upsilon_0)^2 |\epsilon_i^z \epsilon_s^+ - \epsilon_i^+ \epsilon_s^z|^2, \tag{2.40}$$

and for the ↑ magnon

$$\frac{d\sigma}{d\Omega} \propto (n_{\uparrow w_0} + 1)\Gamma^2(\mu_0 + \upsilon_0)^2 |\epsilon_i^z \epsilon_s^- - \epsilon_i^- \epsilon_s^z|^2. \tag{2.41}$$

With typical crystal lattice parameters, the magnon cross section for a ferromagnet is calculated to be comparable or smaller than the vibrational cross section, while an antiferromagnet seems to be a poorer scatter due to the opposite sign between μ_0 and υ_0. These calculations, however, have a wide range of uncertainty[68, 86]. Experimentally single magnons are usually characterized by sharp low-energy peaks in long-range magnetically ordered systems [90–93] as shown in Fig. 2.3.3, labeled as M1, M2. The higher energy features (2M) are associated to the second-order magnetic scattering, which will be introduced next.

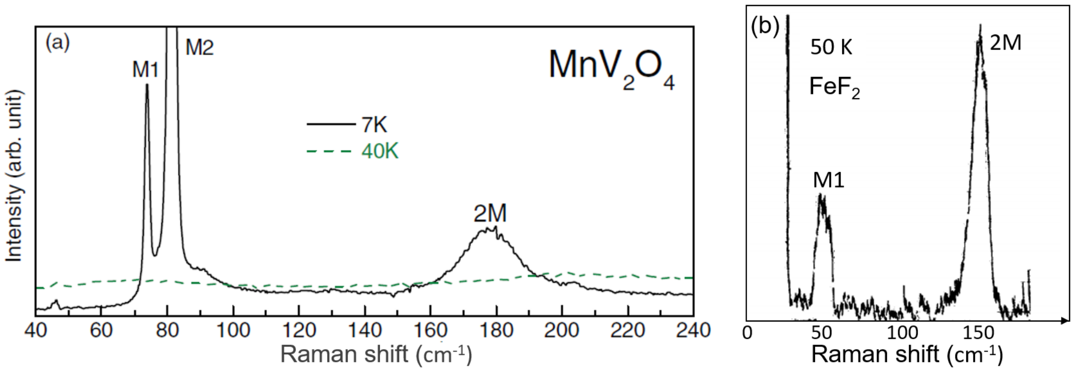

Figure 2.3.3: First- and second-order magnetic scatterings in (a) MnV_2O4 and (b) FeF_2. The single magnons are sharp peaks at low energies, marked as M1, M2, whereas the double magnons are broader and at higher energies, labeled as 2M. The figures are taken from Ref. [90, 91].

Two-magnon excitation

The second-order (or two-magnon) magnetic scattering which involves the creation and destruction of a pair of magnons with wavevector $\mathbf{k}$ and $\mathbf{k}'$ is similar in principle to the second-order phononic scattering that is briefly discussed in Sec. 2.2.1. What is more convenient in the case of magnetic scattering is that typically there is only one magnon branch in a ferromagnet or a simple antiferromagnet in the absence of an external field. With momentum conservation rendering $\mathbf{k} \approx -\mathbf{k}'$, the energy conservation law then gives

$$w_i - w_s = 2w_{\mathbf{k}}. \tag{2.42}$$

The scattered intensity is largely determined by the number of magnons whose energy satisfies Eq. 2.42, and is denoted as the magnon density of states (M-DOS)

$$\rho(w) = \sum_{\mathbf{k}} \delta(w - 2w_{\mathbf{k}}). \tag{2.43}$$

It is the same as the single magnon density of states scaled in frequency by a factor of 2, and generally, the regions of the reciprocal space with large M-DOS are found near the zone boundaries [94], which corresponds to local spin flips in a real-space picture.

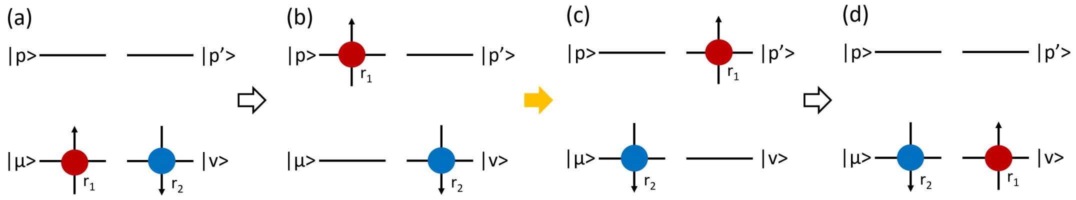

Figure 2.3.4: Schematic representation of the exchange scattering mechanism giving rise to the two-magnon scattering.

Following the second-order phononic scattering, one would naturally try to extend the treatment of the first-order magnetic scattering to the second order. With the same scheme as shown in Fig. 2.3.2, but now the downward-pointing arrow will end on the $S^z = S-2$ ground state level. However, the same mechanism would render a cross section several orders of magnitude smaller than that of the first-order scattering, completely in disagreement with the experimental results as shown in Fig. 2.3.3, where the two-magnon scattering spectra is comparable or even stronger than the single-magnon case. Therefore, the two-magnon scattering arises not from the first-order mechanism taken to a higher order, but from a different mechanism that takes place only in the second order, which is known as the exchange scattering mechanism [86, 95–97]. This mechanism, however, is only applicable in antiferromagnetic systems, and for ferromagnets, the second-order magnetic scattering is simply expected to be much weaker than the first order.

Consider two representative ions μ and v, each belongs to one magnetic sublattice. Suppose the ground state of ion μ is occupied by an electron $\mathbf{r}_1$ with

$s^z = \frac{1}{2}$ on orbital $|\mu\rangle$, while electron $\mathbf{r}_2$ with $s^z = -\frac{1}{2}$ on orbital $|v\rangle$ occupies the ground state of ion v as shown in Fig. 2.3.4.(a). The electric-dipole interaction of the incident and scattered fields, $\mathbf{E}_i$ and $\mathbf{E}_s$, with the electrons and the Coulomb interaction between the electrons are given by the Hamiltonian

$$H = e(\mathbf{E}_i + \mathbf{E}_s) \cdot (\mathbf{r}_1 + \mathbf{r}_2) + \frac{e^2}{4\pi\epsilon_0|\mathbf{r}_1 - \mathbf{r}_2|}. \tag{2.44}$$

The transition matrix element arises in the third-order perturbation theory. A representative matrix element for the Raman process, which is depicted by Fig. 2.3.4, can be written as [68, 86]

$$M = \frac{\langle v_\uparrow(\mathbf{r}_1)|e\mathbf{E}_s \cdot \mathbf{r}_1|p'_\uparrow(\mathbf{r}_1)\rangle \left\langle p'_\uparrow(\mathbf{r}_1)\mu_\downarrow(\mathbf{r}_2)\left|\frac{e^2}{4\pi\epsilon_0|\mathbf{r}_1-\mathbf{r}_2|}\right|v_\downarrow(\mathbf{r}_2)p_\uparrow(\mathbf{r}_1)\right\rangle \langle p_\uparrow(\mathbf{r}_1)|e\mathbf{E}_i \cdot \mathbf{r}_1|\mu_\uparrow(\mathbf{r}_1)\rangle}{(E_p - \hbar w_i)(E_{p'} + \hbar w_{\mathbf{k}} - \hbar w_i)}, \tag{2.45}$$

where $|p\rangle$ and $|p'\rangle$ are orbitals of ion μ and v that satisfy the electric-dipole transition selection rules. The essential part of the transition matrix is the exchange of two electrons as shown by Fig. 2.3.4.(b)-(c), which results in the double spin-flip in the final state. We can write the effective two-magnon Raman scattering operator as [67, 98, 99]

$$\hat{\mathcal{O}} = \sum_{i,j} n_{ij}(\mathbf{E}_i \cdot \mathbf{d}_{ij})(\mathbf{E}_s \cdot \mathbf{d}_{ij})\mathbf{S}_i \cdot \mathbf{S}_j, \tag{2.46}$$

where $\mathbf{d}_{ij}$ is the unit vector connecting the magnetic ion i and j, who has spin $\mathbf{S}_i$ and $\mathbf{S}_j$, respectively. n_{ij} is proportional to the exchange coupling strength, and the sum runs through all pairs of magnetic ions. It is then obvious that the exchange scattering mechanism can only produce magnons in pairs, and therefore is inoperative for one-magnon scattering. Thus the two unrelated mechanisms cast no reason for the second-order magnetic scattering to be smaller than the first order.

Apart from the response intensity, the Raman features arising from two-magnon scattering generally have larger linewidths than that of the one-magnon scattering. Besides the comparison in Fig. 2.3.3, we can also find evidence in the studies of cuprates [100] and iridates [101] shown in Fig. 2.3.5, where very broad two-magnon Raman responses are detected at higher energies.

2.4 Electronic Raman scattering

Besides lattice and spin dynamics, Raman spectroscopy can also give important information on charge dynamics by light scattering of electrons through the creation of variations of the electronic charge density in the system. Same as the phononic Raman scattering, by applying polarization selection rules based on group theories electron dynamics in different regions of the Brillouin Zone can be selectively studied in detail. This important property distinguishes Raman scattering from other techniques such as infrared spectroscopy, thermal and electronic

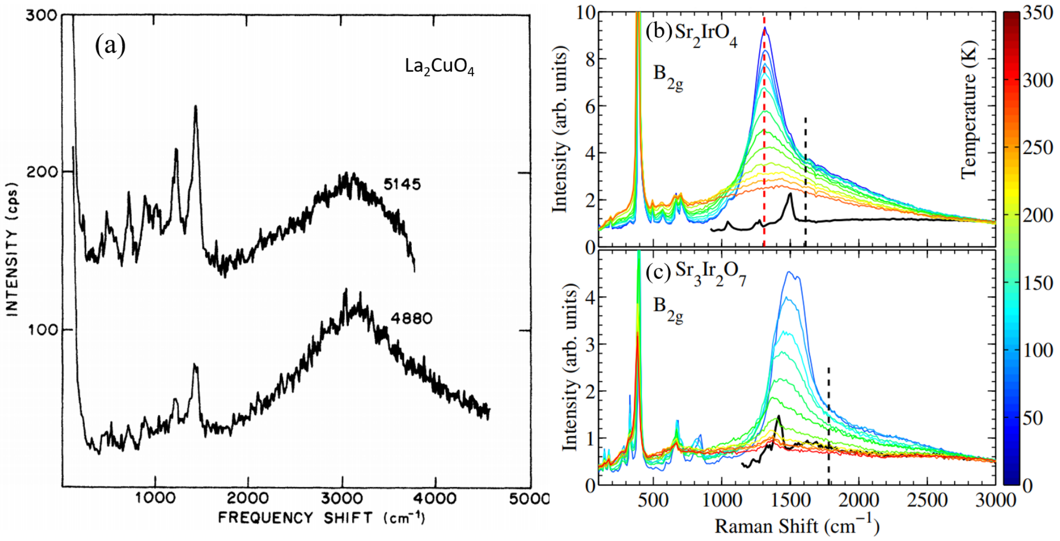

Figure 2.3.5: (a) Raman measurements on La$_2$CuO$_4$ with laser wavelengths 5145 Å and 4880 Å, respectively, where a broad two-magnon mode is detected at around 3000 cm^{-1}. The figure is taken from Ref. [100]. Raman measurements of the B$_{2g}$ modes from 350 K to 10 K for (b) Sr$_2$IrO$_4$ and (c) Sr$_3$Ir$_2$O$_7$, where the broad and strong two-magnon peaks are visible upon cooling. The figure is taken from Ref. [101].

resistivity measurements, *etc.*, which measure averaged quantities over the whole Brillouin zone and are insensitive to anisotropies. In this section, we briefly lay out the theoretical foundation of electronic Raman scattering (more detailed information can be found in Ref. [67]), followed by some of its important applications in correlated systems.

We start by introducing a Hamiltonian for N electrons within the electromagnetic fields:

$$H = \sum_i^N \frac{[\mathbf{p}_i + (e/c)\mathbf{A}(\mathbf{r}_i)]^2}{2m} + H_{Coulomb} + H_{fields} \tag{2.47}$$

$$= \underbrace{\frac{1}{2m}\sum_i \mathbf{p}_i^2 + H_{Coulomb} + H_{fields}}_{H'} \quad + \frac{e}{2mc}\sum_i [\mathbf{p}_i \cdot \mathbf{A}(\mathbf{r}_i) + \mathbf{A}(\mathbf{r}_i)\cdot \mathbf{p}_i] \tag{2.48}$$

$$+ \frac{e}{2mc^2}\sum_i \mathbf{A}(\mathbf{r}_i)\cdot\mathbf{A}(\mathbf{r}_i). \tag{2.49}$$

$\mathbf{p}$ is the momentum operator and $\mathbf{A}(\mathbf{r}_i)$ is the vector potential of the field at $\mathbf{r}_i$. $H_{Coulomb}$ represents the Coulomb interaction and H_{fields} is the Hamiltonian for the free electromagnetic fields. When the field is absent, $H_{Coulomb}$ together with the pure kinetic part $(1/2m)\sum_i \mathbf{p}_i^2$ can be denoted as H_0 which satisfies

$H_0|\alpha\rangle = E_\alpha|\alpha\rangle$, where $|\alpha\rangle$ is the eigenstate of H_0 and E_α is the corresponding eigenvalue.

It is convenient to write the field vector potential $\mathbf{A}(\mathbf{r}_i)$ in the expanded Fourier modes $\sum_{\mathbf{q}} e^{i\mathbf{q}\cdot\mathbf{r}_i}\mathbf{A}_{\mathbf{q}}$, where $\mathbf{A}_{\mathbf{q}}$ can be expressed in second quantization

$$\mathbf{A}_{\mathbf{q}} = \sqrt{\frac{hc^2}{w_{mathbfq}V}}[\hat{\boldsymbol{\epsilon}}_{\mathbf{q}}a_{-\mathbf{q}} + \hat{\boldsymbol{\epsilon}}^*_{\mathbf{q}}a^\dagger_{\mathbf{q}}], \tag{2.50}$$

with V the volume and $a^\dagger_{\mathbf{q}}$, $a_{\mathbf{q}}$ the creation and annihilation operators of photons with energy $\hbar w_{\mathbf{q}}$ and polarization $\hat{\boldsymbol{\epsilon}}_{\mathbf{q}}$. The intensity of the electronic Raman scattering is proportional to the spectral differential cross section which is determined by the transition rate R of scattering an incident phonon with ($\mathbf{q}_i$, w_i, $\hat{\epsilon}^i_{\mathbf{q}}$) into an outgoing state with ($\mathbf{q}_s$, w_s, $\hat{\epsilon}^s_{\mathbf{q}}$):

$$I \propto \frac{d^2\sigma}{d\Omega dw} = \hbar r_0^2\frac{w_s}{w_i}R, \tag{2.51}$$

where $r_0 = e^2/mc^2$ is the Thompson radius, and R can be determined by the Fermi golden rule

$$R = \frac{1}{Z}\sum_{I,F} e^{-\beta E_I}|M_{F,I}|^2\delta(E_F - E_I - \hbar\Omega), \tag{2.52}$$

where Z is the partition function, $\beta = 1/k_BT$, and $M_{F,I}$ is the transition matrix $\langle F|M|I\rangle$ with M the effective light-scattering operator. The sum $\sum_{I,F}$ represents summation over all possible initial and final states, and $\hbar\Omega = \hbar(w_i - w_s)$ is the transferred energy. All three of the last terms of Eq. 2.49 can contribute to $M_{F,I}$. The first two terms couples the electron's current to a single photon and involves only single-photon emission or absorption, while the last term couples the electron's charge to two photons, thus involves absorption and emission (or vice versa) of two photons. A general expression of the matrix element in the second-quantization notations can then be written as

$$\begin{aligned} M_{F,I} = {} & \hat{\boldsymbol{\epsilon}}_i \cdot \hat{\boldsymbol{\epsilon}}_s \sum_{\alpha,\beta} \rho_{\alpha,\beta}(\mathbf{q})\langle F|c^\dagger_\alpha c_\beta|I\rangle \\ & + \frac{1}{m}\sum_v \sum_{\alpha,\alpha',\beta,\beta'} p_{\alpha,\alpha'}(\mathbf{q}_s)p_{\beta,\beta'}(\mathbf{q}_i) \\ & \times \left(\frac{\langle F|c^\dagger_\alpha c_{\alpha'}|v\rangle\langle v|c^\dagger_\beta c_{\beta'}|I\rangle}{E_I - E_v + \hbar w_i} + \frac{\langle F|c^\dagger_\beta c_{\beta'}|v\rangle\langle v|c^\dagger_\alpha c_{\alpha'}|I\rangle}{E_I - E_v - \hbar w_s}\right). \end{aligned} \tag{2.53}$$

Here $c^\dagger_\alpha$, c_β are creation and annihilation operators of electron states α and β, respectively. $|I\rangle$, $|F\rangle$ and $|v\rangle$ are initial, final and intermediate many-electron states with corresponding energies $E_{I,F,v}$. $\rho_{\alpha,\beta}(\mathbf{q}) = \langle\alpha|e^{i\mathbf{q}\cdot\mathbf{r}}|\beta\rangle$ is the matrix element representing single-particle density fluctuations involving α and β states, and

$p_{\alpha,\beta}(\mathbf{q}_{i,s}) = \langle \alpha | \mathbf{p} \cdot \hat{\boldsymbol{\epsilon}}_{i,s} e^{\pm i \mathbf{q}_{i,s} \cdot \mathbf{r}} | \beta \rangle$ is the matrix element for the momentum density. Note that the first term in Eq. 2.53 arises from the two-phonon scattering term in Eq. 2.49 in first-order perturbation theory, while the second term is associated with the single-phonon scattering term in Eq. 2.49 in second order via intermediate states v. The current coupling can only occur in second order due to its odd parity.

Certain simplifications can be made to evaluate Eq. 2.53. We assume the intermediate many-particle states only differ from the initial and final states by single-electron excitations, thus by ignoring the mang-body correlations, we can replace E_v in the denominators in the second term by $E_I - E_{\beta'} + E_\beta$ and $E_I + E_{\alpha'} + E_\alpha$, respectively. By using the closure relation $\sum_v |v\rangle\langle v| = 1$, the four-fermion matrix elements are eliminated, and the matrix element can be reformed into

$$M_{F,I} = \sum_{\alpha,\beta} \gamma_{\alpha,\beta} \langle F | c_\alpha^\dagger c_\beta | I \rangle, \tag{2.54}$$

where

$$\gamma_{\alpha,\beta} = \rho_{\alpha,\beta}(\mathbf{q}) \hat{\boldsymbol{\epsilon}}_i \cdot \hat{\boldsymbol{\epsilon}}_s + \frac{1}{m} \sum_{\beta'} \left(\frac{p^s_{\alpha,\beta'} p^i_{\beta',\beta}}{E_\beta - E_{\beta'} + \hbar w_i} + \frac{p^i_{\alpha,\beta'} p^s_{\beta',\beta}}{E_\beta - E_{\beta'} + \hbar w_s} \right). \tag{2.55}$$

We can further simplify the matrix element by specifying the states α, β by their momentum quantum numbers and thus express the Raman response by the correlation function $\tilde{S}$ of an effective charge density $\tilde{\rho}$

$$I \propto \hbar r_0^2 \frac{w_s}{w_i} \tilde{S}(\mathbf{q}, i\Omega \to \Omega + i0), \tag{2.56}$$

where $\tilde{S}(\mathbf{q}, i\Omega)$ is the Raman effective density-density correlation function

$$\tilde{S}(\mathbf{q}, i\Omega) = \sum_I \frac{e^{-\beta E_I}}{Z} \int d\tau e^{i\Omega\tau} \langle I | T_\tau (\tilde{\rho}(\mathbf{q}, \tau) \tilde{\rho}(-\mathbf{q}, 0)) | I \rangle. \tag{2.57}$$

Here T_τ is the complex time τ ordering operator, and $\tilde{\rho} = \sum_{\mathbf{k},\sigma} \gamma(\mathbf{k}, \mathbf{q}) c^\dagger_{\mathbf{k}+\mathbf{q},\sigma} c_{\mathbf{k},\sigma}$ with $c^\dagger_{\mathbf{k},\sigma}$, $c_{\mathbf{k},\sigma}$ the creation and annihilation operators of electron with momentum $\mathbf{k}$ and spin σ, and $\mathbf{q} = \mathbf{q}_i - \mathbf{q}_s$ the net momentum transferred by the photon. $\gamma(\mathbf{k}, \mathbf{q})$ is the scattering amplitude (also called Raman vertex), and is determined by the matrix element $\gamma_{\alpha,\beta}(\mathbf{k}, \mathbf{q})$ and the incident and scattered light polarizations

$$\gamma(\mathbf{k}, \mathbf{q}) = \sum_{\alpha,\beta} \gamma_{\alpha,\beta}(\mathbf{k}, \mathbf{q}) \hat{\epsilon}_i^\alpha \hat{\epsilon}_s^\beta, \tag{2.58}$$

with now the matrix elements expressed by momentum quantum numbers

$$\gamma_{\alpha,\beta}(\mathbf{k},\mathbf{q}) = \delta_{\alpha,\beta} + \frac{1}{m}\sum_{\mathbf{k}_v}\left[\frac{\langle \mathbf{k}+\mathbf{q}|p_s^\beta|\mathbf{k}_v\rangle\langle \mathbf{k}_v|p_i^\alpha|\mathbf{k}\rangle}{E_\mathbf{k} - E_{\mathbf{k}_v} + \hbar w_i} + \frac{\langle \mathbf{k}+\mathbf{q}|p_i^\alpha|\mathbf{k}_v\rangle\langle \mathbf{k}_v|p_s^\beta|\mathbf{k}\rangle}{E_{\mathbf{k}+\mathbf{q}} - E_{\mathbf{k}_v} - \hbar w_s}\right]. \tag{2.59}$$

Here $p_{i,s}^\alpha = p^\alpha e^{\pm i\mathbf{q}_{i,s}\cdot\mathbf{r}}$ is the projected momentum operators.

We note that through the fluctuation-dissipation theorem, the correlation function $\tilde{S}$ can be related to the imaginary part of the dynamical effective density susceptibility $\tilde{\chi}$ as

$$\tilde{S}(\mathbf{q},\Omega) = -\frac{1}{\pi}[1 + n(\Omega,T)]Im\tilde{\chi}(\mathbf{q},\Omega), \tag{2.60}$$

where $n(\Omega, T)$ is the Bose-Einstein distribution and

$$\tilde{\chi}(\mathbf{q},\Omega) = \langle\langle[\tilde{\rho}(\mathbf{q}),\tilde{\rho}(-\mathbf{q})]\rangle\rangle_\Omega, \tag{2.61}$$

with $\langle\langle ... \rangle\rangle$ represents a thermodynamic average. Therefore for noninteracting (or weakly correlated) electrons, the Raman response is given by the two-particle effective density correlation function. We can then calculate the Raman response by summing up contributions from different Feynman diagrams as given in Ref. [67] with **k**-dependent Raman vertices γ.

To calculate the Raman vertices, we notice that for small momentum transfers (as $q \ll k_F$, $q \to 0$ is a good approximation) and nonresonant scattering, $\gamma_{\alpha,\beta}(\mathbf{k},\mathbf{q})$ recovers the form of the effective-mass tensor [102, 103]

$$\gamma_{\alpha,\beta}(\mathbf{k}, q \to 0) = \frac{1}{\hbar^2}\frac{\partial^2 E_\mathbf{k}}{\partial k_\alpha k_\beta}. \tag{2.62}$$

Therefore, the Raman vertex is proportional to the second derivatives of the conduction band $E_\mathbf{k}$ projected by the polarization vectors of the incident and scattered photons. We can then relate the Raman response to specific regions of the Fermi surface, provided that the information of the band structure is available. In cases without detailed knowledge of the band structure, we can still express the polarization dependence of $\gamma_{\alpha,\beta}(\mathbf{k}, q \to 0)$ by group theory arguments. As the charge density fluctuations vary along the same directions as the polarizations of the incident and scattered photons, these density fluctuations thus obey the same symmetry rules governing the scattering geometry. The Raman tensor can then be decomposed into basis functions Φ_μ of the irreducible point group of the crystal [104–106]

$$\gamma(\mathbf{k}) = \sum_\mu \gamma_\mu \Phi_\mu(\mathbf{k}), \tag{2.63}$$

where μ is the irreducible representations of the point group, and the polarization directions of the incident and scattered photons determine which set of μ contributes to the sum. As most high-T_c cuprates and Fe-based superconductors crystallize in tetragonal structure, in Fig. 2.4.1 we show first the Raman vertices

γ_μ for irreducible representations of the D_{4h} point group, followed by the correspondingly probed areas (light color) in the 1-Cu Brillouin zone. Note that Raman response scales with γ_μ^2, and therefore is insensitive to the phase of the Raman vertices.

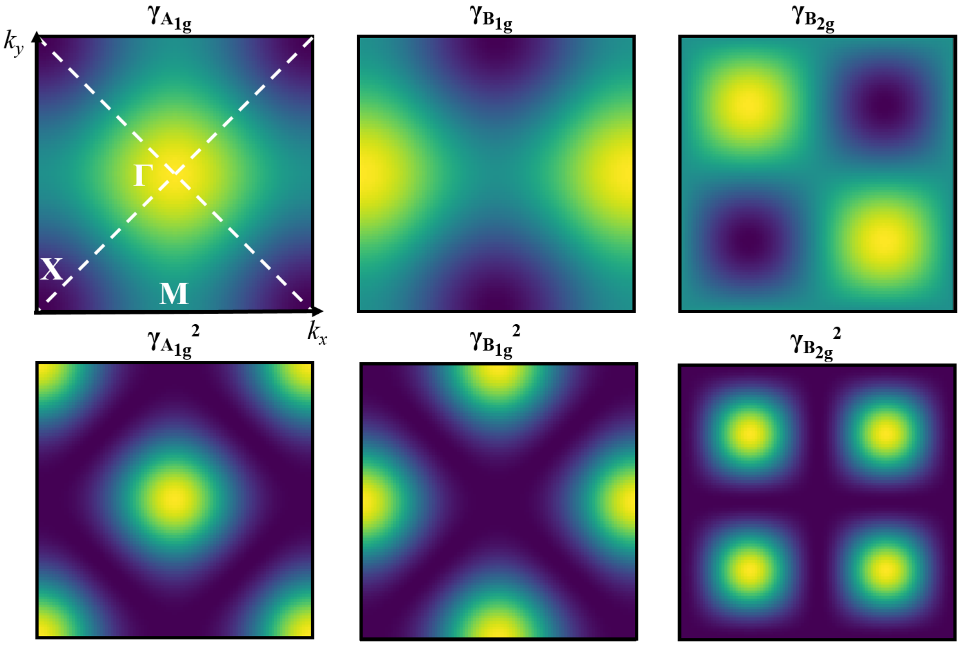

Figure 2.4.1: The top row shows schematic illustrations of the Raman vertices γ_μ for irreducible representations $\mu = \mathrm{A}_{1g}$, B_{1g} and B_{2g} of the D_{4h} point group. The bottom row gives the corrsponding probed Brillouin zone as the Raman response scales with γ_μ^2. The lighter the color, the larger the magnitude.

The ability to probe selective regions of the Fermi surface is the most important and mostly exploited property of the electronic Raman scattering. One of the extraordinary early achievements is the prediction of the d-wave superconducting gap symmetry of high-T_c cuprates. Evidence of a gap anisotropy in $Bi_2Sr_2CaCu_2O_{8+\delta}$ was first discovered by Raman measurements in different polarization configurations as shown in Fig. 2.4.2.(a)-(d). In general, when entering the superconducting state, the spectral weight will be redistributed due to the opening of a superconducting gap. If the gap is isotropic, one would expect in all probed channels complete suppression of scattering in the low-energy part ($\Omega \leq 2\Delta$) and maximum signal at a frequency equal to twice the gap energy. However, as can be seen in Fig. 2.4.2.(b)-(d) the peak in the B_{1g} response is at ~ 30% higher energy than the B_{2g} (or A_{1g}) configuration, and the low-frequency spectra also show different Ω-dependence in different channels [107]. In order to explain the phenomena, a gap with $d_{x^2-y^2}$ symmetry was proposed with the proper momentum- and symmetry-dependencies of the Raman vertices $\gamma_\mu(\mathbf{k})$ and $\mathbf{k}$-dependent energy gap $\Delta(\mathbf{k})$ taken into account. Excellent agreement between the calculated and measured spectra has been found as shown in Fig. 2.4.2.(e)-(f). More importantly, such a prediction of d-wave theory was found to be valid in various optimally

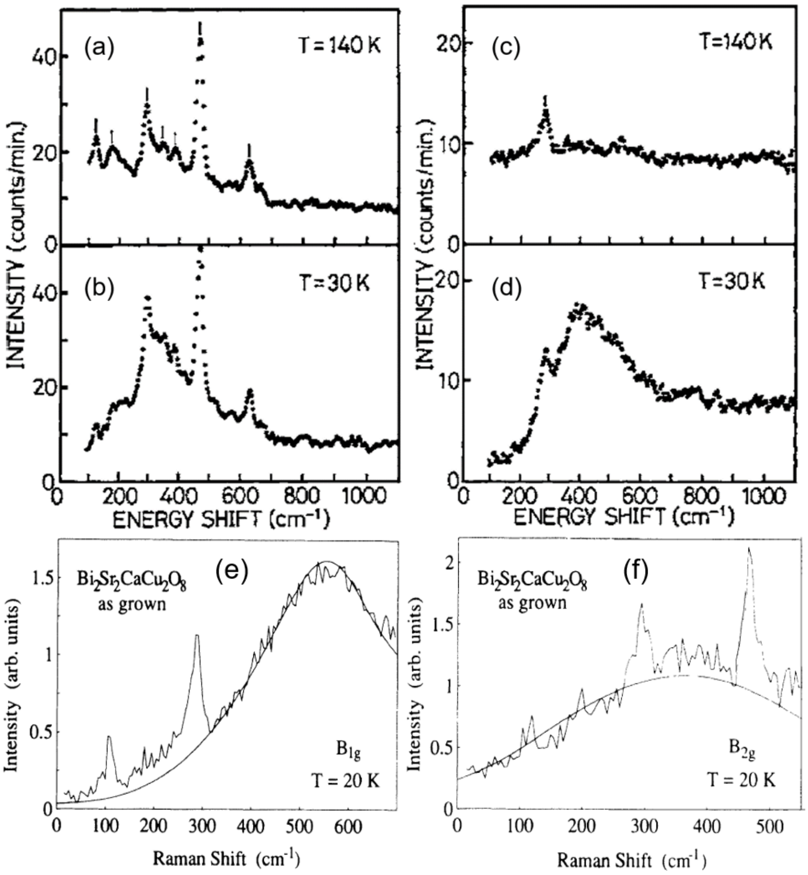

Figure 2.4.2: On the left side are the Raman spectra of $Bi_2Sr_2CaCu_2O_{8+\delta}$ in A_{1g} + B_{2g} channel in the (a) normal state and (b) superconducting state. On the right side are Raman responses in B_{1g} (+ A_{2g}) channel in the (c) normal state and (d) superconducting state. The figures are taken from Ref. [107]. (e) and (f) show the calculated spectra with $d_{x^2-y^2}$ superconducting gap symmetry compared with the experimental points in the B_{1g} and B_{2g} configurations, respectively. The figures are taken from Ref. [108].

hole-doped cuprates [109–113], contributing significantly to the understanding of the pairing mechanism in unconventional superconductors.

Electronic Raman scattering is also proven to be an excellent tool to probe all types of dynamic nematicity [114–118]. In some other experiments, the nematic order parameter is extracted from in-plane anisotropy from detwinned samples [32, 44, 119]. Take elastoresistivity measurement as an example, the nematic susceptibility is calculated by the strain derivative of the resistivity anisotropy, where the sample is under constant strain applied by the deformation of a piezo. However, extra care must be paid to ensure the system is always in the regime of linear response and the effect of intrinsic built-in strain raised from the different thermal expansions of the sample and the piezo stack must be taken into account [119]. On the other hand, nematic fluctuations above the transition can be directly probed by electronic Raman scattering without any lattice effects on the samples. If the

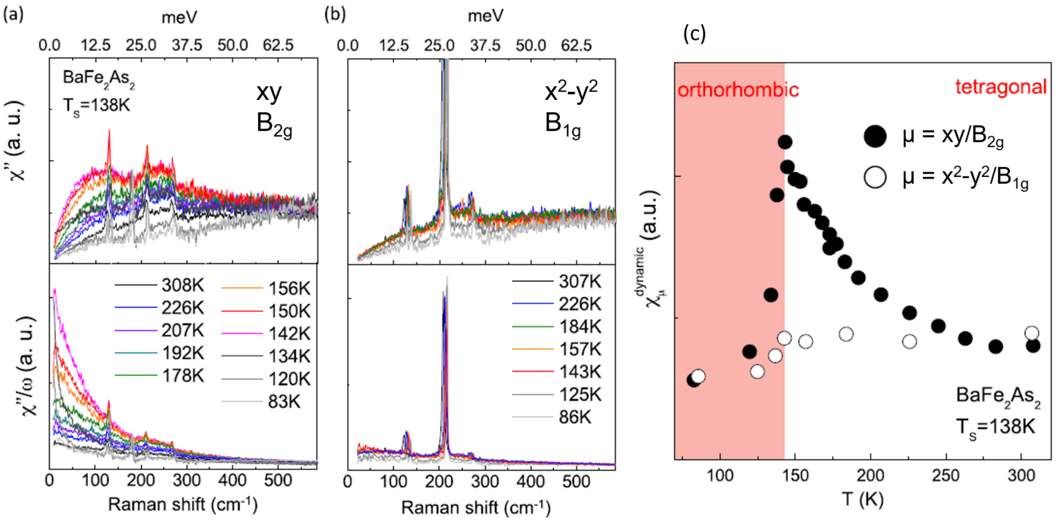

Figure 2.4.3: (a) Raman response χ'' and Raman conductivity χ''/Ω in the B_{2g} channel of $BaFe_2As_2$. (b) The same spectra in the B_{1g} channel. (c) Extracted nematic susceptibility using Kramers-Konig relationship in the B_{1g} and B_{2g} symmetry channels as a function of temperature. The divergent behavior is only observed with B_{2g} configuration. The figures are taken from Ref. [48, 114].

transition is indeed a consequence of condensation of an electronic nematic order parameter, its fluctuations will be observed in the associated symmetry channel and increase as the temperature is cooled towards the transition temperature. A characteristic signature is a quasi-elastic peak present in the low-frequency Raman conductivity (χ''/Ω) with a Lorentzian lineshape which sharpens as the system approaches the transition. Taking the well-studied $BaFe_2As_2$ as an example [48], we show the Raman response χ'' and Raman conductivity χ''/Ω in two symmetry channels in Fig. 2.4.3.(a)-(b). While the Raman response in B_{1g} channel is almost temperature independent, the spectral weight of the low-energy part of the B_{2g} spectra increases dramatically as the temperature is lowered towards T_s. The measured χ''_μ can then give the real part of the uniform response function by using the Kramers-Kronig relation

$$\chi_\mu^{dynamic} = \frac{2}{\pi}\int_0^\infty \frac{d\Omega}{\Omega}\chi''_\mu(\mathbf{q}=0,\Omega) = \lim_{\Omega\to 0}\chi_\mu(\mathbf{q},\Omega), \tag{2.64}$$

with μ indicating the associated symmetry. The resulted nematic susceptibilities of $BaFe_2As_2$ in two channels are shown in Fig. 2.4.3.(c), where divergent behavior at T_s is only observant in the B_{2g} configuration. The corresponding electronic nematic transition temperature T_0 can be subsequently extracted by fitting $\chi_{B_{2g}}^{dynamic}$ using the Curie-Weiss law

$$\chi_{B_{2g}}^{dynamic} = A + \frac{C}{T - T_0}, \tag{2.65}$$

where A and C are temperature-independent constants. Note that typically T_0

is much lower (at least 40 K) than the actual phase transition temperature T_s, which should arise from the fact that T_0 is deduced from lattice-free electronic susceptibility, and the actual transition temperature is higher due to the finite coupling between the electronic and lattice sub-systems.

2.5 Analysis of Raman data

Both lattice vibrations (phonons) and spin-wave excitations (magnons) can be treated within the harmonic approximation, however, as already introduced in Sec. 2.2.4, the spectral light is more correctly described as the emission from a damped harmonic oscillator (DHO).

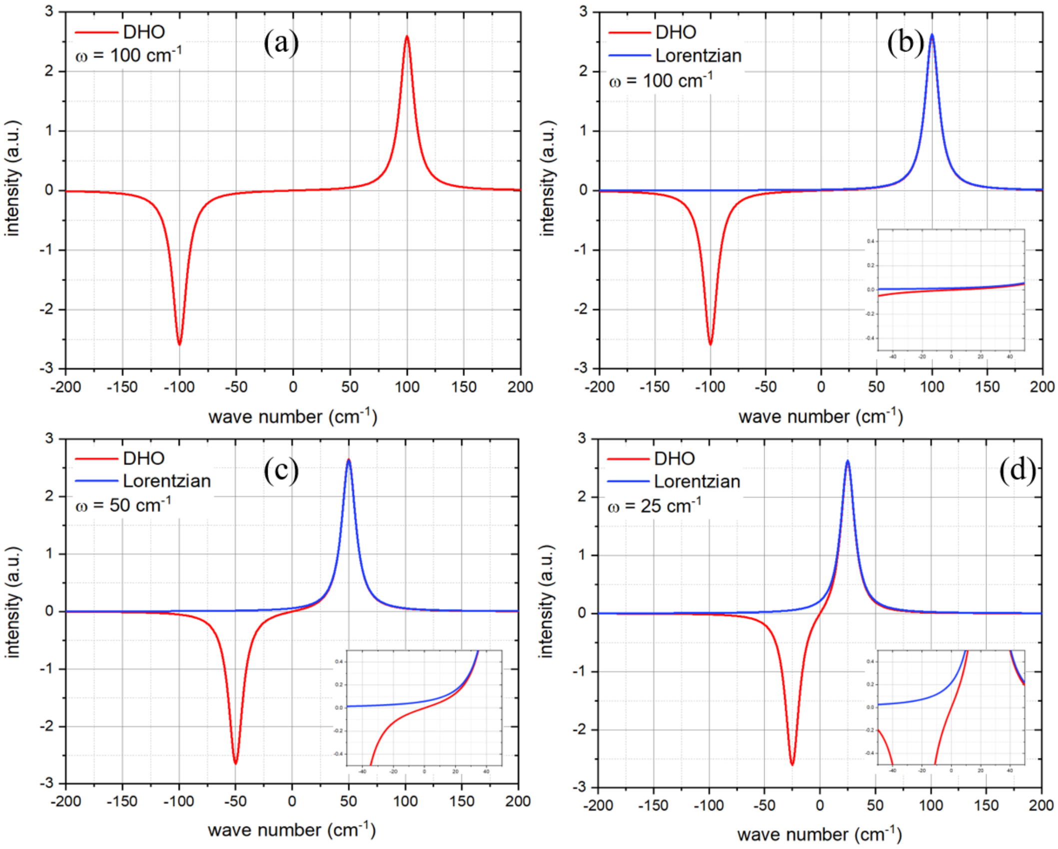

Figure 2.5.1: (a) Raman spectral lineshape described by the DHO function. The comparison between DHO and Lorentzian profile with excitations at (b) w = 100 cm^{-1}, (c) w = 50 cm^{-1}, and w = 25 cm^{-1} is shown, and discrepancy grows larger with lower excitation frequency.

From Eq. 2.26 we can then write

$$I(\Omega) \propto \left[\frac{\Gamma(\Omega)/2}{(\Omega-w)^2+(\Gamma(\Omega)/2)^2} - \frac{\Gamma(\Omega)/2}{(\Omega+w)^2+(\Gamma(\Omega)/2)^2}\right] \times (n(\Omega)+1), \tag{2.66}$$

where $n(\Omega)$ is the Bose-Einstein thermal occupation number. After the Bose-factor correction, the Raman response (the imaginary part of the response function) can be described by the DHO function

$$\chi''(\Omega) \propto \frac{\Gamma(\Omega)/2}{(\Omega - w)^2 + (\Gamma(\Omega)/2)^2} - \frac{\Gamma(\Omega)/2}{(\Omega + w)^2 + (\Gamma(\Omega)/2)^2}. \tag{2.67}$$

The spectrum described by Eq. 2.67 is shown in Fig. 2.5.1.(a). By comparing with the Lorentzian line that is typically used to describe the spectral response (see Eq. 2.28), an alarming discrepancy is observed in Fig. 2.5.1.(b)-(d), especially with low-energy excitations. Therefore, Raman features observed in our work with energy higher than 100 cm^{-1} are fitted with the symmetric Voigt profile (provided that no Fano asymmetry is observed) [120], which is the convolution of a Lorentzian lineshape with the Gaussian lineshape imposed by the instrumental resolution function. The convolution is given by

$$y(x) = \int_{-\infty}^{\infty} L(x-\tau)G(\tau)d\tau, \tag{2.68}$$

where $L(x)$ and $G(x)$ are the Lorentzian and Gaussian profiles, respectively. When Raman modes appear at energies below 100 cm^{-1}, we adopt Eq. 2.67 instead as the fitting profile. Note that in our study typically broad low-energy modes are observed with FWHM $\sim$ 20 cm^{-1}, as a result, the broadening effect due to instrumental resolution was ignored in the data treatment.

2.6 Raman set-up

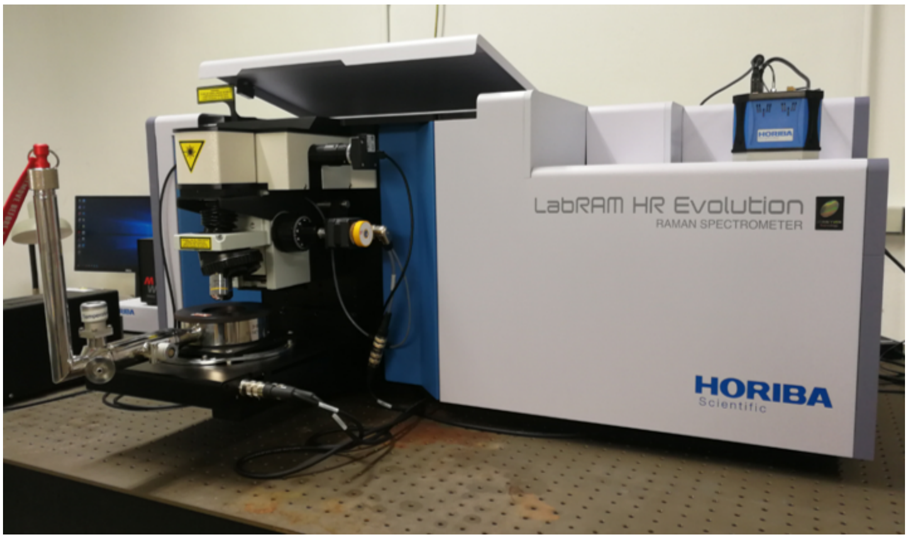

Figure 2.6.1: The Jobin-Yvon LabRam HR evolution spectrometer used in this thesis work.

Raman scattering experiments in this work were performed in the backscattering geometry using a Jobin-Yvon LabRAM HR evolution spectrometer (Fig. 2.6.1). An illustration of the internal optical path is shown in Fig. 2.6.2. The whole setup is placed on a vibration-damped optical table. In most of our experiments, a He-Ne 10mW laser with vertically polarized 633 nm excitation wavelength is used as the incident source.

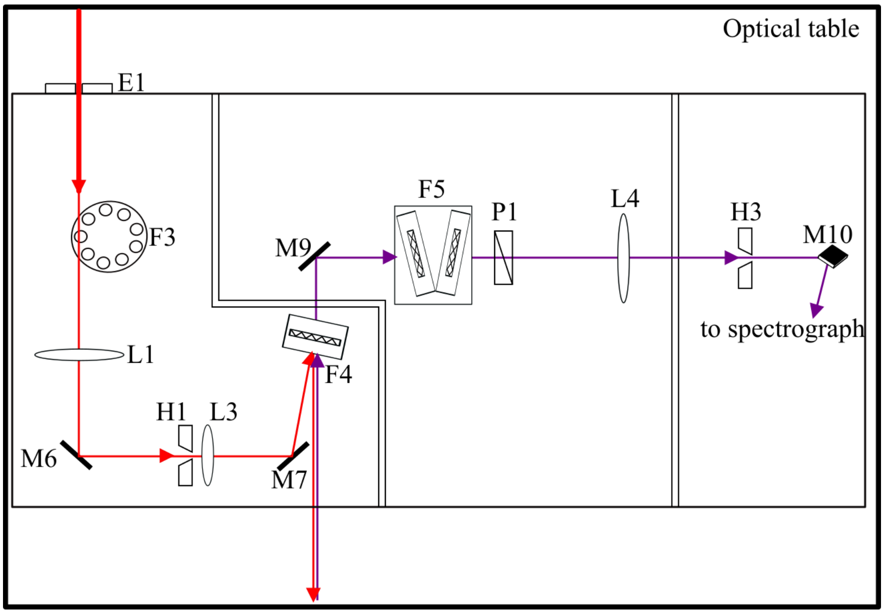

Figure 2.6.2: Schematic illustration of the internal optical path.

The beam enters through E1 and goes through the laser intensity absorption filter F3, which is equipped with 9 different positions ND neutral filters with optical densities 100%, 50%, 25%, 10%, 5%, 3.2%, 1%, 0.1% and 0.01%. The L1 lens then focuses the laser beam via the mirror M6 on the pinhole H1. The resulting laser image is focused by lens L3 via the mirror M7 on the F4 notch filter. This filter serves on one hand as a laser plasma lines purifier, and on another hand as a mirror, so with an appropriate angle, it can reflect the laser image completely towards the sample. The clean laser beam is focused on the sample by microscope objectives (10x, 50x, 100x). For calibration, the 100x objective is routinely used, whereas the 50x objective is used for all Raman measurements. The laser power with different optical densities and 50x objective is tabulated in Tab. 2.2. In the backscattering configuration, the Raman signal is then collected by the same objective. The scattered beam passes through the notch filter and yet another Bragg filter F5 for higher suppression of the exciting line. A polarizer is inserted at P1 to govern the outgoing polarization. The resulting signal is focused onto the entrance slit H3 through lens L4, and is guided into the spectrograph through M10.

The spectrometer is equipped with two gratings, 1800 gr/mm and 600 gr/mm, to vary both spectral resolution and spectral coverage. The energy resolutions are ~ 0.6 cm^{-1} for 1800 gratings and ~ 1.54 cm^{-1} for 600 gratings, which were determined by measuring the resolution limited Ne emission lines. A Peltier-cooled CCD detector is used for Raman signal detection. With the conjunction of notch

Table 2.2: Laser power for He-Ne laser with different filters

Objective	Filter	Laser power (mW)
MDPlan ×50	1%	0.09
	5 %	0.77
	10 %	1.04
	25 %	3.99
	50 %	6.69

filter and Bragg filter, the elastic line is much suppressed, allowing the detection of Raman signal as low as 15 cm^{-1}.

For low-temperature Raman measurements we used a horizontal helium flow cryostat (Konti-Cryostat-Mikro, Cryovac) as shown in Fig. 2.6.3, which is positioned under the microscope objective. In the middle of the cryostat stands a copper cold finger where the samples are mounted. Typically we used Apiezon N grease as sample glue to ensure thermal contact and a stress-free environment even at low temperatures. The temperature is monitored by a combination of a temperature controller and a heater and can reach as low as ~ 4 K with continuous helium flow.

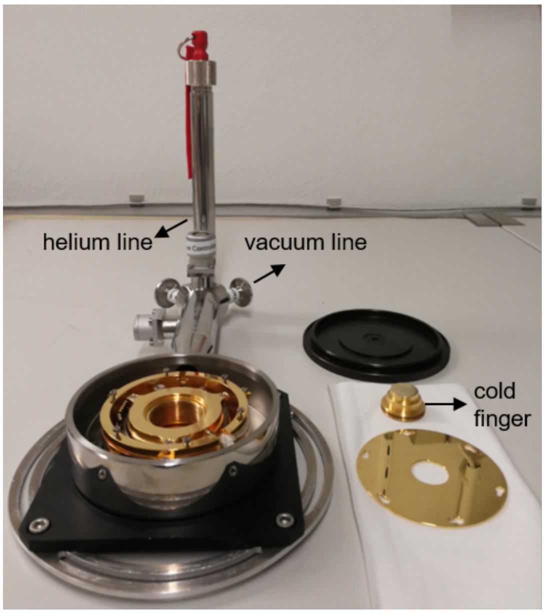

Figure 2.6.3: Horizontal helium flow cryostat used in this thesis work.

Chapter 3

Raman measurements on CrAs

3.1 Introduction

CrAs belongs to the large family of transition-metal pnictides with a general formula MX (M = transition metal, X = P, As, Sb). At ambient conditions, it crystallizes into an orthorhombic structure of MnP-type with space group $Pnma$ ($c > a > b$). Upon cooling, CrAs undergoes a first-order phase transition from a paramagnetic (PM) state to a double-helical magnetic state at $T_N \approx 265$ K, accompanied by a giant structural anomaly [53–56]. At T_N, the crystallographic b-axis expands by $\sim$3.9% and the unit-cell volume by $\sim$2.2%, while the space group remains unchanged [121]. Such a transition between phases which have the same space group and corresponding atoms on the same Wyckoff positions belongs to the so-called type 0 (or isosymmetric) transition. It occurs when the system goes through a crossover where the changes in axial ratios or atomic coordinates that are unconstrained by the current symmetry lead to distinctively different coordination environments [122].

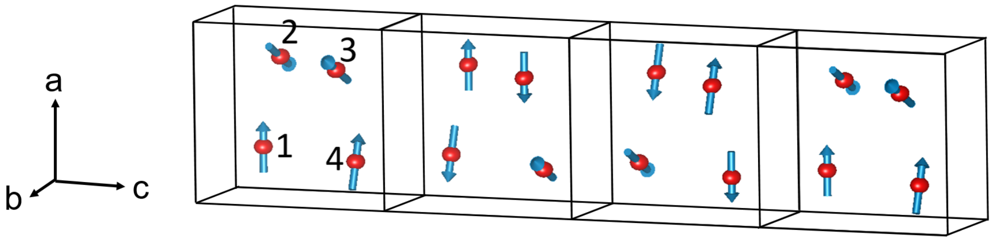

Figure 3.1.1: Incommensurate double-helical magnetic structure of CrAs shown for four unit cells along the crystallographic c-axis.

Since the early 1970s, CrAs has been subjected to intense investigations mainly due to its itinerant character and the complex antiferromagnetic (AFM) order [53–56, 123]. The magnetic structure was, in particular, studied in great detail. Neutron diffraction measurements have revealed the double-helical structure with a large magnetic moment of ~1.73 μ_B/Cr at 1.5 K lying and rotating in the ab crystallographic plane, and the spirals propagate with a wave vector of (0 0 0.356) in the reciprocal unit cell [124, 125] . The magnetic phase angle ϕ defined as the angle between Cr atoms 1 and 2 (as shown in Fig. 3.1.1), and atoms 3 and 4 were found to be -110(4)° at 1.5 K. Note that the magnetic moments between atoms 1 and 4 and atoms 2 and 3 are almost antiparallel. To understand the formation of such a peculiar magnetic structure, special attention was paid to the intimate relationship between the lattice structure and the underlying magnetic order. Several studies have interpreted the helical magnetic ordering below T_N as a result of an electronic transition from collective states to localized states due to increased Cr-Cr distance as a consequence of the b-axis expansion [55, 126]. The study by Suzuki and Ido [121], in which the effects on T_N of various substitutions for Cr by other transition metals, or for As by other pnictogens were summarized, has further determined a critical b-axis length ($b_c = 3.38$ Å), and the helical magnetic order exits only when $b > b_c$, irrespective of the substitution elements. The magnetic structure of CrAs has been modeled using a Heisenberg-like Hamiltonian $H = \sum_{i,j} J_{ij}\tilde{\mathbf{S}}_\mathbf{i} \cdot \tilde{\mathbf{S}}_\mathbf{j}$ with J_{ij} representing the most important exchange integrals in this structure type. Although the ratio between the exchange couplings has been determined based on the stable conditions for the double-helical magnetic ground state, the values of the exchange couplings are not yet known. [56, 59]. Note that the early researches on CrAs have mostly been limited to polycrystallines based on the fact that pristine compounds tend to break upon thermal cycling due to the large magnetoelastic effect across the magnetic transition.

The interest for this material has been recently revived due to the discovery of superconductivity (SC) under pressure in two independent studies in 2014 [57, 58]. Resistivity (see Fig. 3.1.2.(a)-(c)) and ac susceptibility measurements performed on CrAs single crystals show suppression of the helical magnetic order (manifested by the decreasing T_N) under hydrostatic pressure, and bulk SC emerges and displays a dome-shaped pressure dependence with a maximum SC transition temperature $T_c \approx 2$ K at $p_c \sim 10$ kbar as shown in Fig. 3.1.2.(d). These reports provided first evidence of superconductivity in Cr-based materials, and more importantly, CrAs exhibits several features that are generally encountered in unconventional superconductors. First of all, the dome-like pressure dependence of T_c resembles that of many other known unconventional SCs, such as the high-T_c cuprates [127] and iron-pnictide SCs [23], where SC universally emerges in proximity to the long-range magnetic order, which strongly suggests a pairing mechanism via magnetic fluctuations. This suggestion is further supported by evidences at both $p = 0$ and $p \geq p_c$ (where long-range magnetic order vanishes). As shown in Fig. 3.1.3.(a), at ambient pressure the magnetic susceptibility of single crystal CrAs increases linearly with temperature up to 700 K (well above T_N), which has been generally found in iron-based SCs, and is often regarded as an indication of finite AFM fluctuations in the PM phase [57, 128]. Above p_c, nuclear quadrupole resonance (NQR) measurements were performed on single crystal CrAs [129], in which the nuclear spin-lattice relaxation rate $1/T_1$ in the normal state deviate significantly from Fermi liquid (FL) behavior below 100 K as shown in Fig. 3.1.3.(b), indicating

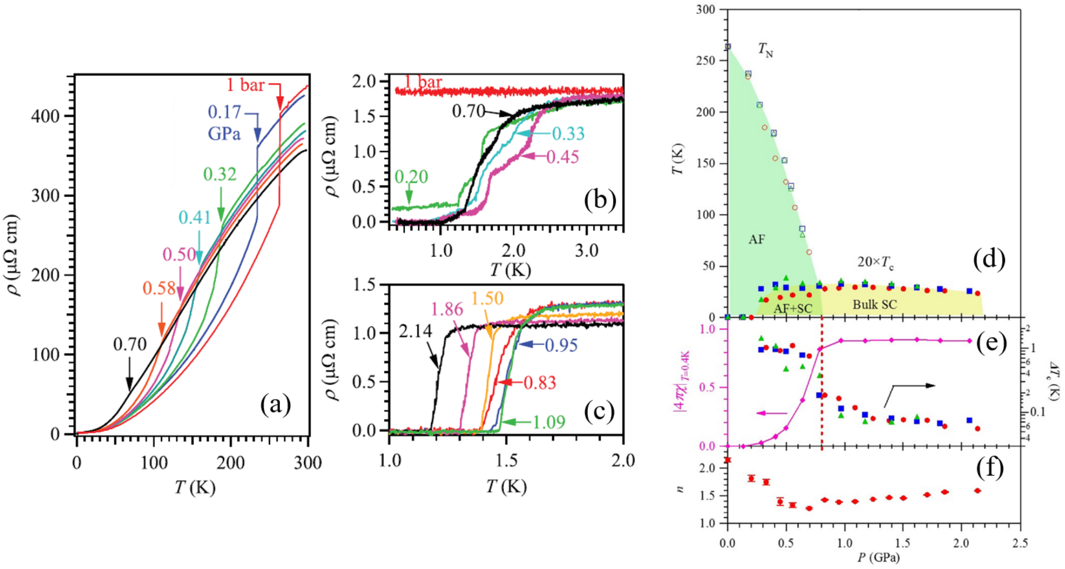

Figure 3.1.2: (a) Resistivity $\rho(T)$ of CrAs single crystal under hydrostatic pressure up tp $p = 0.70$ GPa, highlighting the suppression of T_N under pressure. $\rho(T)$ data at low temperatures is shown in (b) for $p \leq 0.7$ GPa with an inhomogeneous SC phase and (c) for $p \geq 0.83$ GPa with a sharp SC transition. (d) Temperature-pressure phase diagram of CrAs. T_c has been scaled for clarity. (e) Pressure dependence of $|4\pi\chi|_{T=0.4K}$, which is the SC shielding fraction at 0.4 K, and that of ΔT_c which is the SC transition temperature width, defined as the 10-90% SC transition width. (f) Low-temperature resistivity exponent n as a function of pressure, obtained from the power-law fitting below 10 K. The figures are taken from Ref. [57].

development of magnetic correlations towards lower temperatures. In addition, the absence of the coherent Hebel-Slicher peak in the nuclear relaxation rate $1/T_1T$, which is considered the marker of BCS superconductor [130], further suggests an unconventional pairing mechanism in CrAs. This argument is of course not going unchallenged. Muon spin rotation study on powder CrAs [131] uncovered an intermediate pressure range between 3.5 kbar to 7 kbar where superconducting and the magnetic volume fractions are spatially phase separated and compete only for phase volume instead of the order parameter. Moreover, T_c was found to be the highest within the intermediate pressure range when the nonmagnetic volume fraction is at the lowest, contradicting the previous reports of the competing relation between superconductivity and magnetism.

On the other hand, non Fermi liquid (nFL) behavior of CrAs is further reported in electrical resistivity measurements upon applying pressure. In stark contrast to the FL behavior at ambient pressure [132], the low-temperature resistivity exponent n from the power law $\rho(T) = \rho_0 + AT^n$ was found to be close to 1.5 under pressure (see Fig. 3.1.2.(e)-(f)) [57, 59], which is very close to the value predicted for incoherent scattering of quasiparticle by magnetic interactions in 3D antiferromagnets [133, 134]. Close to p_c, the T-quadratic coefficient A, defined by

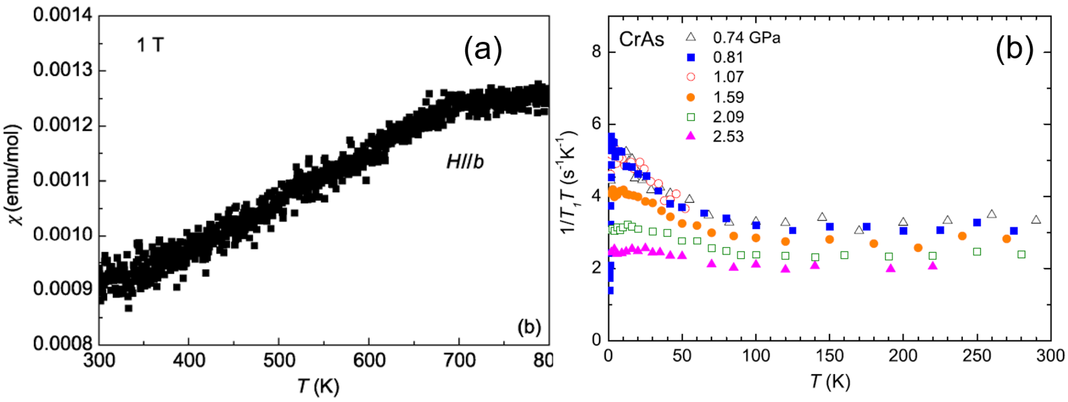

Figure 3.1.3: (a) Magnetic susceptibility measurement on single crystal CrAs between 300 and 800 K for $\mathbf{B}//b$. The figure is taken from Ref. [132]. (b) $1/T_1T$ in the PM state as a function of temperature. The figure is taken from Ref. [129]. Note that in their study the magnetic transition is fully suppressed when $p \geq 0.7$ GPa.

$\rho - \rho_0 = AT^2$ and is related to the effective mass of charge carriers in the FL theorem, displays a pronounced peak as shown in Fig. 3.1.4.(b), which can be further confirmed from the sizable enhancement of the electronic specific-heat coefficient γ around x_c based on the specific-heat measurements on CrAs$_{1-x}$P$_x$ [59]. These features have been interpreted as a signature of quantum criticality, which in turn suggests an unconventional superconducting pairing mechanism. We briefly note that phosphorous-doping produces a similar effect as hydrostatic pressure on suppressing T_N in CrAs. However, no SC has been detected in CrAs$_{1-x}$P$_x$ due to the strong disorder introduced by doping, which is again consistent with the nature of unconventional superconductivity [57, 59, 135].

It is thus evident from previous studies that CrAs exhibit complex superconducting behavior under either physical- or chemical-pressure, and an unconventional pairing mechanism through magnetic fluctuations is strongly suggested. To gain more insight into the superconductivity of CrAs under pressure, one is first required to obtain a deeper and more comprehensive understanding of the strong coupling of the lattice with the magnetic order at ambient pressure, which already manifests itself through the giant magnetoelastic effect at T_N. To the best of our knowledge, no study of the lattice dynamics of CrAs nor its coupling to magnetism is reported, and we believe such a study can facilitate our understanding of the impact on the magnetic order when the system is under structural distortion by means of applied pressure, which will in return affect the superconductivity. In the following sections, after a brief introduction of the sample preparation and characterization process, a detailed report of the experimental results of Raman scattering measurements on high-quality single crystals CrAs is presented.

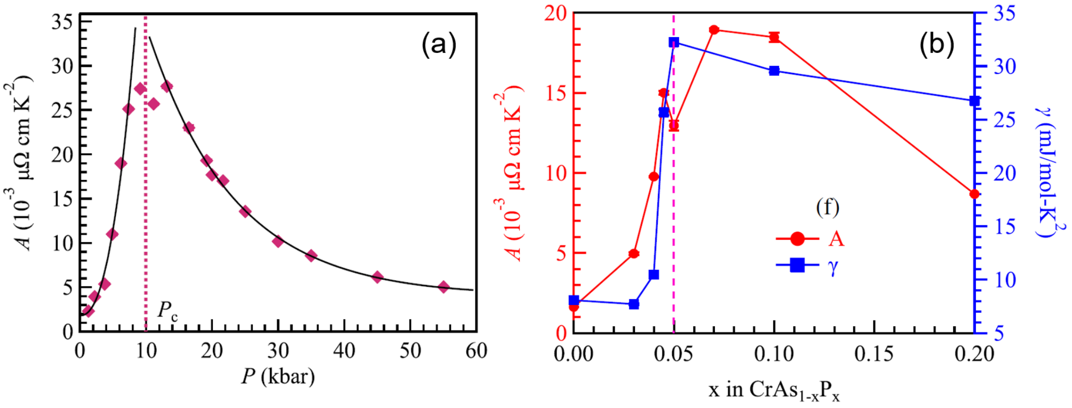

Figure 3.1.4: (a) T-quadratic coefficient A for CrAs as a function of pressure, and displays a pronounced peak around $p_c \approx 10$ kbar. (b) Chemical pressure dependence of the T-quadratic coefficient A and electronic specific-heat coefficient γ for CrAs$_{1-x}$P$_x$. Both show strong enhancement near x_c. The figures are taken from Ref. [59].

3.2 Experiment detail

3.2.1 Crystal growth and structural characterization

Single crystals of CrAs were grown from Sn flux. We started by preparing polycrystalline CrAs from the high-purity elements chromium (99.99 %, Alfa Aesar) and arsenic (99.999 %, ChemPUR). The elements were weighed stoichiometrically and subsequently evacuated and sealed in a quartz ampoule. The mixture was heated at 700°C for 20 h and then cooled down to room temperature (RT) with a cooling rate of 50°C/h. The product was grinded in an argon atmosphere in a glove box, and powder X-ray diffraction was used to check the phase purity. Polycrystalline CrAs are then added to an alumina crucible with pieces of Sn with a molar ratio of CrAs:Sn ≈ 1:10, and placed in a quartz ampoule which was subsequently sealed after evacuated at 10^{-5} mbar. The quartz ampoule was heated to 650°C and held there for 10 h, then heated to 900°C. After 5 h, the ampoule was slowly cooled to 685°C in 7 days. At this temperature, the excessive Sn was centrifuged and a 30% HNO3 solution was used to wash off the remaining Sn flux. In the end we obtained large shiny crystals with dimensions up to 5 × 0.5 × 0.7 mm as shown in Fig. 3.2.1.(a).

Laue measurements were performed on several single crystals to determine the orientation of the crystallographic a-, b- and c-axis. The single crystals show morphology similar to a hexagonal system, and the a-axis is always along the hexagonal axis, whereas the b- and c-axis are not necessarily perpendicular to the hexagonal surface. Fig. 3.2.1.(b) gives an example of the orientation of the crystal axes.

The structural information of single crystal CrAs was collected using temperature-

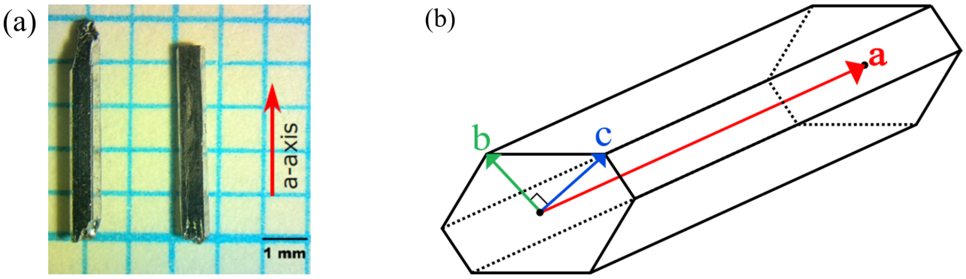

Figure 3.2.1: (a) CrAs single crystals with the typical size. (b) Schematic representation of the CrAs crystal morphology and crystallographic lattice axes.

dependent X-ray diffraction. The measurements were conducted on a STOE imaging plate diffraction system (IPDS-2T) using Mo $K\alpha$ radiation between 85 K and room temperature. All accessible symmetry-equivalent reflections, around 5000, were measured up to a maximum angle of $2\theta = 65°$. The collected raw data were first corrected for Lorentz, polarization, extinction, and absorption effects. Subsequently around 160 averaged symmetry-independent reflections (I $> 2\sigma$) were included for the refinements in space group $Pnma$ using SHELX and JANA2006. For all temperatures the weighted reliability factors (ωR_2) are around 4 %, which indicates the excellent refinement. The orthorhombic unit cell is displayed in Fig. 3.2.2.(a), where Cr and As reside on the Wyckoff positions 4c with coordinates x, $\frac{1}{4}$, z. Fig. 3.2.2.(b) shows the temperature dependence of the a-, b- and c-axis lattice parameters, and the enormous b-axis expansion across the first-order magnetic transition is clearly observed.

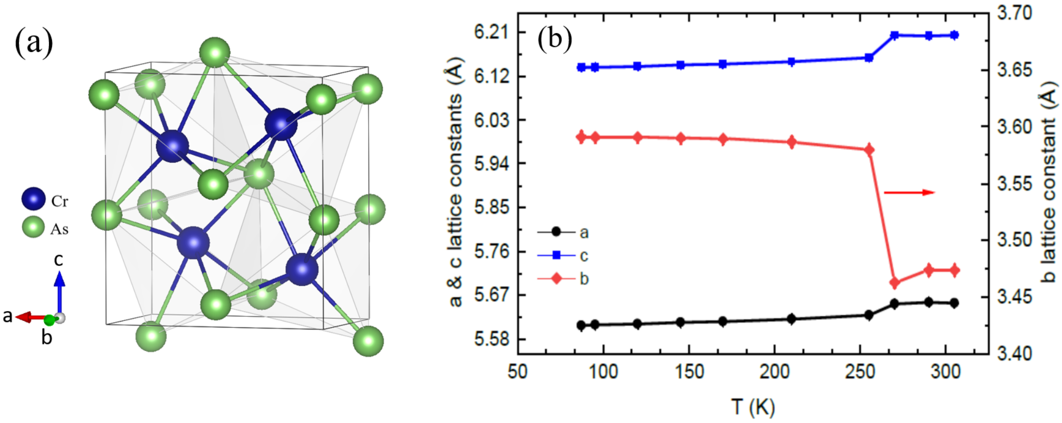

Figure 3.2.2: (a) Crystallographic unit cell of orthorhombic CrAs. (b) The temperature dependence of the crystallographic a-, b- and c-axis, measured by single crystal X-ray diffraction.

The obtained structural parameters at 95K and room temperature are listed in Appendix. A.

3.2.2 Magnetic measurements

We have performed magnetic susceptibility measurements on CrAs. A single crystal with mass $\approx$ 12 mg was glued to a polyether ether ketone substrate and mounted into a Quantum Design physical properties measurement system. The measurements were conducted with the standard vibrating sample magnetometer option with a field of 1 T along the crystallographic a-axis. The results are shown in Fig. 3.2.3, where a sharp jump with a width of < 1.5 K clearly indicates the magnetic transition. A pronounced hysteresis was observed, as expected for a first-order phase transition. The transition temperature is 265 K upon cooling, and 272 K on warming.

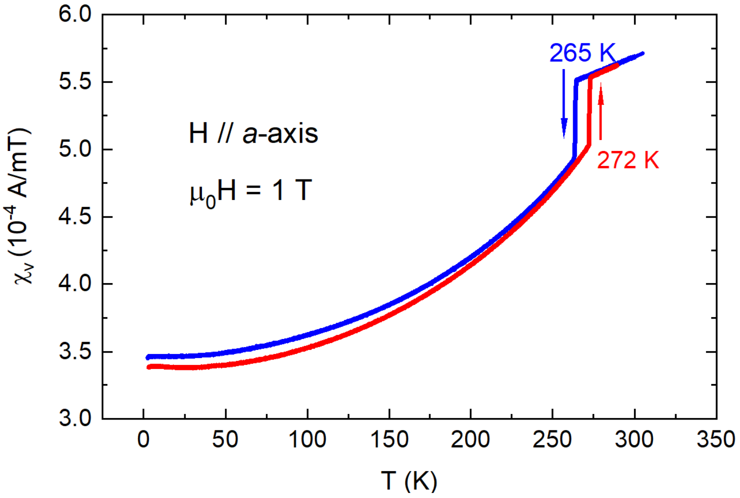

Figure 3.2.3: Magnetic volume susceptibility (χ_v) of CrAs as a function of temperature during cooling (blue line) and warming (red line).

3.2.3 Raman scattering

Raman scattering measurements were performed on single crystals of CrAs in backscattering geometry using a Jobin-Yvon LabRAM HR evolution spectrometer which is introduced in Sec. 2.6. A He-Ne laser with wavelength 632.8 nm was focused through a 50× microscope objective onto the crystal facets. Natural crystal surfaces were used in all experiments (after polishing, the sample shows weak and broadened phonons, indicating amorphousness introduced by the polishing process). The laser spot size is of ≈ 5 μm and the laser power was controlled to be ≈ 1 mW to limit laser-induced heating.

Temperature-dependent Raman response was measured with different polarization configurations. The experiments have two main focuses, *i.e.*, phononic and magnetic Raman scattering. The high-resolution mode (grating 1800 grooves/mm) was used to analyze the optical phonons, whereas the magnetic excitations were measured with the low-resolution mode (grating 600 grooves/mm), in order to maximize the signal throughput. The total energy resolutions of the spectrometer are 0.6 cm^{-1} for high grating and 1.54 cm^{-1} for low grating, which are determined from the direct measurement of the resolution limited Ne emission lines.

Prior to the experiment, Raman-active optical modes of CrAs were determined following the *nuclear site group analysis* introduced in Sec. 2.2.3. CrAs crystallizes in the centrosymmetric orthorhombic structure with space group $Pnma$, and remains so until the base temperature. It has point group of D_{2h}, and contains 4 Cr- and 4 As-atom per unit cell. The site symmetry of each set of four equivalent points and the corresponding irreducible representations are summarized in Tab. 3.1. The 8 atoms in the unit cell give rise to 24 zone-center vibrational modes

$$\Gamma = 4\mathrm{A}_g + 2\mathrm{A}_u + 2\mathrm{B}_{1g} + 4\mathrm{B}_{1u} + 4\mathrm{B}_{2g} + 2\mathrm{B}_{2u} + 2\mathrm{B}_{3g} + 4\mathrm{B}_{3u}, \tag{3.1}$$

from which 12 are Raman active

$$\Gamma_{Raman} = 4\mathrm{A}_g + 2\mathrm{B}_{1g} + 4\mathrm{B}_{2g} + 2\mathrm{B}_{3g}. \tag{3.2}$$

Table 3.1: Atomic site symmetries and corresponding normal modes in CrAs

Atom	Site symmetry	Irreducible representations
Cr	C_s	$2\mathrm{A}_g + \mathrm{A}_u + \mathrm{B}_{1g} + 2\mathrm{B}_{1u} + 2\mathrm{B}_{2g} + \mathrm{B}_{2u} + \mathrm{B}_{3g} + 2\mathrm{B}_{3u}$
As	C_s	$2\mathrm{A}_g + \mathrm{A}_u + \mathrm{B}_{1g} + 2\mathrm{B}_{1u} + 2\mathrm{B}_{2g} + \mathrm{B}_{2u} + \mathrm{B}_{3g} + 2\mathrm{B}_{3u}$

We can now introduce the Raman tensor of each irreducible representation, and find out all possible polarization configurations of the incident and scattered light $\hat{\epsilon}_i$ and $\hat{\epsilon}_s$ by simply evaluating Eq. 2.14. Typically the polarization configurations in polarized Raman experiments are described by the Porto notation, with the form of $i(kl)j$, where i and j indicate the propagation direction of the incident and scattered beam, and k and l denote the polarization of the corresponding electric field. The Raman tensor and polarization configuration for each irreducible representation can be found in Tab. 3.2.

Table 3.2: Raman tensor and polarization configuration of Raman-active modes of CrAs

Irreducible representations	A_g	B_{1g}	B_{2g}	B_{3g}
Raman tensor	$\begin{pmatrix} a & 0 & 0 \\ 0 & b & 0 \\ 0 & 0 & c \end{pmatrix}$	$\begin{pmatrix} 0 & d & 0 \\ d & 0 & 0 \\ 0 & 0 & 0 \end{pmatrix}$	$\begin{pmatrix} 0 & 0 & e \\ 0 & 0 & 0 \\ e & 0 & 0 \end{pmatrix}$	$\begin{pmatrix} 0 & 0 & 0 \\ 0 & 0 & f \\ 0 & f & 0 \end{pmatrix}$
Polarization configuration	xx, yy, zz	xy, yx	xz, zx	yz, zy

After having identified the Raman-active modes and corresponding polarization configurations, we need theoretical estimations to verify the Raman lines observed in the spectra. To this aim, density functional calculations were carried out for CrAs, using the mixed-basis pseudopotential method [136]. The electron-core interaction is represented by norm-conserving pseudoporentials with nonlinear core corrections, and semicore states Cr-3s, Cr-3p, and As-4s are included. The mixed-basis set consists of plane waves and localized functions, in our case, local functions of s, p, and d type at the Cr sites, which allows an efficient description of more localized components of the valence states, and also lower cut-off energy (24 Ry *i.e.*, 326.5 eV) and a smaller number of basis functions [137]. We used the Perdew-Burke-Ernzerhof (PBE) parameterization of the generalized gradient approximation (GGA) for the exchange-correlation functional [138], and performed Brillouin zone integrations with a $8 \times 12 \times 8$ orthorhombic k-point grid in conjunction with a Gaussain smearing of 0.1 eV. In the mixed-basis scheme, zone-centered phonons were calculated by density functional perturbation theory [137, 139]. Prior to the phonon calculations, internal structural parameters were relaxed, ensuring the system energy is at a minimum. The resulting frequencies and eigenvectors of the Raman active phonon modes are presented in Fig. 3.2.4.

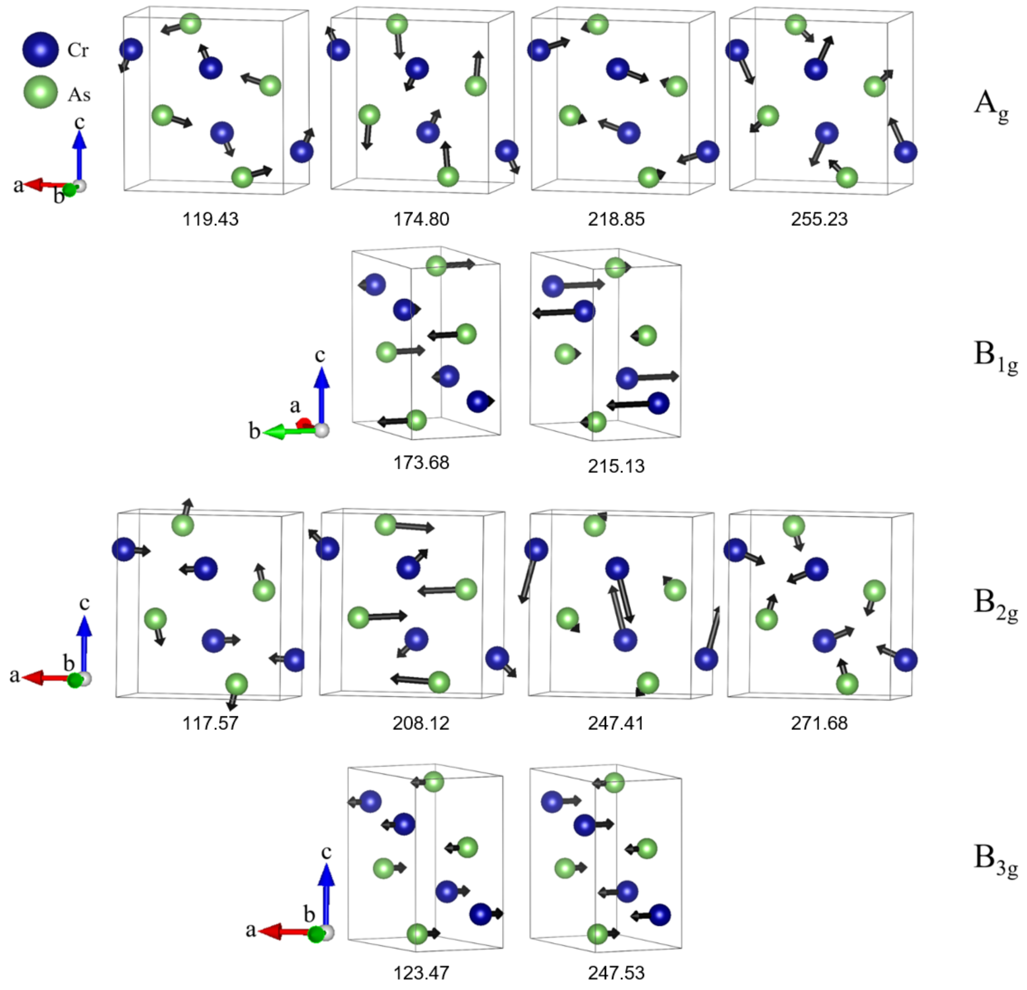

Figure 3.2.4: Schematic representations of CrAs active Raman modes. Phonon eigenvectors are represented by black arrows, and corresponding phonon frequencies are written below the figure (unit: cm^{-1}). The irreducible representations are indicated on the right side of each row.

3.3 Experimental results

3.3.1 Raman-active phonons

Previous section has shown the 12 Raman-active optical modes of CrAs and corresponding polarization configurations (Eq. 3.2 and Tab. 3.2). To probe B$_{3g}$ phonons one is required to stand the needle-like sample along the a-axis and pin-point the b-, c-axis, which vary from sample to sample as shown by Laue measurements, therefore, the B$_{3g}$ phonons have not yet been studied.

With crossed polarization configuration, where the polarization of the incoming photon is parallel to the crystallographic a-axis, both B$_{1g}$ and B$_{2g}$ phonons are probed. The Raman spectra at high-temperature (310 K) and low-temperature

(10 K) is shown in Fig. 3.3.1. For total 6 Raman-active phonons, 4 are strong enough for observation. By comparing with the theoretical estimations (shown in Fig. 3.2.4), they can be referred to as B_{1g}-1 (151.9 cm^{-1}), B_{2g}-1 (108.4 cm^{-1}), B_{2g}-3 (239.1 cm^{-1}) and B_{2g}-4 (298.0 cm^{-1}), respectively. As we can see, these vibrational modes are very weak in intensity and show little temperature dependence, as a result, are also neglected in our current work. We have, therefore, restricted ourselves to the study of the fully symmetric A_g modes.

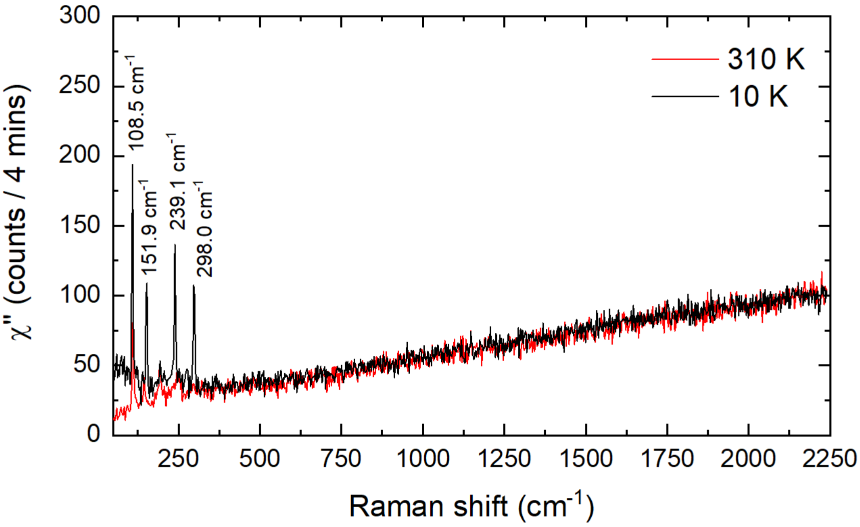

Figure 3.3.1: Raman spectra in crossed polarization geometry at 310 K and 10 K. This configuration probes both B_{1g} and B_{2g} phonons. Out of 6 Raman-active phonons with these symmetries, 4 were detected and assigned accordingly.

With parallel polarization configuration, where polarizations of both incoming and scattered photon are along the crystallographic a-axis, we measured the temperature dependence of the Raman response of CrAs with A_g symmetry, irrespective of the facet of the crystal on which they are measured (in Appendix. B we show that the Raman signal demonstrates no dependence on crystal facets). In Fig. 3.3.2 representative Raman spectra at two temperatures above and below the magnetostructural transition (T_N = 265 K) is plotted. At 310 K, all four expected A_g modes were detected in the low-energy regime and can be assigned as A_g-1 (118.9 cm^{-1}), A_g-2 (178.8 cm^{-1}), A_g-3 (227.6 cm^{-1}) and A_g-4 (265.0 cm^{-1}), respectively. Noticeably, the A_g-1 mode is almost an order of magnitude more intense than the other three modes. Upon cooling, all four phonons show drastic renormalizations across T_N, and additionally, two broad features at higher energies start to emerge. These two new peaks are argued to be of magnetic origin and will be addressed in the next part.

We now take a look at the detailed analysis of the temperature dependence of the frequency and linewidth (FWHM) of the A_g modes, all of which can be fitted with Voigt profiles, and no Fano asymmetry is present. The extracted results are presented in Fig. 3.3.3, where the solid red lines are the fitting results using the anharmonic model introduced in Sec. 2.2.4.

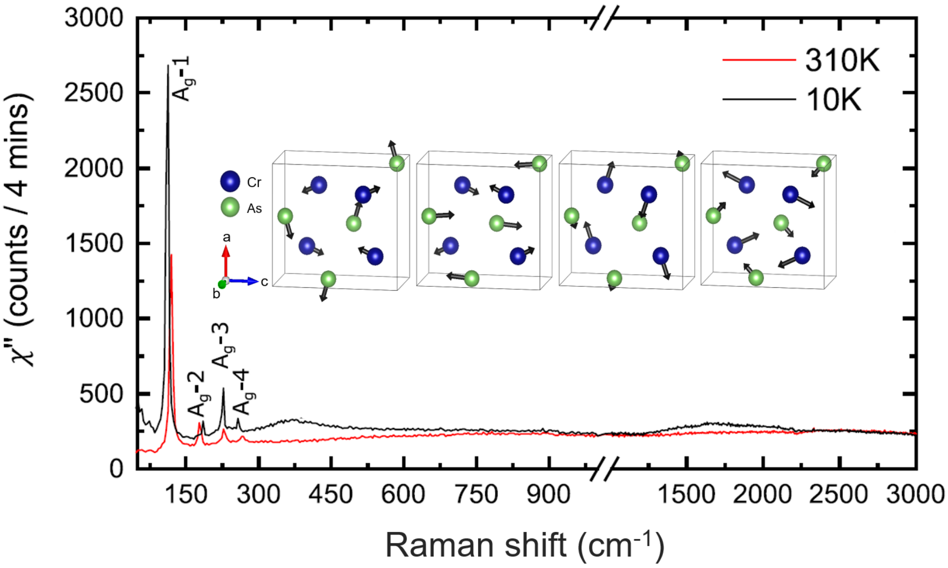

Figure 3.3.2: Raman response of CrAs with the A$_g$ symmetry at two temperatures below and above the magnetostructural transition at $T_N = 265$ K. In the low-energy regime, all four expected A$_g$ modes are present. Below T_N, the phonons are renormalized and two broad features at higher energies are present. The insets show the eigenvectors of the four phonon modes.

We first restrict ourselves to the trend of the phonon frequencies and find that the corresponding temperature dependence can be well described by the anharmonic model both above and below T_N. All phonon modes harden continuously as the temperature decreases, then a sudden renormalization of the phonon frequencies was observed across T_N, as expected from the strong first-order nature of the phase transition. Phonon A$_g$-1, A$_g$-3, and A$_g$-4 are softened significantly below the transition, while the A$_g$-2 mode hardens slightly. The percentage of the phonon frequency change is calculated simply by $\Delta w/w = (w_{T<T_N} - w_{T>T_N})/w_{T>T_N}$. We note that the softening of A$_g$-1 mode is surprisingly strong that renders an unusually large Grüneisen parameter of $\gamma_{A_g-1} \approx 5.3$, instead of a typical value of ~ 2, calculated from the Grüneisen's law [141, 142], which relates the phonon frequency with the unit-cell volume by $\Delta w_i/w_i = -\gamma_i \Delta V/V$.

Another important feature is the rate of change of the phonon frequency above and below T_N. The blue dotted lines below T_N in Fig. 3.3.3.(a)-(d) represent the slopes of the frequency variation (dw/dT) above T_N. Except for A$_g$-2, where the rate of hardening shows very little difference, all other phonons display significantly slower hardening in the magnetic phase. Quantitatively speaking, the change of the phonon frequencies of all the modes from T_N towards base temperature, around 2-4 cm^{-1}, is rather normal, on the other hand, the change between room temperature and T_N, *i.e.*, within merely 30 K, exhibiting similar amplitude, is particularly striking. Therefore, this unusual strong temperature dependence is evident for an anomalously large lattice anharmonicity in the paramagnetic phase.

We shift our focus now on the phonon linewidth and find equally, if not more,

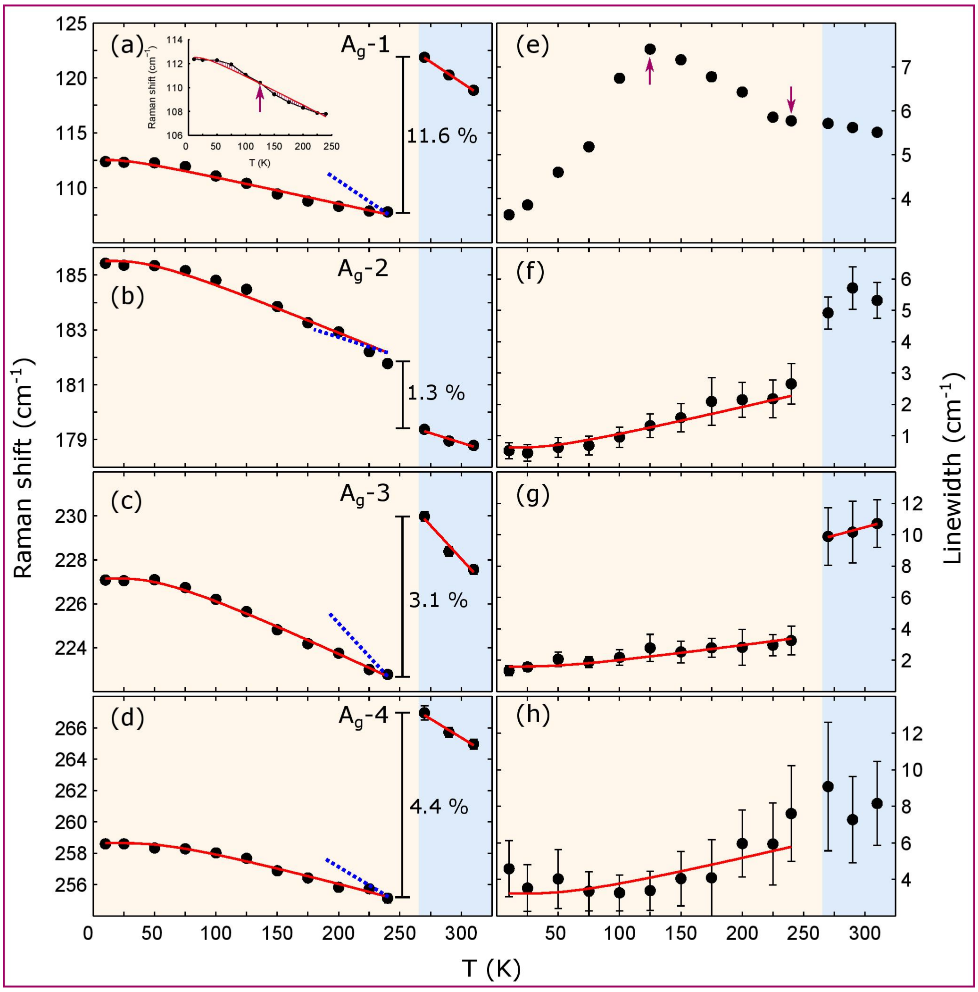

Figure 3.3.3: (a)-(d) Temperature dependence of the Raman shift for the four A_g modes. (e)-(h) Temperature dependence of the corresponding linewidth. The red solid lines are theoretical fitting by the anharmonic model. The dotted blue lines in (a)-(d) below T_N represents the slop of the change of phonon frequencies. The figure is taken from Ref. [140].

intriguing features in their behaviors. First, we note that at the base temperature the residual phonon linewidths are very small (0.5 cm^{-1} for the A_g-2 mode and 2-4 cm^{-1} for other modes, including the ones with B_{1g} and B_{2g} symmetries), which confirms the high quality of the single crystals under investigation. Second, a clear deviation from the standard behavior is manifested in the A_g-1 phonon linewidth as a function of temperature. Differently from A_g-2 and A_g-3 modes, whose linewidth can be well fitted by the anharmonic model, and display a sudden drop of more than 50% across T_N (the intensity of A_g-4 mode is too weak to allow a reliable determination of the linewidth), the linewidth of A_g-1 mode shows no abrupt change across the magnetic transition, and in addition, broadens anomalously upon cooling until $T \approx 125$ K, far below T_N, and then rapidly narrows down upon further cooling till the base temperature. This behavior is believed to be closely related to the magnetic structure of the system. Before discussing in length the origin of this anomalous phenomenon, we briefly introduce another set of Raman-active excitations which is regarded as evidence of magnetic Raman scattering.

3.3.2 Magnetic Raman scattering

In the representative spectra shown in Fig. 3.3.2, two broad features were observed at 10 K at higher energy ≈ 350 and 1700 cm^{-1}, that are absent at 310 K. In Fig. 3.3.4.(a) a detailed temperature dependence of the lower energy mode (≈ 350 cm^{-1}) is presented. By subtracting the 310 K Raman spectrum (after the phonon contribution is subtracted), we obtained the temperature-dependent part of the Raman response $\Delta\chi'' = \chi''(T) - \chi''(310K)$ in the spectral range between 150 and 750 cm^{-1}. The resulted $\Delta\chi''$ is shown in Fig. 3.3.4.(b), where the 350 cm^{-1} feature emerges clearly just below T$_N$, and evolves into sharper and more intensive peak upon further cooling. For a qualitative comparison, we extracted the spectral weight of $\Delta\chi''$ by integrating between 150 and 750 cm^{-1}, and plotted the results together with the shifted magnetic susceptibility curve $|\chi_v(T) - \chi_v(T_N)|$ as shown in Fig. 3.3.4.(c). The perfect agreement strongly indicates a magnetic origin of this excitation.

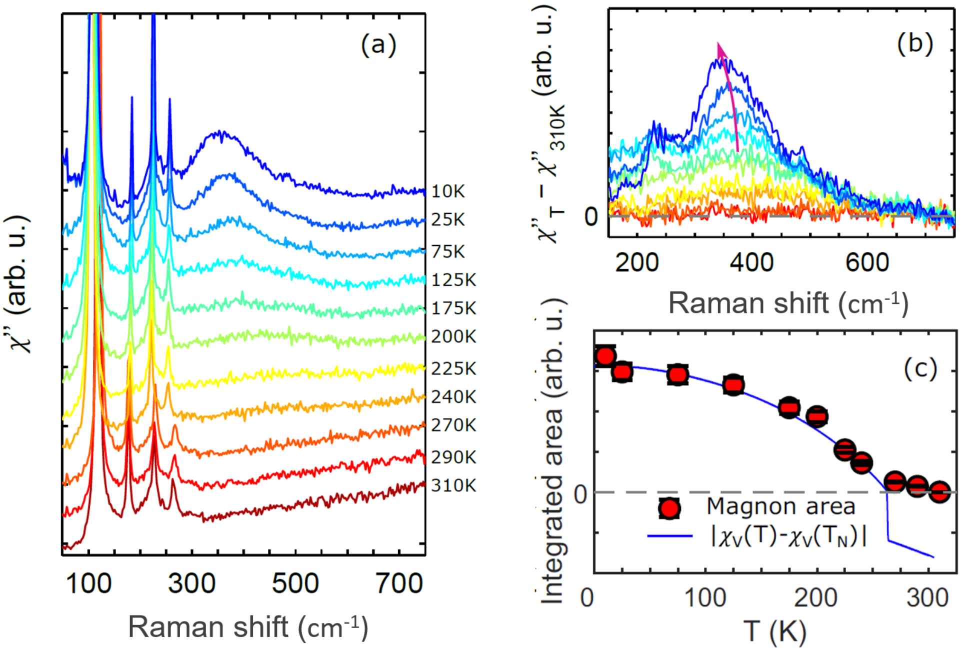

Figure 3.3.4: (a) Detailed temperature dependence of the normalized Raman response (χ''). (b) Temperature-dependent part of the Raman response $\Delta\chi'' = \chi''(T) - \chi''(310K)$. All spectra prior to subtraction have been subtracted by the phonon contributions. The arrow marks the distinctive softening of the 350 cm^{-1} mode. (c) Red circles show the integrated area under the curves in (b) as a function of temperature, and the solid line is the shifted magnetic susceptibility (cooling curve) χ_v. The figures are taken from Ref. [140].

A more subtle feature around 230 cm^{-1} was observed at the lowest temperatures, when its intensity is sufficiently strong, and in addition the 350 cm^{-1} excitation is narrow enough for the mode to be resolved. All these features were only observed in the parallel polarization configuration, and completely absent in crossed polarization as can be seen in Fig. 3.3.1. This is proven in Appendix. C to be consistent with the results calculated from the Fleury-London magnetic light scattering Hamiltonian that is introduced in Sec. 2.3.

3.4 Discussion

3.4.1 Phonon renormalization across T_N

We have shown in Fig. 3.3.3 that the Raman-active A$_g$-phonons are dramatically renormalized across the first-order magnetic transition, accompanied by a significant structural anomaly. We attempted at first to explain the shift in phonon frequencies by pure lattice renormalization, and compare the experimental values with the calculated ones using the first-principles method as introduced in Sec. 3.2.3, and the lattice parameters (see Tab. A.1) obtained by X-ray diffraction at corresponding temperatures. This first trial was carried out without considering the long-range magnetic order of CrAs, and the results are represented by green circles shown in Fig. 3.4.1. When comparing the experimental (indicated by the black line) and calculated phonon frequencies at both temperatures, a relatively good agreement ($< 5\%$) is found for A$_g$-3 and A$_g$-4 phonons, while the calculations for A$_g$-1 and A$_g$-2 modes show significant deviations from the experimental values, $\sim$ 15% - 18% off (depending on the temperatures) for A$_g$-1 and $\sim$ 8% - 10% off for A$_g$-2.

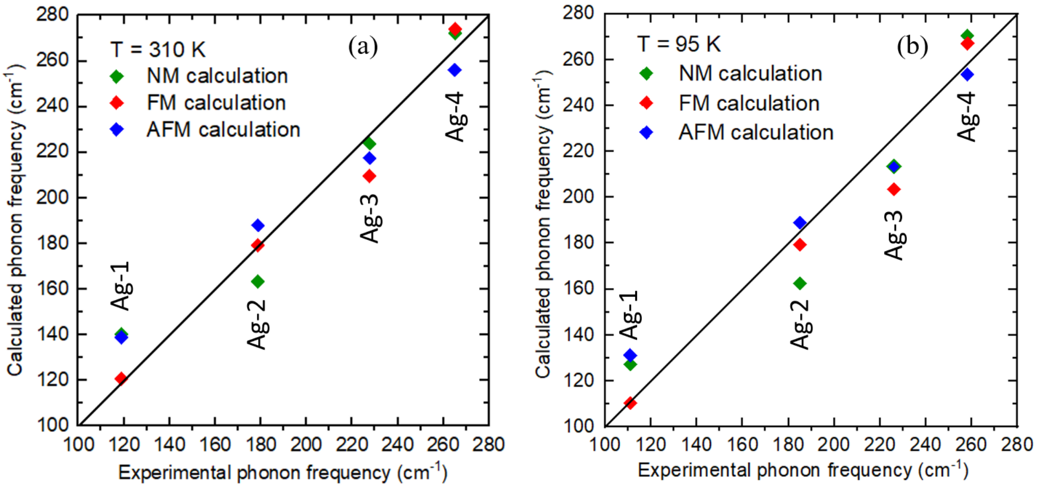

Figure 3.4.1: Comparison between the experimental phonon frequencies (indicated by the diagonal line) and the calculated value in nonmagnetic (NM), ferromagnetic (FM), and antiferromagnetic (AFM) environments at (a) 310 K and (b) 95 K. The slop of the experimental data line is set to be 1, therefore, the closer are the dots to the line, the more accurate are the theoretical calculations.

This discrepancy can be traced back to the difference between the experimentally determined bond lengths and bond angles in the unit cell (marked in Fig. 3.4.2.(a)) and the calculated ones. We show their comparison at both temperatures in Fig. 3.4.2.(c)-(d). While most bond lengths show agreement with the experimental values within ≈ ± 2%, the Cr-Cr bond B6 is 5% too short in the calculation. Similarly, the Cr-As-Cr bond angle A1 is also underestimated by 3.16°, whose renormalization happens to be dominated by the eigendisplacements of the A_g-1 and A_g-2 modes. More importantly, bond length B6 and bond angle A1 are directly related to the dominant magnetic exchange path, indicated as J_{c2} in Fig. 3.4.5. This clearly demonstrates a significant role of magnetism in the lattice dynamics in CrAs, and calls for an inclusion of magnetism in the phonon calculations. To include the actual double-helical magnetic structure of CrAs is, however, more than difficult based on two reasons: i) noncollinear magnetic order is often not implemented in the spin polarized DFT calculation codes; ii) more importantly, a magnetic super cell with a finite size is typically required for such calculations, while the incommensurate magnetic order of CrAs renders an infinitely large magnetic unit cell. Although certain approximations can be made, this implementation is beyond the scope of the present work. For simplification, we imposed FM and AFM orders on the Cr atoms, and calculated the phonon frequencies, after relaxing the atomic positions in the unit cell. In this way, we can qualitatively evaluate the impact of magnetism on the structural parameters, and subsequently, on the phonon frequencies. From the calculations, we find that the GGA functional overestimates the magnetic moment on Cr atoms to a great deal, in agreement with a previous study [143]. The theoretically obtained value is 2.4 (~ 2.3) μ_B/Cr below T_N for the FM (AFM) order.

As can be seen from Fig. 3.4.2.(b)-(d), the inclusion of magnetism systematically improved the agreement between the calculated structural parameters with the experimentally determined ones. For both bond lengths and bond angles, the calculations considering AFM order shows better agreement than the FM case. Interestingly, the FM order seems to induce deviations to the experimental values in an opposite manner compared to that in the NM case. Bond lengths that are underestimated in the NM calculations shown in Fig. 3.4.2.(c)-(d) are now slightly overestimated and vice versa. On the other hand, for the bond angles, while angle A2 and A4 seem to be under marginal effect by magnetism, A1 (A3) is significantly overestimated (underestimated) by the FM calculation. But more importantly, the agreement between the FM/AFM calculations and the experiments is generally better than that of the NM calculation.

As a consequence, the calculated phonon frequencies are also found to have better agreement with the experimental values as shown in Fig. 3.4.1. With the inclusion of FM, A_g-4 is only slightly affected, while A_g-1, A_g-2, and A_g-3 are strongly renormalized, and the former two show excellent agreement with the experimental results (within ≈ 3%). On the other hand, the inclusion of AFM has an effect mostly on the A_g-2 and A_g-4 modes, leaving A_g-3 slightly affected at the high temperature and A_g-1 almost unmodified compared to the NM case.

It is certainly very complex to determine the relationship between the struc-

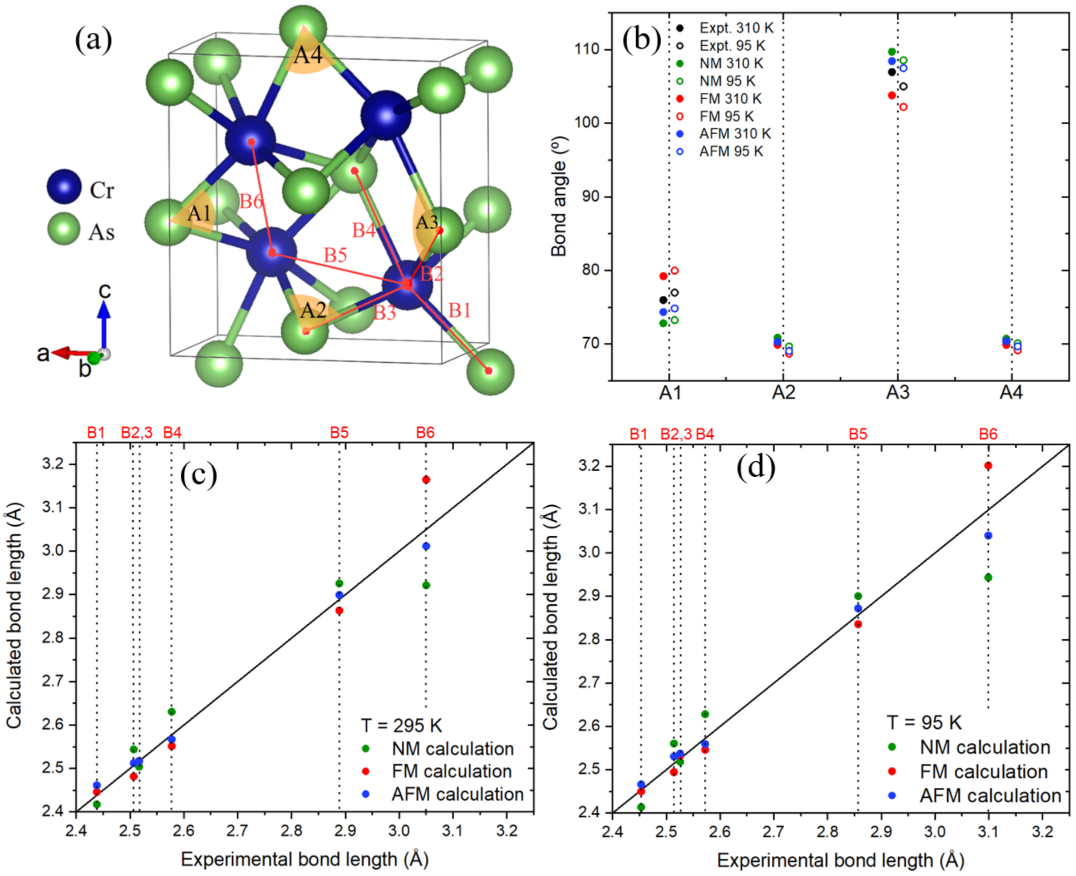

Figure 3.4.2: (a) A sketch of the CrAs unit cell with labels of the bond lengths and bond angles under investigation. (b) Comparison of the experimental values of the bond angles with the theoretical calculations at 310 K and 95 K in nonmagnetic (NM), ferromagnetic (FM), and antiferromagnetic (AFM) environments. (c) Comparison of the experimental values of the bond lengths with the theoretical calculations at 310 K. (d) The corresponding comparison at 95 K.

tural and magnetic degrees of freedom within CrAs, but qualitatively, the inclusion of magnetism shows the strongest impact on the structural parameters that modulate the exchange paths J_{c2} (AFM) and J_{c1} (FM), which subsequently has a dramatic effect on the calculated phonon frequencies. This connection clearly demonstrates a strong coupling between spin and lattice degrees of freedom, and more importantly, this conclusion is valid both below and above the magnetic transition. This is of strong reminiscence of the behavior of iron-based superconductors [144, 145], where the calculations of the phonon frequencies and dispersion relations agree the best with the experimental value with the inclusion of magnetic order, even in the paramagnetic phase. It is, therefore, expected that when taking into account the actual double-helical magnetic structure, which compromised between the FM and AFM orders but is currently beyond our computational capabilities for lattice dynamic calculations, the results will produce the best agreement with the experiment.

Finally, we note that although the recapture of the phonon frequencies requires the inclusion of magnetism, the relative change $\Delta w/w = (w_{95K} - w_{310K})/w_{310K}$ of the phonon frequency across T_N can already be well reproduced even in the NM calculation, namely, the large Grüneisen parameter of the A$_g$-1 mode does not have a magnetic origin. To qualitatively understand the reason behind the unusually large phonon renormalization, we point out that this A$_g$-1 mode belongs to the branch that gets completely soft at the zone boundary (M point) of the high-temperature hexagonal unit cell, when the structural phase transition to the orthorhombic phase occurs at 1173 K, at which point this M point backfolds to the zone center. In Fig. 3.4.3 we plotted the phonon dispersion curves of CrAs in the hexagonal phase, where the strongest instability at the M point can be clearly observed. This situation is very close to that of MnAs, in which the system undergoes a first-order transition from a hexagonal FM phase to an orthorhombic PM phase at 315 K. The lowering of crystal symmetry is argued to be induced by the soft mode through a giant spin-phonon coupling [146]. In the case of CrAs, the amplitude of the structural orthorhombicity, which is defined as c/b ($\sqrt{3}$ in the hexagonal phase), increases from 1173 K down to T_N and suddenly changes its sign below the magnetic transition. Energetically the low-temperature structure of CrAs is very close to its hexagonal phase, therefore, it is natural to assume that the sudden change in orthorhombicity strongly affects the soft-branch to which the A$_g$-1 mode belongs.

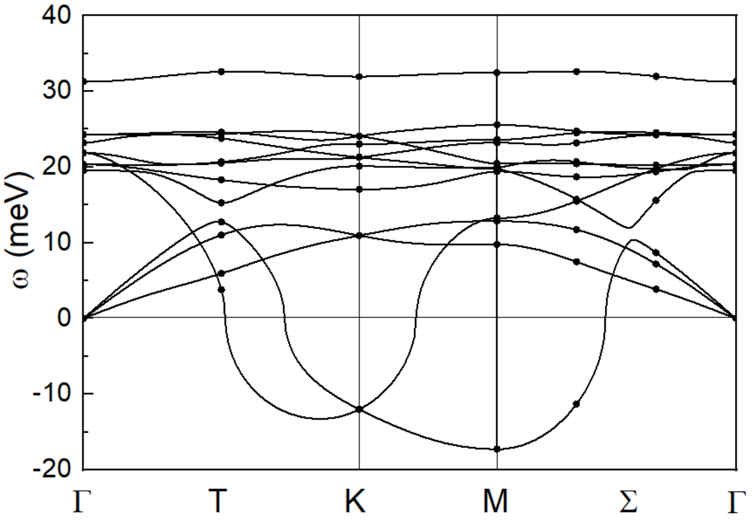

Figure 3.4.3: First-principlec calculations of the phonon dispersion relations for the hexagonal phase of CrAs. The strongest instability is observed at the M point.

3.4.2 Impact of spin-phonon coupling on phonon lifetime

After establishing the importance of magnetism on the calculation of phonon frequencies even above T_N, we now consider its possible influence on the phonon linewidths. As shown in Fig. 3.3.3, the FWHMs of A$_g$-2 and A$_g$-3 modes show a singular behavior, exhibiting through the marked jump across T_N. This behavior is very similar to that of the magnetization and also that of the electrical resistivity $\rho(T)$ as reported in Ref. [57, 59]. To gain more insight, we note that there are studies on other magnetic metals linking $\rho(T)$ with the line shape of Raman-active phonons, in particular, on the parent compounds of iron-based superconductors such as $BaFe_2As_2$ [147, 148]. As shown in Fig. 3.4.4.(a), the FWHM of the A$_{1g}$ mode of $BaFe_2As_2$ drops rapidly and continuously below the spin density wave (SDW) transition temperature T_s, which remarkedly resembles the $\rho(T)$ measurements as plotted in Fig. 3.4.4.(b). This phenomena is understood to be attributed to the reduction of electron-phonon interaction resulted from the opening of a SDW gap in the electronic density of states, evident by the repression of reflectivity $R(w)$ below T_{SDW} in optical spectroscopy measurements [147]. In this context, to better understand the origin of the linewidth anomalies in CrAs, further investigations are needed using, *e.g.*, angle-resolved photoemission spectroscopy on changes in its electronic structure across T_N, and subsequently on that in P-doped CrAs, where the substitution strongly affects $\rho(T)$ [59].

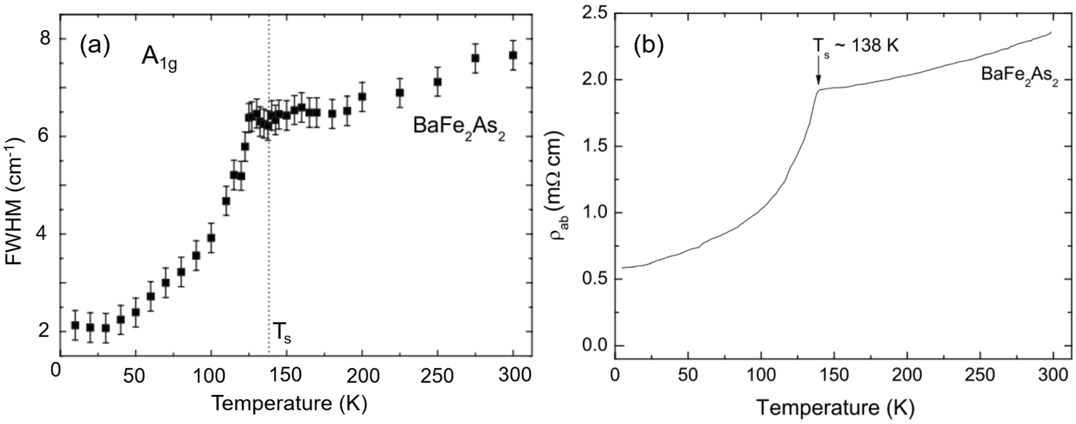

Figure 3.4.4: (a) FWHM of the A$_1g$ mode of $BaFe_2As_2$, which drops pronouncedly and continuously below the spin density wave transition temperature T_s. (b) Resistivity of $BaFe_2As_2$ in the *ab*-plane as a function of temperature. The figures are taken from Ref. [148].

On the other hand, the linewidth of the A$_g$-1 mode, as shown in Fig. 3.3.3.(e), exhibits a totally different temperature dependence, with a cusplike shape peaking at ≈ 125 K. We note that this temperature does not coincide with any known anomaly in the structural or thermodynamic properties of CrAs, which in turn suggests that such an unusual temperature dependence arises from a compromise between orders with opposite effects below T_N. As already established previously that A$_g$-1 mode is highly sensitive to the underlying magnetism, the spin-phonon coupling can thus be a possible damping factor below T_N, which is partially compensated at low temperatures by the regular phonon-phonon interaction. The effect of spin-phonon coupling on phonon frequencies has since long been studied in several systems [149–151], its effect on the phonon linewidth, however, was barely discussed. Recent studies on antiferromagnetic $Pr_{1-x}Ca_xMnO_3$ [152], $SmCrO_3$, and $GdCrO_3$ [153, 154] have reported similar phonon broadenings below the magnetic transition, a robust theoretical framework to explain such a generic phenomenology is, nevertheless, still missing.

3.4.3 Magnetic Raman scattering

The excitations at higher energies around 350 and 1700 cm^{-1} emerge only below the magnetic transition, and since no additional phonon modes are expected in the absence of broken translational symmetry, they are argued to have a magnetic origin. The mechanism behind magnetic Raman scattering has already been introduced in Sec. 2.3, and we note here that one-magnon Raman scattering typically gives rise to sharp low-energy peaks, while two-magnon scattering generally results in broader features. Therefore, it is natural to suspect the two-magnon origin of the extra excitations in CrAs below T_N based on their large FWHMs.

As the two-magnon scattering arises from the exchange coupling mechanism (introduced in Sec. 2.3), it is intuitive to estimate the exchange coupling constant in turn from the two-magnon Raman spectra. It has been successful in the case of the parent compound of high-T_c cuprates [100], which are $S = 1/2$ antiferromagnets on square lattices. For a more general case of a noncollinear magnet such as CrAs, however, it is much more complicated to interpret. In principle, the two-magnon energy can be calculated in two ways: (1) evaluate the energy cost of two neighboring spin flips (*i.e.*, Eq. 2.45); (2) compute the M-DOS (Eq. 2.43). However, both cases encounter difficulties brought by the noncollinearity and the itinerant character of the system such as unable to determine final-state interactions [155]. In addition, the actual spin contribution to the total magnetic moment (1.73 μ_B/Cr) is not precisely known. With a large orbital contribution ($\sim$ 60%) to the total magnetic moment of metallic Cr [156], it is strongly suggested that the spin in CrAs might be larger than 1/2.

The magnetic strucure of CrAs has already been modeled using a Heisenberg-like Hamiltonian $H = \sum_{i,j} J_{ij}\tilde{\mathbf{S}}_\mathbf{i} \cdot \tilde{\mathbf{S}}_\mathbf{j}$ [56, 59], where J_{ij} contains the leading exchange couplings up to the fourth nearest neighbors which are denoted as J_a, J_b, J_{c1} and J_{c2} as shown in Fig. 3.4.5.(c). Note that J_b couples the magnetic moments of the same sublattice in the nearest-neighbor unit cells along the crystallographic b-axis. To maintain a stable condition for the double-helical magnetic ground state, the ratio between the exchange couplings have been determined as $J_{c2}/J_a = 7.1$ and $J_{c1}/Ja = -0.52$ [56], regardless of the value and sign of J_b (based on the ratio of the Cr-Cr distances along a and b axis we approximated that $J_a/J_b \approx 1.26$). The values of the exchange couplings, however, are not precisely known, and have been estimated only from inelastic neutrons scattering measurements performed on polycrystalline samples [59], where the total magnetic excitation bandwith ($\sim$

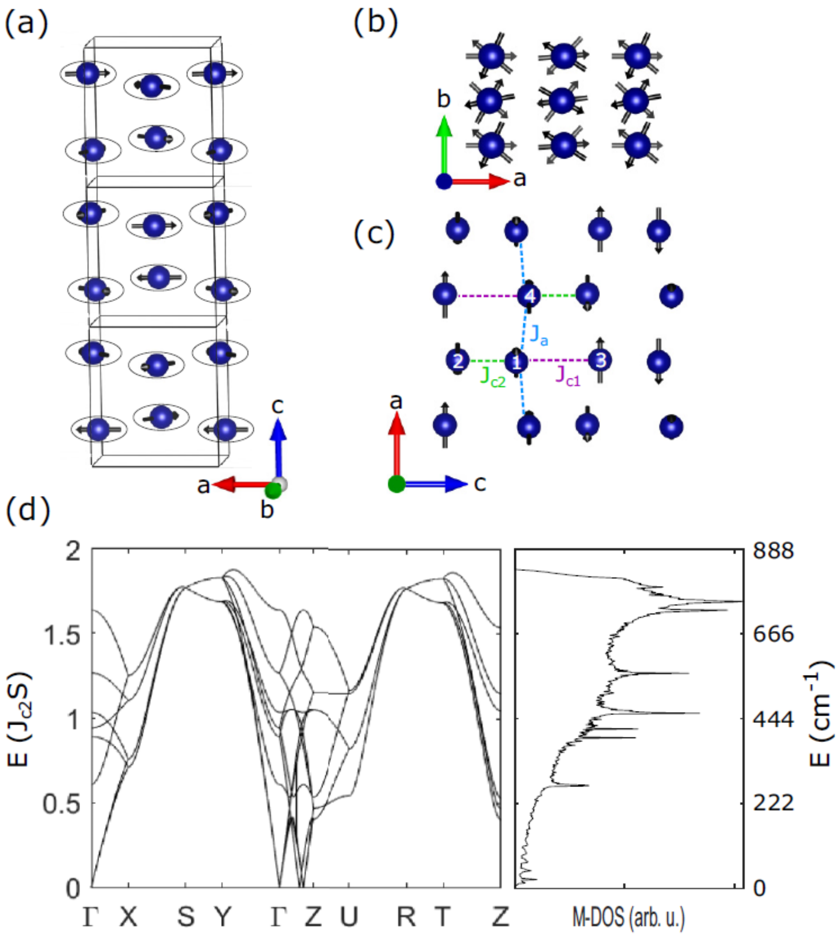

Figure 3.4.5: (a) The double-helical magnetic ground state of CrAs with propagation vector of (0, 0, 0.36). (b) A view of the magnetic structure along the crystallographic c-axis. (c) The magnetic ground state of CrAs with the marked magnetic exchange couplings on the crystallographic ac-plane. (d) On the left is the magnon dispersion along the high-symmetry directions in reciprocal space in units of $J_{c2}S$ and on the right is the corresponding M-DOS with additional units of cm^{-1}. The figures are taken from Ref. [140].

110 meV) is assumed to be dominated by $J_{c2} \gg J_{c1}$, J_a, and could be roughly expressed as $2J_{c2}S$. Using these estimated exchanging parameters, we calculated the linear spin-wave spectra of CrAs [157] and the corresponding M-DOS as shown in Fig. 3.4.5.(d) in units of $J_{c2}S$. The latter clearly indicates a dominated feature in the magnetic Raman response at the energy around $1.7J_{c2}S$, and amounts to 93.5 meV (754 cm^{-1}) based on the estimation from Ref. [59]. This value is doubled in the two-magnon scattering process, *i.e.*, 187 meV or 1508 cm^{-1}, and is relatively close to the energy of the feature at 1700 cm^{-1}. However, the excitation around 350 cm^{-1} can not be easily associated with any of the other features of the M-DOS.

This brings us to the fact that linear spin-wave theory cannot correctly interpret the magnetic excitation spectra of noncollinear magnets, as nontrivial anharmonic corrections to the spin-wave spectrum for a noncollinear magnetic system already appear to the first order in $1/S$ and significantly affect the spin-wave dispersion [158]. A recent study in noncollinear antiferromagnetic $\mathrm{CaCr_2O_4}$, as an example, has verified this conclusion, in which the magnetic excitations are found to be much softer than the predicted values from the linear spin-wave theory. Therefore, to confirm the magnetic origin of these two extra excitations, an experimental investigation of the magnetic dispersion of CrAs is required.

We finally note that although in some systems such as $\mathrm{Cd_2Os_2O_7}$ [159] linear spin-wave theory produces calculations in good agreement with the magnetic Raman response, for other noncollinear magnets, for instance, α-$\mathrm{SrCr_2O_4}$ [160] or $\mathrm{Bi_2Fe_4O_9}$ [161], difficulties are encountered when interpreting the two-magnon Raman spectra. To the best of our knowledge, efforts to explain the magnetic Raman response by adding nonlinear corrections have only been made for the case of a triangular lattice [162, 163]. These corrections, however, are strongly model dependent and need to be evaluated for the specific magnetic structure of CrAs.

3.5 Conclusions and outlook

We have conducted a detailed Raman scattering study of the lattice and magnetic excitations as a function of temperature in single crystals CrAs. In our work, dramatic changes in phonon frequencies for all four A_g modes were detected across $T_N = 265$ K, at which temperature the system undergoes a first-order magnetostructural phase transition characterized by the formation of a double-helical magnetic order, accompanied by a large expansion of the unit cell without changing of the crystal symmetry. Evidence of magnetic light scattering was also reported in this itinerant noncollinear magnet. An attempt to explaining the phonon frequency renormalizations was performed through first-principles lattice structure and dynamics calculations using the experimental lattice parameters, which show a good agreement with the experimental data, especially when magnetic order (FM or AFM) is taken into account, thus suggesting a sizable spin-phonon coupling in CrAs. However, as our calculations are limited to collinear magnetic structures, which fails to capture the true behavior within the helical magnetic order, further work is required to allow quantification of these effects. In addition, we observed an anomalous temperature dependence of the linewidth of the strongest A_g mode, which shows an unusual broadening in the magnetic phase down to 125 K. An origin of coupling with the magnetic degrees of freedom is proposed, and calculations beyond the harmonic level are needed for further understanding.

Despite the difficulty in quantatively account for the observed features, we have demonstrated that Raman scattering is a useful tool to probe the strong spin-phonon coupling effect and noncollinear spin wave in CrAs. To discuss the potential relation between these effects with superconductivity, tracking the phonon anomalies and magnetic excitations as a function of hydrostatic pressure or chemical pressure (via doping) as the magnetic order is suppressed will provide important information.

Chapter 4

Raman measurements on $BaNi_2(As,P)_2$

4.1 Introduction

The discovery of superconductivity in Fe-based pnictides in 2008 with T_c pushing towards 60 K was a significant breakthrough in condensed matter physics [164–170]. Before this point, the term 'high-T_c superconductivity' was reserved only for the Cu-based superconductors. The importance of the discovery of FeSCs not only lies in their high T_c, but more importantly, in the different behaviors between these two systems. In general cuprates can be well described by an effective single-band Hubbard model, and the parent phase is an antiferromagnetic Mott insulator [171, 172]. Although the undoped phase of FeSC is also antiferromagnetic, it is metallic. And unlike cuprates, all five of the $3d$ orbitals of the iron contribute to the electronic structure near the Fermi level, the FeSCs are, therefore, multi-band superconductors [173, 174]. This discovery thus prompted the community to rethink what is really the essential ingredients for high-T_c superconductivity in different systems. Since then the properties of different members of the FeSCs have been under investigations with unprecedented speed and intensity. One of the most important discoveries is undoubtedly the ubiquitous observation of electronic nematicity in the iron-based '1111' and '122' families. This nematic phase can rise from the thermal spin fluctuations between the two degenerate spin density wave (SDW) orders along (π,0,0) and (0,π,0) above the antiferromagnetically ordered phase and subsequently breaks the C_4 rotational symmetry [32, 44, 48, 119]. Interestingly we note that the electronic nematicity might also be responsible for the anomalous phonon behavior observed in previous Raman scattering measurements. As shown in Fig. 4.1.1, E_g phonon splitting below the structural transition has been observed in pure $BaFe_2As_2$, one of the most studied iron-based SCs [20, 175–177], with an amplitude too large (~ 9 cm^{-1}) to be explained by the small orthorhombic distortion alone (it would yield a splitting of less than 1 cm^{-1}) [178]. It is thus highly plausible that the splitting is induced through a symmetry-allowed coupling between the doubly degenerate E_g mode with the Ising nematic order with the B_{2g} symmetry, and the coupling strength is then in return reflected by the phonon splitting amplitude. Within this scenario, the magnetic order seems to be a crucial element. It is then of strong motivation of us to see if similar behaviors can be detected in an analogous non-magnetic system. To this aim, $BaNi_2As_2$ can serve as the perfect candidate.

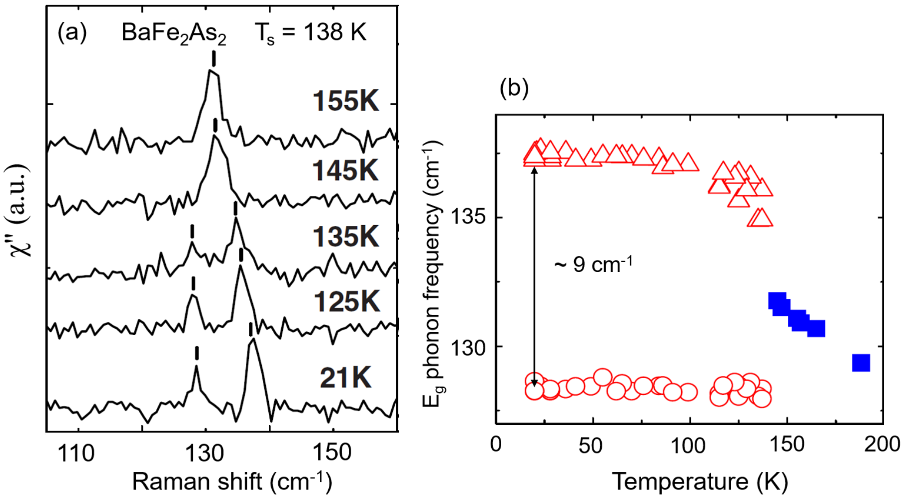

Figure 4.1.1: (a) The evolution of the E_g phonon mode of $BaFe_2As_2$ with temperature. (b) Extracted E_g phonon frequency as a function of time. The figures are taken from Ref. [178].

To begin with, $BaNi_2As_2$, a non-magnetic superconductor, has the same high-temperature tetragonal $I4/mmm$ structure as $BaFe_2As_2$. Previous studies have reported that the system undergoes a first-order structural transition from tetragonal to triclinic ($P\bar{1}$) at $T_{tri} \approx 130$ K (cooling), below which temperature a commensurate charge density wave (C-CDW) with wave vector $(1/3\ 0\ 0)_{tri}$ was observed [60–62, 179], indicating the presence of a strong electron-lattice coupling effect in this system. More importantly, a recent study on pristine $BaNi_2As_2$ has discovered a unidirectional and incommensurate charge density wave (IC-CDW) above T_{tri} with a propagation vector of $(\pm 0.28\ 0\ 0)_{tet}$[62].

Further studies by Merz *et al* [64] here in KIT on $BaNi_2As_2$, $BaNi_2(As,P)_2$ and $Ba(Ni,Co)_2As_2$ have not only revealed the robustness of the IC-CDW in doped systems, but also found a second-order structural transition at T_{oth} from tetragonal to orthorhombic with space group $Immm$ that coincides with the appearance of the IC-CDW. This unidirectional IC-CDW is thus a striking charge analogy of the unidirectional SDW in the Fe-based counterpart, and charge/orbital-fluctuation-driven electronic nematicity might play a significant role in shaping the phase diagram of the Ni-based system. A recent study on $Ba_{1-x}Sr_xNi_2As_2$ by elastoresistivity measurements has indeed reported nematic-fluctuation-enhanced superconductivity [180] with electronic nematic fluctuations present only in the B_{1g} channel, instead of the B_{2g} channel as in the case of $BaFe_2As_2$. The phase diagram and the nematic susceptibility of this system is shown in Fig. 4.1.2.(a)-(b) respectively. Upon doping, the amplitude of the nematic susceptibility follows closely the triclinic and CDW phase boundaries. More importantly, the electronic nematic fluctuations show a smooth enhancement approaching $x_c = 0.75$ from the endmemeber $SrNi_2As_2$, in excellent agreement with the T_c enhancement.

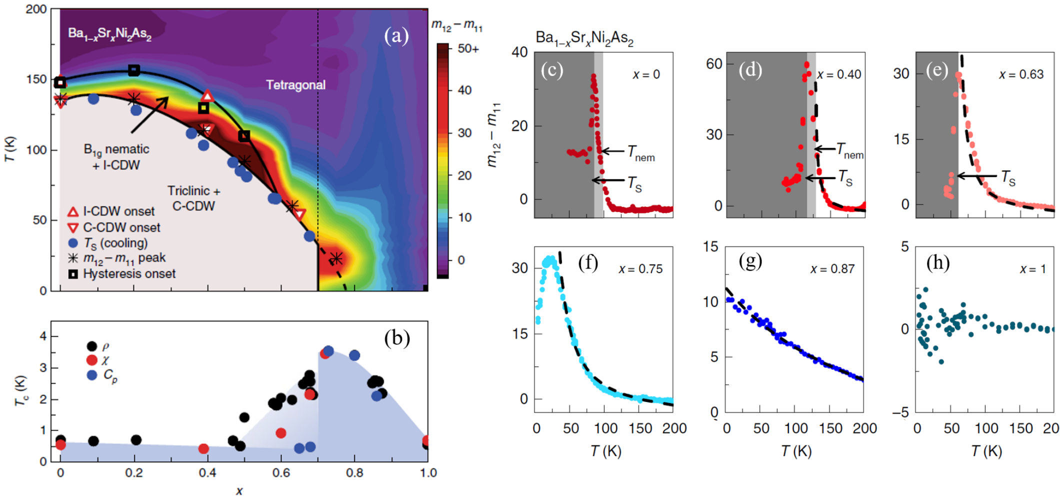

Figure 4.1.2: (a) Phase diagram of $Ba_{1-x}Sr_xNi_2As_2$ with different phase boundaries clearly marked. (b) Superconducting temperature T_c of $Ba_{1-x}Sr_xNi_2As_2$ obtained by transport (balck circles), magnetization (red circles) and hear capacity (blue circles) measurements. The light blue region indicates where superconductivity was observed in transport and magnetization measurements but absent in heat capacity measurement, while the dark blue region represents where bulk superconductivity was confirmed in all measurements. (c)-(h) B_{1g} nematic susceptibilities of $Ba_{1-x}Sr_xNi_2As_2$ single crystals with $x = 0$, 0.40, 0.63, 0.75, 0.87 and 1. The figures are taken from Ref. [180].

On the other hand, it is important to note that although $BaNi_2As_2$ is the non-magnetic analogy of $BaFe_2As_2$, the superconducting behaviors of these two systems are very different. Unlike the Fe-based counterpart, parent $BaNi_2As_2$ material already shows superconductivity, albeit with a much lower $T_c \sim 0.7$ K in the triclinic phase [60, 179]. Thermal conductivity measurements provided evidence for a fully gapped s-wave superconductivity. The specific heat jump together with the low T_c have pictured $BaNi_2As_2$ to be one of the conventional BCS type superconductors [179]. Although T_c seems to be unaffected by physical pressure up to 25 kbar [181], it can be largely enhanced (although never exceeds 5 K) by chemical substitutions. The behavior and mechanism of the T_c enhancement are strongly dependent on the substitution element, while the triclinic transition is universally suppressed. As shown in Fig. 4.1.3.(a), with cobalt substitution on the Ni-site, the critical temperature T_c increases in a dome-like manner while CDW is suppressed together with the triclinic transition by doping, which closely resembles the behavior of antiferromagnetism in its Fe-based counterpart [62]. On the other hand, Kudo *et al* [63] has reported a step-like increase in T_c with phosphorus substitution on the As-site. As can be seen in Fig. 4.1.3.(b), T_c jumps abruptly from 0.6 K in the triclinic phase to 3.3 K in the tetragonal phase across the critical doping level $x_c = 0.067$. The enhanced superconductivity was further suggested to arise from doping induced phonon softening, which is manifested in the sudden decrease in the Debye frequency w_D and logarithmic-averaged phonon frequency w_{ln} [182, 183] across x_c as shown in Fig. 4.1.3.(c). The in-plane Ni and As (P) at ~ 50 cm^{-1} as calculated in Ref. [184] was then suggested to be the responsible soft mode.

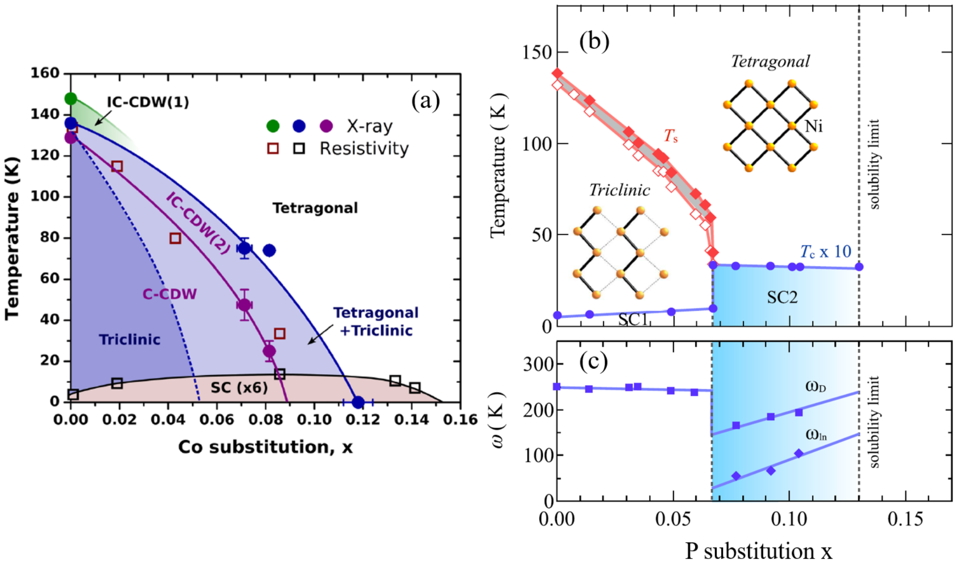

Figure 4.1.3: (a) Phase diagram of Ba(Ni$_{1-x}$Co$_x$)$_2$As$_2$. The figure is taken from Ref. [62]. (b) Phase diagram of BaNi$_2$(As$_{1-x}$P$_x$)$_2$. The red open and closed diamonds represent the structural transition temperatures upon cooling and heating, respectively. (c) The evolution of the Debye frequency w_D and the logarithmic-averaged phonon frequency w_{ln} extracted from the specific heat measurement results with phosphorus substitution. The figures are taken from Ref. [63]. Note that the values of T_c in both systems have been scaled.

It is thus evident that in the Ni-based system both electronic and lattice degrees of freedom show significant impacts on the superconductivity. To gain more insight into the enhancement of superconductivity upon doping, one is first required to obtain a more comprehensive understanding of the electronic and lattice order and the interplay between them in the normal state. To this aim, we have performed Raman scattering measurements on single crystals BaNi$_2$(As,P)$_2$ in order to study the rich electronic and lattice dynamics in this system. One of the main objectives is to search electronic nematic fluctuations and probe possible coupling effect between the nematic order and phonon mode as suggested in the case of BaFe$_2$As$_2$.

4.2 Experimental detail

4.2.1 Crystal growth

Single crystals BaNi$_2$As$_2$ were grown by Amir Haghighirad and Tom Lacmann using the self flux method [185]. NiAs as a precursor was grown in the first step.

Grinded Ni and As were weighed stoichiometrically and subsequently evacuated and sealed in a fused silica ampoule. This process was done in an Argon atmosphere to prevent oxygen or water contaminations. The mixtures were heated up to 730°C for 20 h, then the temperature was decreased rapidly to 60°C with a cooling rate of 200°C/h. Finally, we took the ampoule out of the furnace and let it cool to room temperature under natural conditions. After the ampoule was fully cooled, we extracted the grown NiAs crystals and grinded them together with small pieces of Ba with the atomic ratio Ba:Ni:As = 1:4:4. The mixtures were filled in a glassy carbon or aluminum oxide ampoule and subsequently evacuated and sealed by a fused silica ampoule under argon atmosphere and placed inside an oven. The mixtures were heated up to 1090°C in three steps and dwelled for 5 h. Afterward we cooled the oven slowly back to 995°C with a cooling rate of < 1°C/h over a period of 20 days. Finally, we turned off the oven and let the ampoule cool down to room temperature. The grown crystals were then mechanically removed from the inner ampoule and the flux.

For the more complicated growth of $\mathrm{BaNi_2(As_{1-x}P_x)_2}$, pure phosphorus or chemically bonded phosphorus ($\mathrm{Ni_5P_4}$) were added to provide the doping element. The atomic ratio Ba:Ni:As: = 1:4:4(1-x):4x was kept when pure phosphorus was concerned and 1:5:5(1-x):5x when $\mathrm{Ni_5P_4}$ was used. In the end, we obtained crystals of millimeter size with plate-like geometry and shiny metallic surface as shown in Fig. 4.2.1. The crystallographic c-axis is perpendicular to the plane as marked on the figure.

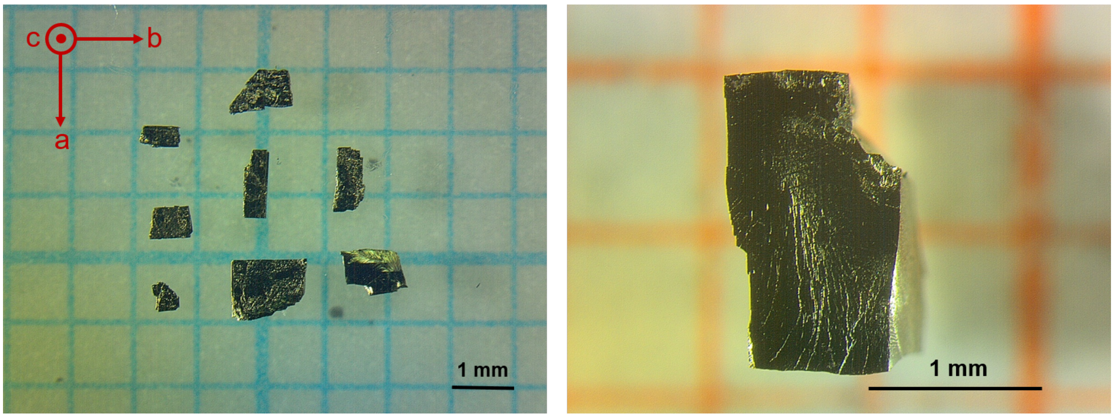

Figure 4.2.1: Pictures of the grown single crystals $\mathrm{BaNi_2(As_{1-x}P_x)_2}$.

4.2.2 Sample characterizations

Thermal expansion and X-ray diffraction measurements

All investigated crystals were characterized using single-crystal X-ray diffraction (XRD) with the same set-up as introduced in Sec. 3.2.1, and the results showed that all samples are in a single phase. The room temperature diffraction data were used to determine the phosphorus content x. Samples within the same batch and samples between different batches but with the same nominal P concentration can have different doping concentrations up to $\sim$0.5% [185].

Both temperature-dependent X-ray diffraction and high-resolution (10^{-11}-10^{-12} m) thermal expansion (TE) were exploited to study the second-order orthorhombic transition. Detailed experimental results are reported in Ref. [64], here we only give a brief summary. The orthorhombic distortion is extremely weak and only manifests itself on the diffraction image plate by a slight broadening of some Bragg peaks, but owing to the high resolution of TE, the discrepancy between the crystal's expansion along different in-plane directions ($[100]_{tet}$ and $[110]_{tet}$) presents unambiguous evidence of the loss of the high-temperature tetragonal symmetry. The TE results of pure $BaNi_2As_2$ and P-doped sample with $x = 0.035$ are given in Fig. 4.2.2.(a)-(b) respectively. The temperature at which the splitting was first detected is marked as the orthorhombic transition temperature T_{oth}. The amplitude of the discrepancy is proportional to the strength of the structural anisotropy, and as we can see, the doped sample shows clearly more pronounced orthorhombic distortion. It is important to note that while in $BaFe_2As_2$ the detwining occurs along $[110]_{tet}$ (B_{2g}), in the Ni-based systems the four-fold symmetry is broken in the B_{1g} channel with form factor $x^2 - y^2$. More detailed refinement of the structural parameters obtained from the diffraction data have shown that the effect of the orthorhombic distortion in the Ni-based systems is less about bringing discrepancy along the crystallographic a- and b-axis, but more about shifting the position of Ni- and As-atoms along the c-axis, thus resulting in different Ni-As bond lengths within the NiAs tetrahedron and lifting the degeneracy between the d_{xz} and d_{yz} orbitals of the Ni atom.

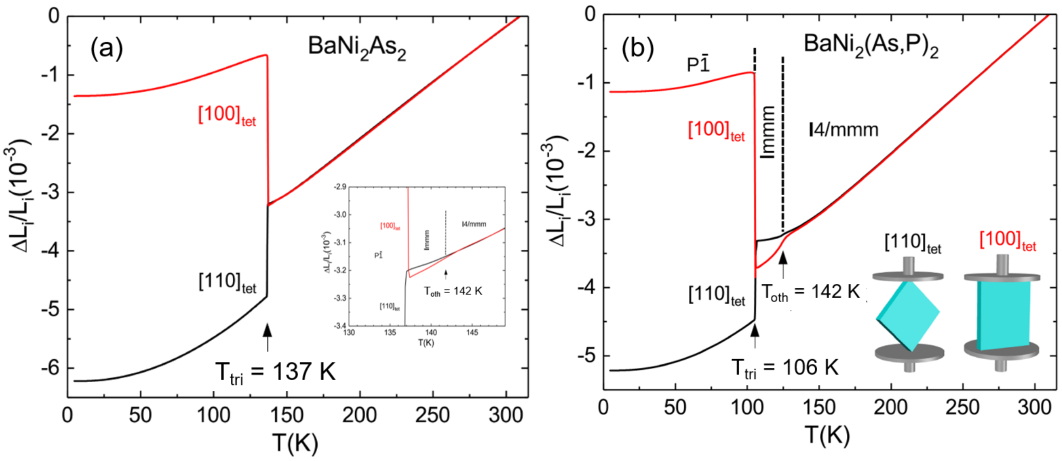

Figure 4.2.2: (a) Relative length change $\Delta L/L$ as a function of temperature of the $[100]_{tet}$ and $[110]_{tet}$ direction for $BaNi_2As_2$ measured by high-resolution capacitance dialtometry. The insert shows an enlarged section of the range above the first-order transition. (b) The same for $BaNi_2(As,P)_2$ with 3.5% phosphorus doping. The figures are taken from Ref. [64].

TE measurements were also used to determine the transition temperature for the first-order triclinic transition, which is marked by the dramatic jump in thermal expansion data of each direction with opposite signs as shown in Fig. 4.2.2.

The obtained triclinic transition temperatures T_{tri} for different doping levels are in good agreement with the previous report [63].

Four circle diffraction measurements

Four circle diffraction measurements were performed by Michaela Sofia Souliou and Tom Lacmann on single crystals $BaNi_2(As_{1-x}P_x)_2$ with $x = 0$ and 0.035 to detect the incommensurate charge density wave (IC-CDW) and commensurate charge density wave (C-CDW) [185]. A common Euler type diffractometer and a point detector were used in the experiment. The samples were glued with GE-varnish or Apiezon N on a Beryllium plate on a copper holder mounted on a heating stage and kept under vacuum in the DE-202SG/700K closed-cycle cryostat from ARS, which is surrounded by a Beryllium heat shield and Beryllium dome. Temperature-dependent measurements were enabled with a compressor, a heater, and a temperature controller. The incoming beam was generated from a Molybdenum X-ray tube with a voltage of 50 kV and a current of 40 mA. Both emitted X-rays at Molybdenum $K_{\alpha1}$ and $K_{\alpha2}$ lines with theoretical energies of 17479.10 ± 0.55 eV and 17374.18 ± 0.62 eV were used. The beam was collimated and cleaned up by a 0.8 mm pinhole before hitting the samples. To measure one Bragg peak, the sample was moved first by the angles ϕ and χ so the associated reciprocal vector lies in the equatorial plane in which the detector sits. The angles θ and 2θ were then oriented in conjunction to fulfill the Bragg relation. The top and side view of the experimental set-up is shown in Fig. 4.2.3.(a)-(b). Note that the θ and 2θ are not necessarily at a fixed ratio.

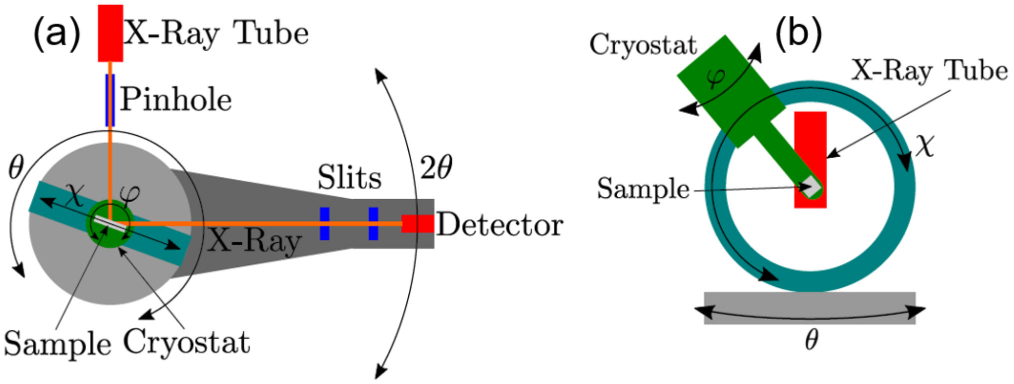

Figure 4.2.3: Schematic representations of the (a) top and (b) side view of the used four circle diffractometer with the mounted closed cycle cryostat. The four angular positions and correponding movemonts are also denoted. The figure is taken from Ref. [185].

In the end, IC-CDW with wave vector $(h, k{\pm}0.28, l)_{tet}$ and C-CDW with wave vector $(h,\ k \mp \frac{1}{3},\ l \pm \frac{1}{3})_{tet}$ were detected, in excellent agreement with the XRD data [64]. Moreover, the temperature dependence of the amplitude of each CDW, which is calculated by the integrated peak area squared, was carefully traced. The results are summarized in Fig. 4.2.4. We can thus extract the onset temperature T_{IC-CDW}, T_{CDW} for the IC-CDW and CDW order, respectively.

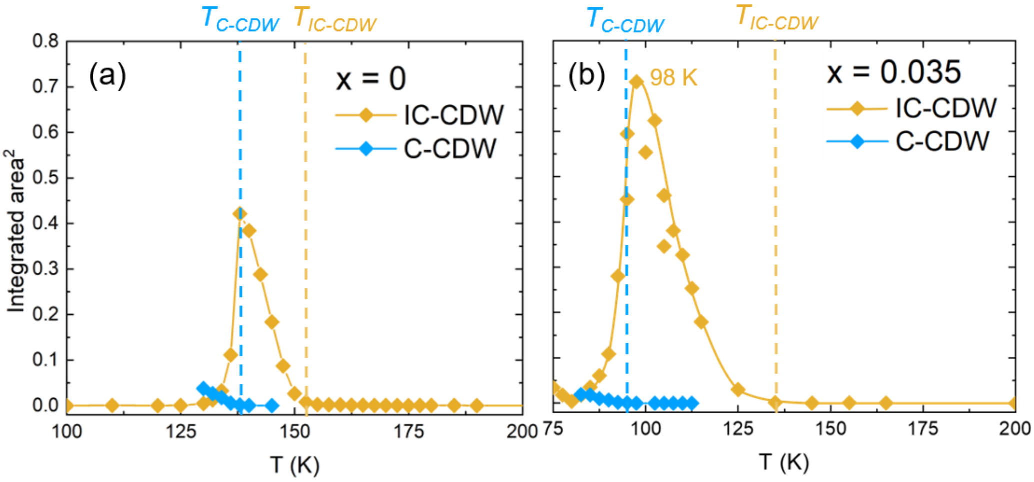

Figure 4.2.4: Temperature dependence of the amplitude of the IC-CDW and C-CDW in $BaNi_2(As_{1-x}P_x)_2$ with $x = 0$ and 0.035. The blue and yellow dashed lines mark the onset temperature of the two CDW orders respectively.

Finally, we summarize in Tab. 4.1 all transition temperatures determined during sample characterizations for materials with different phosphorus concentrations. The corresponding experimental method is marked in the end.

Table 4.1: Transition temperatures for $BaNi_2(As_{1-x}P_x)_2$ determined by different experimental methods.

Batch number	Phosphorus concentration	T_{oth} (K)	T_{tri} (K)	T_{IC-CDW} (K)	$T_{C-CDW}(K)$
TWCX1227	0	142.8	137.2	/	/
TWCX1375	~ 0.035	125.2	106.1	/	/
AAH43	0	/	/	155	138
AAH49	~ 0.035	/	/	135	95
AAH53	~ 0.045	/	87	/	/
AAH66	~ 0.065	110.3	69.3	/	/
Technique		Thermal expansion		Four circle diffraction	

4.2.3 Raman scattering

Raman scattering measurements were performed on single crystals $BaNi_2(As,P)_2$ in similar fashion as described in Sec. 3.2.3. All measurements were done with the low-resolution mode of the spectrometer with 600 grooves/mm for maximum signal output. In most of the measurements the He-Ne laser (633 nm) was used as the incident source with the exception when the main focus was on the low-frequency electronic background in searching for electronic nematicity, in which case the solid state green laser (532 nm) was used as the incident beam since the low-energy part of the spectrum is cleaner and the suppression of the eleastic line is better.

Prior to the experiment, Raman-active optical modes of $\mathrm{BaNi_2(As,P)_2}$ were determined following the *nuclear site group analysis*. Each unit cell contains one Ba-, one As- and one Ni-atom, resulting in 9 zone-center vibrational modes. In Tab. 4.2 we summarize the site symmetry of each point, the resulting normal modes, and the Raman-active optical modes within each phase. At room temperature, $\mathrm{BaNi_2(As,P)_2}$ possesses the tetragonal structure with space group $I4/mmm$ and point group D_{4h}, thus $1\mathrm{A}_{1g}$, $1\mathrm{B}_{1g}$ and $2\mathrm{E}_g$ modes are expected. Upon cooling, the system undergoes a second-order orthorhombic transition and the space group changes to I/mmm with point group D_{2h}. By breaking the four-fold symmetry, the A_{1g} and B_{1g} modes of the tetragonal phase become A_g modes in the orthorhombic phase, and the doubly degenerate E_g modes of the tetragonal phase split into non-degenerate B_{2g} and B_{3g} modes in the orthorhombic phase. However, the amplitude of the orthorhombic distortion is very small (in the order of 10^{-3} Å), as confirmed by the previous thermal expansion and XRD measurements, therefore, no drastic modifications in the phonon position or linewidth are expected. Finally below the first-order transition temperature, the symmetry of the structure is further lowered to triclinic with space group $P\bar{1}$ and point group C_i, where all phonon modes have A_g symmetry. The Raman tensor and polarization configuration for each Raman-active mode is shown in Tab. 4.3.

Theoretical estimations of the phonon energies in the high-temperature tetragonal phase and low-temperature triclinic phase were calculated using density functional theory introduced in Sec. 3.2.3. Due to the small amplitude of the orthorhombic distortion and the narrow temperature window of the orthorhombic phase, the phonon frequencies are expected to be close to those in the tetragonal phase. Calculations both with and without the internal structural parameters relaxed were performed. The resulted frequencies and eigenvectors of the Raman-active phonon modes are presented in Fig. 4.2.5.

Table 4.2: Atomic site symmetries and the resulting normal modes for each point and the Raman-active optical modes Γ_{Raman} for BaNi$_2$(As,P)$_2$ in different phases.

Tetragonal phase ($I4/mmm$)

Atom	Site symmetry	Irreducible representations
Ba	D_{4h}	$1\mathrm{A}_{2u} + 1\mathrm{E}_u$
As	C_{4v}	$1\mathrm{A}_{1g} + 1\mathrm{A}_{2u} + 1\mathrm{E}_u + 1\mathrm{E}_g$
Ni	D_{2d}	$1\mathrm{A}_{2u} + \mathrm{B}_{1g} + 1\mathrm{E}_u + 1\mathrm{E}_g$
Γ_{Raman}		$1\mathrm{A}_{1g} + 1\mathrm{B}_{1g} + 2\mathrm{E}_g$

Orthorhombic phase (I/mmm)

Atom	Site symmetry	Irreducible representations
Ba	D_{2h}	$1\mathrm{B}_{1u} + 1\mathrm{B}_{2u} + 1\mathrm{B}_{3u}$
As	C_{2v}	$1\mathrm{A}_g + 1\mathrm{B}_{1u} + 1\mathrm{B}_{2g} + 1\mathrm{B}_{2u} + 1\mathrm{B}_{3g} + 1\mathrm{B}_{3u}$
Ni	C_{2v}	$1\mathrm{A}_g + 1\mathrm{B}_{1u} + 1\mathrm{B}_{2g} + 1\mathrm{B}_{2u} + 1\mathrm{B}_{3g} + 1\mathrm{B}_{3u}$
Γ_{Raman}		$2\mathrm{A}_g + 2\mathrm{B}_{2g} + 2\mathrm{B}_{3g}$

Triclinic phase (P-1)

Atom	Site symmetry	Irreducible representations
Ba	C_1	$3\mathrm{A}_u$
As	C_1	$3\mathrm{A}_g + 3\mathrm{A}_u$
Ni	C_1	$3\mathrm{A}_g + 3\mathrm{A}_u$
Γ_{Raman}		$6\mathrm{A}_g$

Table 4.3: Raman tensor and polarization configuration of Raman-active modes of $BaNi_2(As,P)_2$

Irreducible representations	A_{1g}	B_{1g}	E_g
Raman tensor	$\begin{pmatrix} a & 0 & 0 \\ 0 & a & 0 \\ 0 & 0 & b \end{pmatrix}$	$\begin{pmatrix} c & 0 & 0 \\ 0 & c & 0 \\ 0 & 0 & 0 \end{pmatrix}$	$\begin{pmatrix} 0 & 0 & 0 \\ 0 & 0 & e \\ 0 & e & 0 \end{pmatrix}$
Polarization configuration	xx, yy, zz	xx, yy	yz, xz
Irreducible representations	A_g	B_{2g}	B_{3g}
Raman tensor	$\begin{pmatrix} a & 0 & 0 \\ 0 & b & 0 \\ 0 & 0 & c \end{pmatrix}$	$\begin{pmatrix} 0 & 0 & e \\ 0 & 0 & 0 \\ e & 0 & 0 \end{pmatrix}$	$\begin{pmatrix} 0 & 0 & 0 \\ 0 & 0 & f \\ 0 & f & 0 \end{pmatrix}$
Polarization configuration	xx, yy, zz	xz	yz

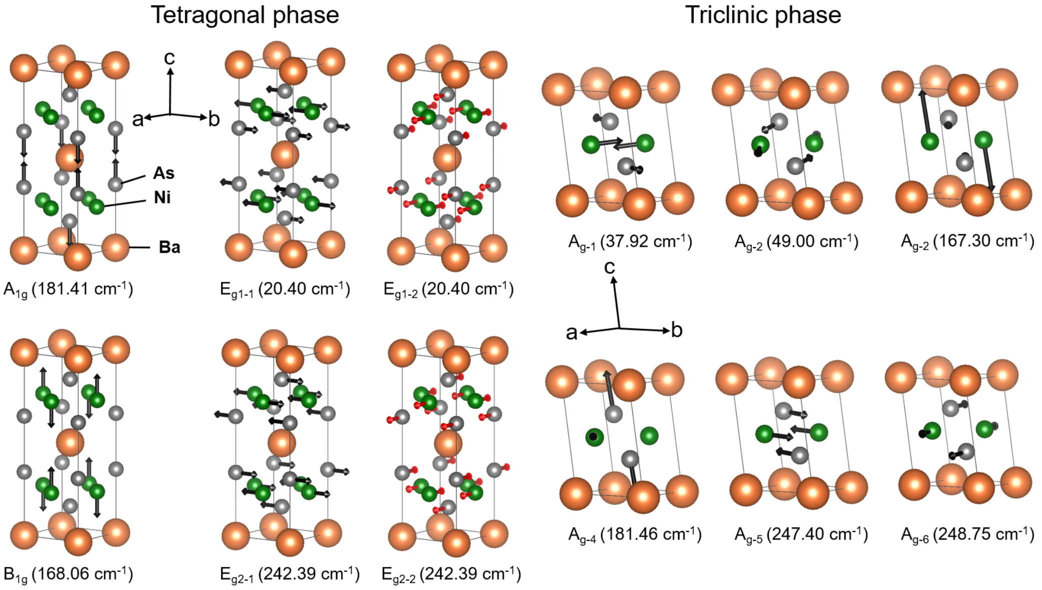

Figure 4.2.5: Schematic representations of the Raman-active modes of $BaNi_2As_2$ both in the high-temperature tetragonal phase and the low-temperature triclinic phase. Phonon eigenvectors are represented by black arrows (the red arrows show degenerate modes), and corresponding irreducible representations and phonon frequencies (with internal structural parameters relaxed) are written below the figure.

Temperature-dependent Raman scattering measurements in different configurations were performed on single crystals $BaNi_2(As_{1-x}P_x)_2$ with $x = 0$, 0.03, 0.035, 0.045, 0.06 and 0.065. Measurements with pure $BaNi_2As_2$ strained by a glass-fiber-reinforced plastic (GFRP) in the YZ configuration were also carried out. The results are summarized in Appendix. E. All crystal surfaces were freshly cleaved by a razor blade prior to the experiments. For the more delicate measurement in the ZZ and YZ configurations, the incident laser needs to be parallel to the crystal *ab*-plane, thus requiring the thin, layered-like sample to stand on its side. To this aim, we first glued the crystals on a 1 mm × 1mm × 2 mm high-quality copper piece as shown in Fig. 4.2.6.(a), with high-vacuum Apiezon N Grease which is craze-free at cryogenic temperatures and has very good thermal contact properties, then flipped this copper piece to let the samples hang on its side as shown in Fig. 4.2.6.(b), thus giving us an optical access to the edge of the crystal. The copper pieces were also glued on the cold finger with the same Apiezon N Grease to ensure good thermal contact.

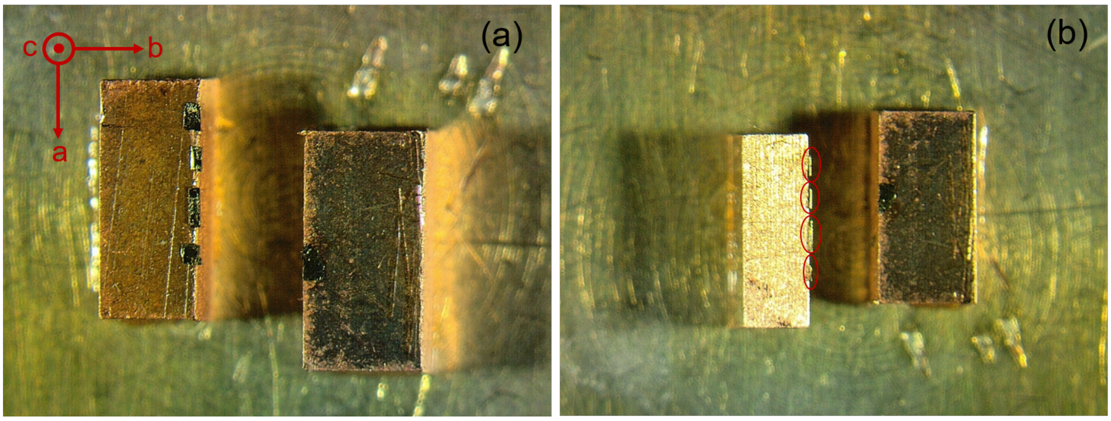

Figure 4.2.6: (a) First step: glue the crystals on a 1 mm × 1mm × 2 mm high-quality copper piece with high-vacuum Apiezon N Grease. (b) Second step: flip the copper piece so the samples are hanged on its side. The copper pieces were also glued on the cold finger with Apiezon N Grease to ensure thermal contact.

All four expected Raman-active modes were detected at room temperature for $BaNi_2(As_{1-x}P_x)_2$ with different doping levels. We show in Fig. 4.2.7.(a) the Raman response of pure $BaNi_2As_2$ at 310 K in the ZZ, YZ, XX and YX configurations. According to the polarization selection rules, we indexed the phonon mode in the ZZ configuration as A_{1g} (172.92 cm^{-1}), which is also active in the XX channel with frequency 171.16 cm^{-1}, and partially overlaps with the B_{1g} mode (158.65 cm^{-1}). The two modes in the YZ channel are the doubly degenerate E_g modes referred as E_{g1} (41.43 cm^{-1}) and E_{g2} (235.20 cm^{-1}). In Fig. 4.2.7.(b) we compare the measured and calculated phonon frequencies at 310 K. In general a good agreement is found for the A_{1g} and B_{1g} modes, whereas the calculations without relaxation of the internal structural parameters produce slightly better results for the E_g modes, especially the soft E_{g1}.

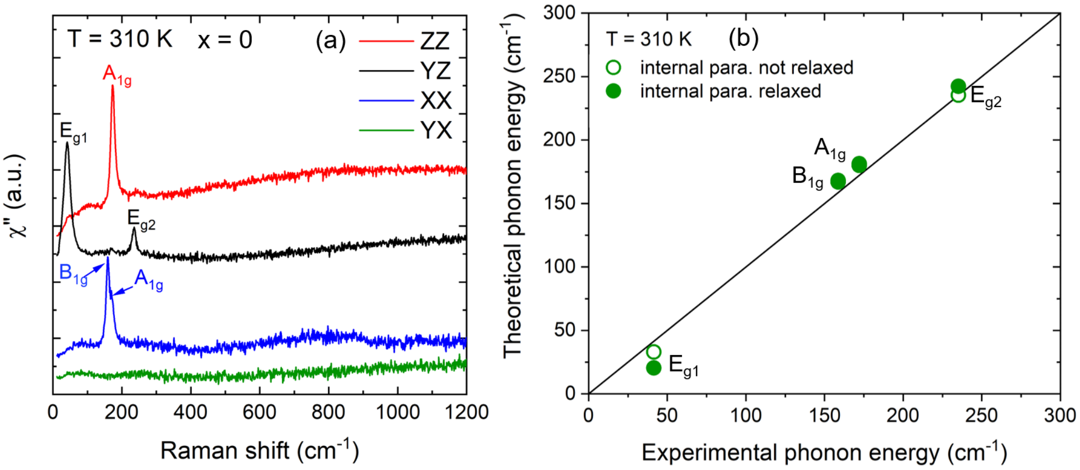

Figure 4.2.7: (a) Raman responses of pure $BaNi_2As_2$ at 310 K in the ZZ, YZ, XX and YX polarization configurations. All four Raman-active modes were detected and assigned according to the polarization selection rules. (b) Calculated phonon frequencies with (solid circle) and without (open circle) relaxation of the internal parameter are plotted versus the experimental phonon energies at 310 K. The solid line through the data has a slope of 1, meaning if the experimental and calculated phonon frequencies are equal, the data points will fall on the line.

The temperature and doping dependence of the lattice and electronic dynamics were carefully studied. Due to the strong first-order nature of the triclinic transition, the Raman spectra are dramatically renormalized across this transition. Therefore in the next parts we will present the experimental results divided into two parts, *i.e.*, above and below T_{tri}, with each part followed by in-depth discussions.

4.3 Lattice and electronic dynamics above the triclinic transition

4.3.1 Experimental results

Giant E_{g1} phonon splitting

In the YZ polarization configuration (here we do not distinguish YZ and XZ as in the tetragonal phase they are equivalent) we have observed extremely intriguing and anomalous behaviors of the two E_g phonon modes as functions of temperature and doping above the triclinic transition. First we restrict ourselves to the E_{g1} phonon behavior.

The evolution of the low-frequency part of the Raman response of pristine $BaNi_2As_2$ in this channel with temperature is given in Fig. 4.3.1.(a). The spectrum background has been subtracted for clarity. As we can see, the E_{g1} mode

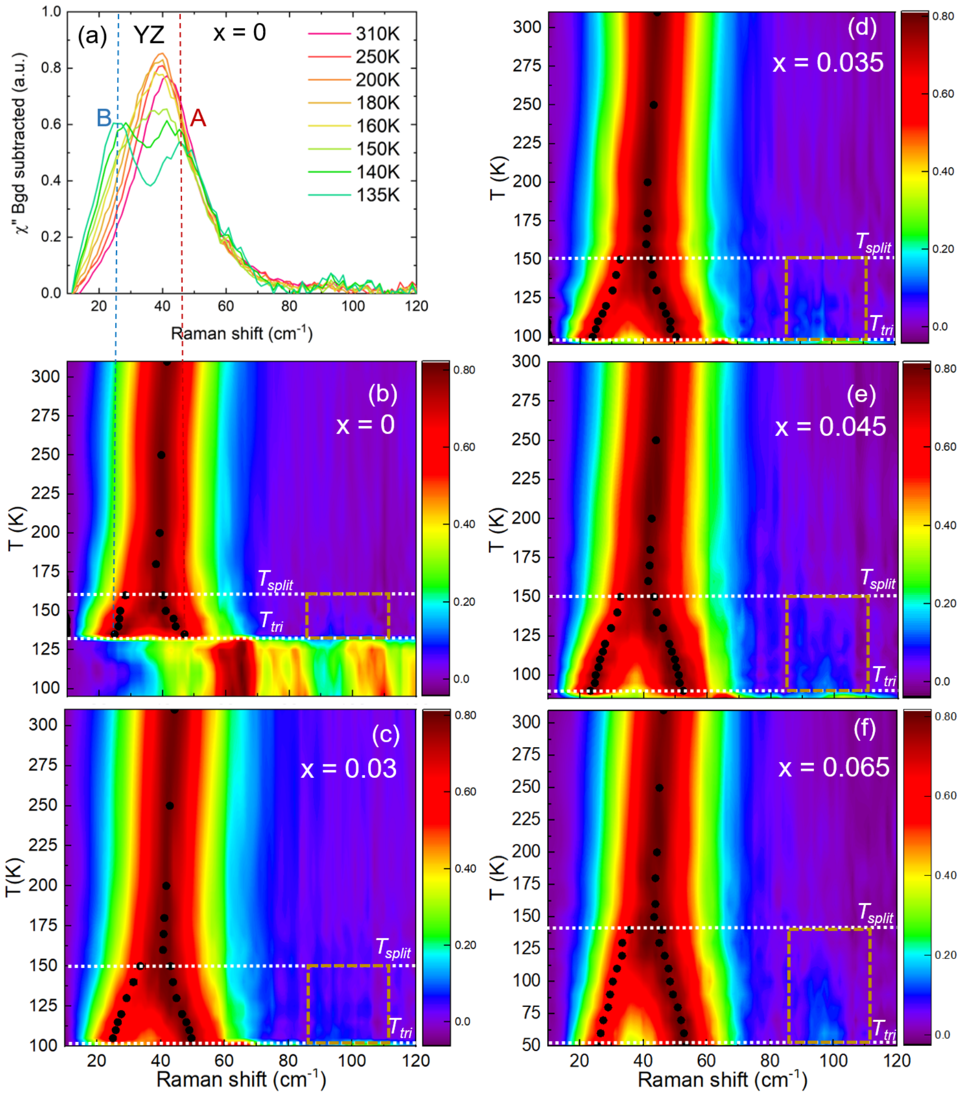

Figure 4.3.1: (a) Low-frequency part of the Raman responses of $BaNi_2As_2$ as a function of temperature. (b)-(f) Colormaps corresponding to the low-frequency part of the Raman response of $BaNi_2(As_{1-x}P_x)_2$ with $x = 0$, 0.03, 0.035, 0.045 and 0.065 at different temperatures, respectively. The black circles represent phonon frequencies obtained from fitting. The yellow dashed squares mark the area where several weak peaks were observed below T_{split} and above T_{tri}. The electronic background has been subtracted for clarity.

softens and broadens upon cooling until reaching 160 K, where a shoulder develops on the left side of the peak and the spectrum can no longer be described by one single phonon peak, signifying the occurrence of a splitting of the phonon mode. With one feature (referred as E_{g1}-A) keeps hardening and the other feature (E_{g1}-B) keeps softening, the splitting develops further until reaching the triclinic transition, where the strong first-order phase transition alters the spectrum completely and the E_g modes are replaced by multiple A_g modes. This phonon splitting and the abrupt renormalization of the spectrum across the triclinic transition can be clearly viewed in the corresponding colormap plotted in Fig. 4.3.1.(b). All spectra are scaled to have the same intensity for accurate demonstration of the phonon broadening effect. By phosphorus doping, the temperature dependence of the E_{g1} mode remains essentially the same as shown by Fig. 4.3.1.(c)-(f). While the triclinic transition temperature T_{tri} is strongly suppressed upon doping, the phonon splitting onset temperature T_{split} decreases only slightly, thus leaving us a much bigger temperature window to observe the splitting behavior. More importantly, regardless of the doping level T_{split} was found to be approximately 20 K higher than T_{oth} (see Tab. 4.1). This temperature difference could not result from different experimental set-ups based on the excellent agreement between the triclinic transition temperatures determined both by TE and Raman (maximum ∼ 5 K difference), thus giving an unambiguous evidence that the E_{g1} splitting occurs already in the high-temperature tetragonal phase.

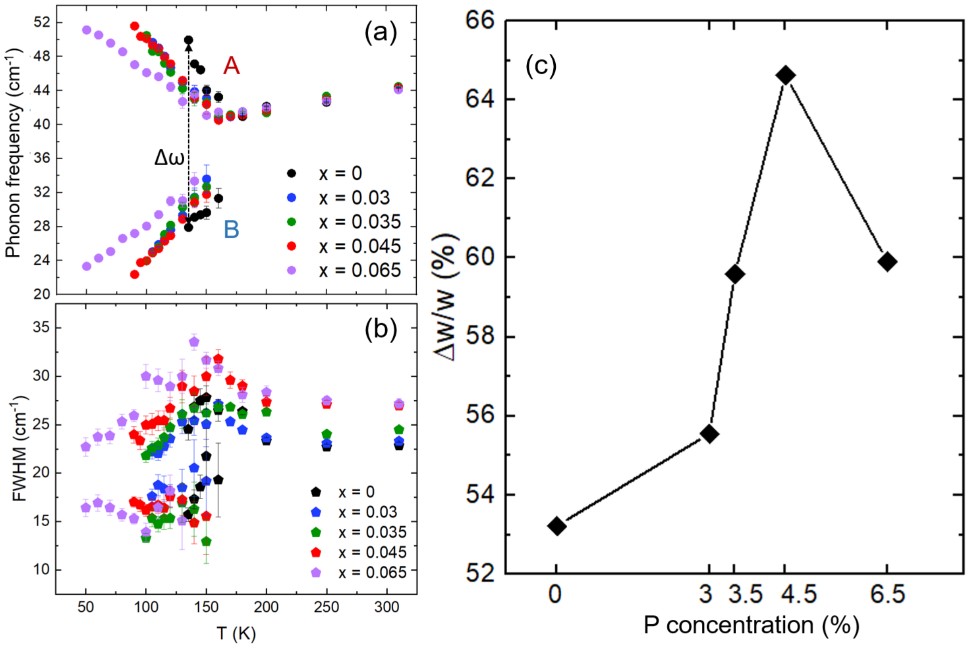

Figure 4.3.2: (a) E_{g1}-A and E_{g1}-B phonon frequencies and (b) phonon linewidths as functions of temperature and doping. (c) $\Delta w/w$ as a function of phosphorus concentration. w is the E_{g1} phonon frequency at 310 K, and Δw is the splitting amplitude just above the triclinic transition.

The temperature and doping dependence of the E_{g1} phonon frequency and linewidth are subsequently extracted by fitting the spectra with two DHOs (see Sec. 2.5). The results are summarized in Fig. 4.3.2.(a)-(b). As we can see, the splitting amplitude is extremely large, especially compared to the low frequency of the E_{g1} mode. In Fig. 4.3.2.(c) we calculated $\Delta w/w$ where w is the E_{g1} phonon frequency at 310 K, and Δw is the splitting amplitude just above the triclinic transition. Even for the pure $BaNi_2As_2$, the splitting is more than 50%, and this ratio pushes towards 65% for doped sample with $x = 0.045$. With higher doping level $x = 0.065$, $\Delta w/w$ is reduced back to $\sim 60\%$ due to a smaller splitting rate as shown in Fig. 4.3.2.(a).

E_{g2} phonon splitting

As for the E_{g2} mode, the phonon intensity is about 3-4 times lower than that of the E_{g1} mode, leading to a much lower signal-to-noise ratio. For the samples with medium phosphorus concentration ($x \leq 4.5$), no clear splitting of the mode was resolved, and all spectra can be fitted with one Voigt profile. The extracted phonon frequencies and phonon linewidths are summarized in Fig. 4.3.3.(a)-(b). For the pure $BaNi_2As_2$, the E_{g2} mode hardens almost linearly upon cooling, with the linewidth showing little temperature dependence. With phosphorus doping, the phonon hardens initially upon cooling, then a kink develops below 200 K, as the phonon seems to soften slightly until $\sim$ 150 K, then resumes to harden as before until reaching the triclinic transition temperature. On the other hand, the linewidths narrow at first from 310 K to $\sim$ 150 K, then increase dramatically with further cooling with no clear evidence of phonon splitting.

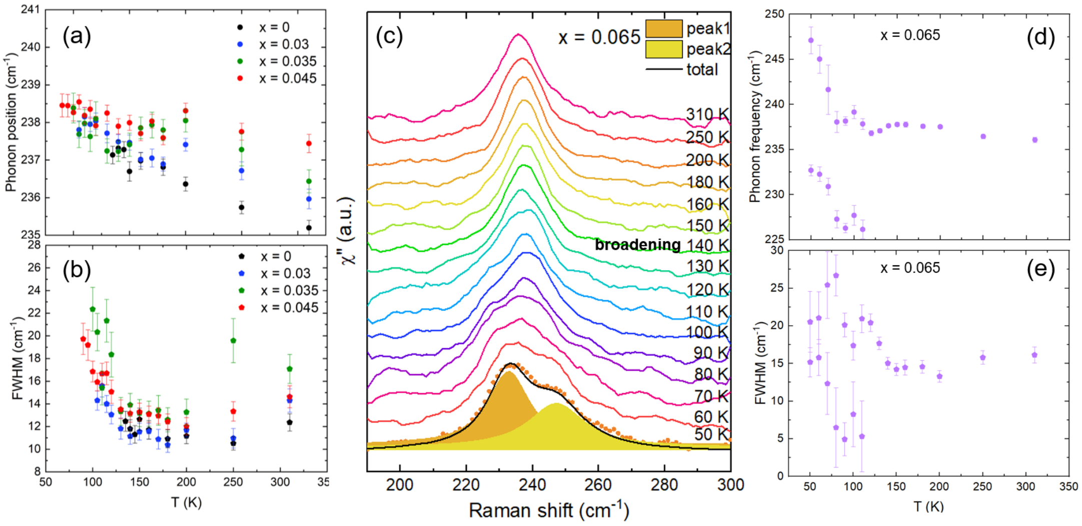

Figure 4.3.3: E_{g2} phonon frequencies (a) and phonon linewidths (b) as functions of temperature and doping. (c) The smoothed spectra of doped $BaNi_2As_2$ with $x = 0.065$. All spectra are shifted vertically for clarity. The temperature where the phonon starts to broaden is marked in the figure. The temperature dependence of the phonon frequency and linewidth of this material is summarized in (d) and (e), respectively.

However, in the sample with a higher P-concentration ($x = 0.065$), a sizable splitting ($\sim$ 20 cm^{-1}) of the E_{g2} mode was detected upon cooling approaching the triclinic transition temperature. The corresponding Raman response between 190 cm^{-1} to 300 cm^{-1} are plotted in Fig. 4.3.3.(c). All spectra are smoothed and shifted vertically for clarity. As we can see, the E_{g2} mode initially hardens and narrows down upon cooling from 310 K to 150 K. At 140 K, the hardening stops and the phonon clearly broadens. The broadening continues with further cooling until two peaks can be distinctly observed at 110 K. Below 110 K, two Voigt functions are needed to fit the spectra. The representative fitting curves at 50 K are shown in the figure and the obtained fitting results are summarized in Fig. 4.3.3.(d)-(e).

Additional modes in the YZ configuration

Besides the anomalous phonon behavior of the E_g modes, we have also observed the emergence of several additional modes below T_{split} in the low-frequency part (between 85 cm^{-1} to 110 cm^{-1}) of the Raman response of all investigated samples. In the colormaps in Fig. 4.3.1.(b)-(f), this region is marked by a yellow dashed square. As we can see, the intensities of these peaks increase with further cooling until again reaching the triclinic transition temperature, at which point they are replaced by much stronger A_g modes.

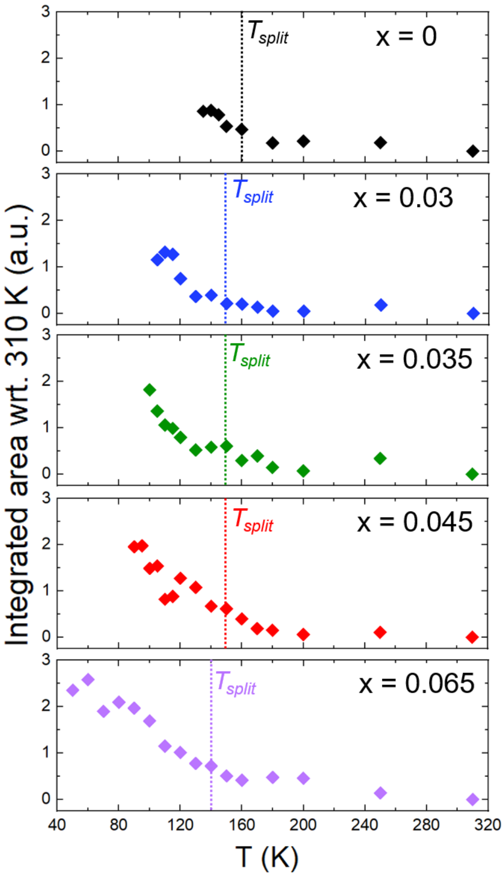

Figure 4.3.4: The evolution of the integrated area of Raman spectra within the range of 85 cm^{-1}-110 cm^{-1} with temperature after subtracting the integration performed at 310 K for $BaNi_2(As_{1-x}P_x)_2$ with x = 0, 0.03, 0.035, 0.045 and 0.065. The onset temperature of the E_{g1} splitting of each sample is marked by the dashed line.

The spectral weight within this range is subsequently integrated. We obtained the temperature-dependent part of the Raman response by subtracting the integration by that at 310 K, and summarized the results in Fig. 4.3.4. As we can see, the temperature dependencies of the spectral weight are similar between different doping levels, and the integration appears higher for heavier doping only because of the delayed entrance to the triclinic phase. As these peaks appear well above T_{oth}, it is unlikely these additional modes are results of backfolding of the phonon dispersion curves. The origin of this observation thus remains an open question.

Electronic nematic fluctuations with B_{1g} symmetry

Detailed temperature-dependent Raman scattering measurements on doped $BaNi_2As_2$ single crystals with $x = 0.065$ in the B_{1g} (X′Y′, 45° rotated with respect to XY) and B_{2g} (XY) polarization configurations were performed to probe possible response of electronic nematic fluctuations. Sample with the highest doping concentration was chosen as the triclinic transition is suppressed the most in this material, leaving us the widest window for temperature-dependent measurements. The green laser with wavelength of 532 nm was used as the incident source as mentioned in Sec. 4.2.3.

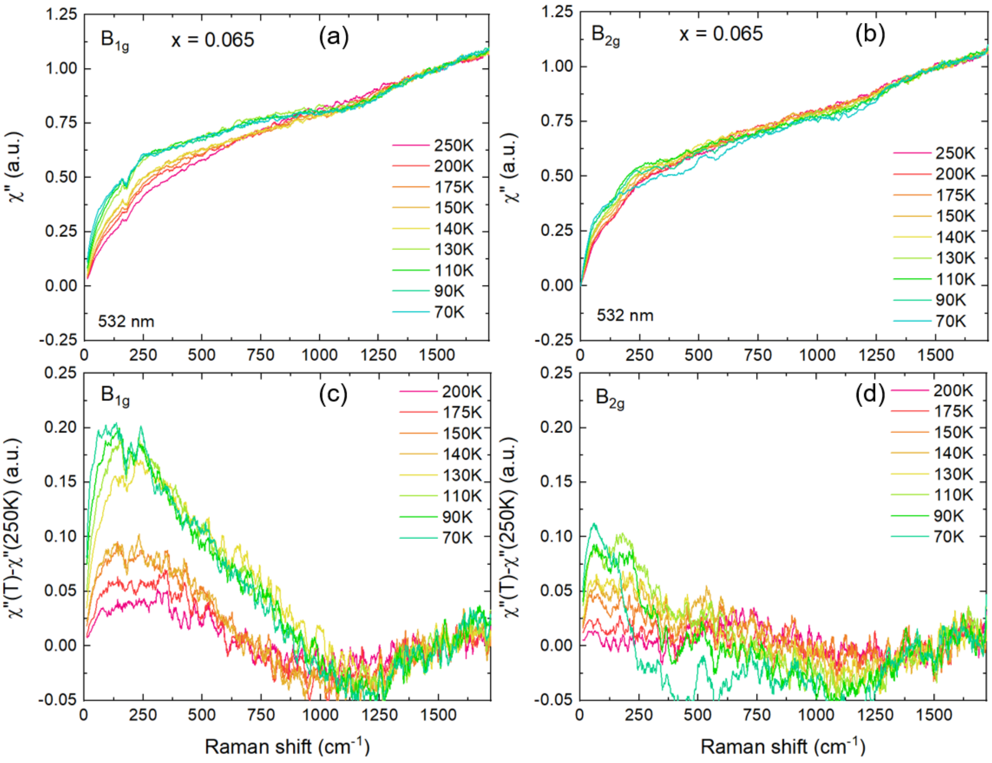

Figure 4.3.5: (a) Raman response of $BaNi_2(As_{1-x}P_x)_2$ with $x = 0.065$ at different temperatures in the B_{1g} channel. (b) The same in the B_{2g} configuration. (c) Temperature-dependent part of the Raman response $\chi''(T) - \chi''(250K)$ in the B_{1g} channel. (d) The same in the B_{2g} configuration.

The electronic part of the obtained Raman response (after the B_{1g} phonon is fitted and subtracted) in both configurations is plotted in Fig. 4.3.5.(a)-(b). As we can see, the Raman response in B_{1g} channel shows a clear buildup of intensity below 1000 cm^{-1} upon approaching T_{tri}, while in the B_{2g} channel the spectra are relatively quiet with no obvious changes with temperature. For more direct comparison, we extracted the temperature-dependent part of the Raman response $\chi''(T) - \chi''(250K)$ and plotted them in Fig. 4.3.5.(c)-(d). As we can see, there is a broad peak developing in the B_{1g} channel upon cooling, and no such phenomenon was observed in the B_{2g} channel. The temperature and distinctive symmetry dependencies of this broad peak remind us of the low-frequency quasi-elastic peak (QEP) observed in the B_{2g} channel in the Fe-based superconductors [48, 114], and could be linked to the dynamic electronic nematic fluctuations corresponding to an orientational order along the Ni-As bonds.

Standard behavior of the B_{1g} phonon mode

Regardless of the electronic dynamics in the B_{1g} channel, the B_{1g} phonon shows standard behavior in all investigated samples ($x = 0$, 0.035, 0.045, 0.065).

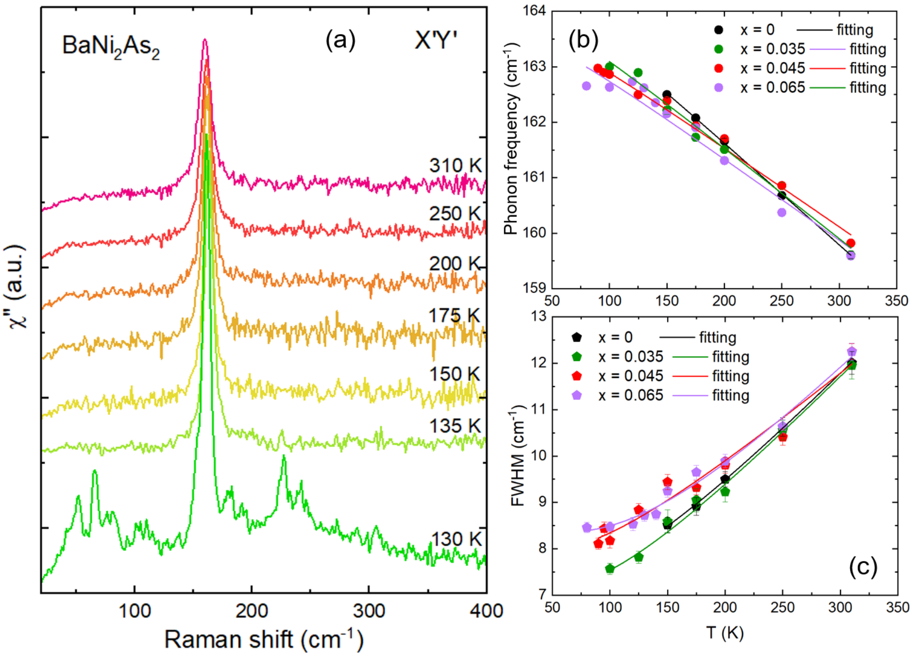

Figure 4.3.6: (a) Raman responses of pure $BaNi_2As_2$ in the X′Y′ polarization configuration as a function of temperature. Spectra are shifted vertically for clarity. (b) Temperature and doping dependencies of the B_{1g} phonon frequency. The solid lines are fitting results from the anharmonic model. (c) Temperature and doping dependencies of the B_{1g} FWHM, with fitting results based on the anharmonic model.

Representative spectra of pure $BaNi_2As_2$ ($T_{tri} \sim 130$ K-135 K) in the X′Y′ polarization configuration as a function of temperature are shown in Fig. 4.3.6.(a).

The spectra are shifted vertically for clarity. As we can see, a single sharp and strong peak corresponding to the B_{1g} phonon mode was observed at room temperature, and it hardens and sharpens upon cooling until reaching the triclinic transition temperature, at which point the B_{1g} mode is replaced by multiple A_g modes. The spectra were fitted with the Voigt profile, and the temperature and doping dependence of the phonon frequency and phonon linewidth are shown in Fig. 4.3.6.(b)-(c).

The extracted B_{1g} phonon energies and FWHM for each sample can be well described by the anharmonic model as represented by the solid lines in the figure. Phosphorus doping seems to have little influence on the phonon frequency, which can be well understood since the B_{1g} phonon represents vibrations of the Ni atoms, and should show little subjection to the phosphorus substitution on the As-site. As for the phonon linewidth, the FWHMs at lower temperatures are slightly larger for heavily doped ($x > 0.035$) samples than that of pure or lightly doped samples. Since the FWHM is inversely proportional to the lifetime of the phonon, a larger FWHM indicates a shorter lifetime, which can be well accounted for by the induced disorder by doping.

Strong doping dependence of the A_{1g} phonon mode

The behavior of the A_{1g} phonon in the ZZ configuration was carefully studied on single crystals $BaNi_2(As_{1-x}P_x)_2$ with $x = 0$, 0.03 and 0.045. For all investigated systems, a single sharp and strong peak corresponding to the A_{1g} symmetry was observed at room temperature. Upon cooling, the phonon sharpens and shifts to a higher frequency. With further cooling, the system enters the triclinic phase and the spectrum is strongly remodified with the A_{1g} mode replaced by multiple A_g phonons. Representative spectra of pure $BaNi_2As_2$ showing this temperature dependence are plotted in Fig. 4.3.7.

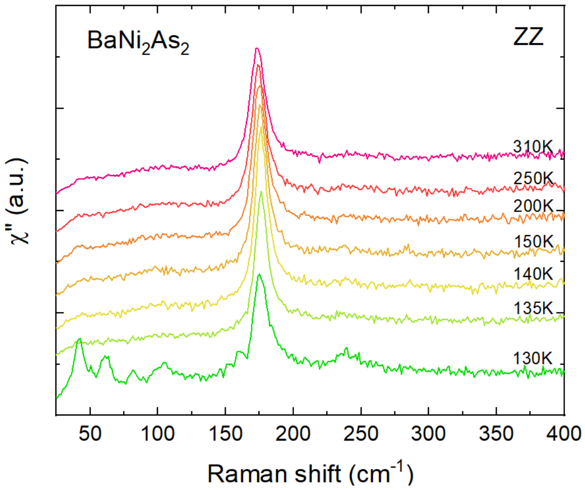

Figure 4.3.7: Representative spectra of pure $BaNi_2As_2$ in the ZZ configuration from 310 K to 130 K. Single A_{1g} mode was detected at high temperatures. Below 135 K, multiple phonon modes were observed in the triclinic phase.

Weak Fano lineshape of the A_{1g} mode is already observed in the parent compound. With doping the phonon becomes significantly more asymmetric and broadened, as can be seen from the comparison between the spectra with different doping levels at 310 K in Fig. 4.3.8.(a). Note that all spectra are scaled and shifted for clarity. To gain more insight into the temperature and doping dependence of the phonon behavior, we fitted the spectra with the Fano profile (Eq. 2.32) and extracted the phonon frequencies, phonon linewidths, and asymmetric parameters (The lineshape asymmetry is represented by $1/q^2$, and the smaller the q is, the more asymmetric the lineshape is). They are summarized and plotted in Fig. 4.3.8.(b)-(d). We can clearly see that for doped samples the asymmetries are $3 \sim 4$ times enhanced, indicating a stronger interaction between the phonon and electronic continuum, which could result from either larger electron-phonon coupling (EPC) strength or higher electronic density of states (DOS) at the Fermi level. The doping dependence of the phonon linewidth is in line with this picture. As previously introduced in Sec. 2.2.4, the phonon linewidth is proportional both to the electronic DOS and the EPC strength squared. And from our data, the linewidth at 310 K increases from 13 cm^{-1} to 16.5 cm^{-1} between $x = 0$ and 0.045.

As for the phonon frequency, a clear hardening with doping was observed. On one hand, based on the structural parameters extracted from previous XRD measurements, the crystallographic c-axis increases from 11.6424 Å to 11.6468 Å between $x = 0$ and $x = 0.035$, which would lead to a softening of ~ 0.4 cm^{-1} based on a simple approach linking the phonon frequency w with the bond length l ($w^2 \sim \frac{1}{l^3}$) [178, 186]. Thus the softening induced by the lattice distortion is very small. On the other hand, the phosphorus atom is much lighter than the arsenic atom (the atomic weight is 30.97 for P and 74.92 for As), and as the phonon frequency is $\propto \sqrt{1/m}$, higher vibrational energy can be expected.

Now, regardless of the doping effect, we find that the temperature dependence of the phonon frequency and linewidth is similar for all investigated systems. While the changes of phonon linewidths can be well fitted by the anharmonic model, as represented by the solid lines in Fig. 4.3.8.(d), the temperature dependence of the phonon frequencies shows clear deviation from the standard behavior. The A_{1g} mode initially hardens linearly upon cooling from 310 K, the variation rate slows down below $\sim$ 180 K and the phonon frequency seems to reach a plateau above 150 K. When further cooled below 150 K, a small jump in the phonon position was observed for all investigated systems, and after a small temperature window ($\sim$ 10 K), the phonon presumes to harden with initial variation rate.

4.3.2 Discussions

Unique features of the E_g phonon splitting in the Ni-based compounds

As already mentioned in Sec. 4.1, anomalous E_{g1} phonon splitting has been previously observed in $\text{Ba}(\text{Fe}_{1-x}\text{Co}_x)_2\text{As}_2$ [178], and such phenomenon could arise from the coupling between the phonon mode with the electronic nematic order. However, the splitting was detected below the orthorhombic transition, indicating a finite contribution of lattice distortion. In addition, the presence of magnetism

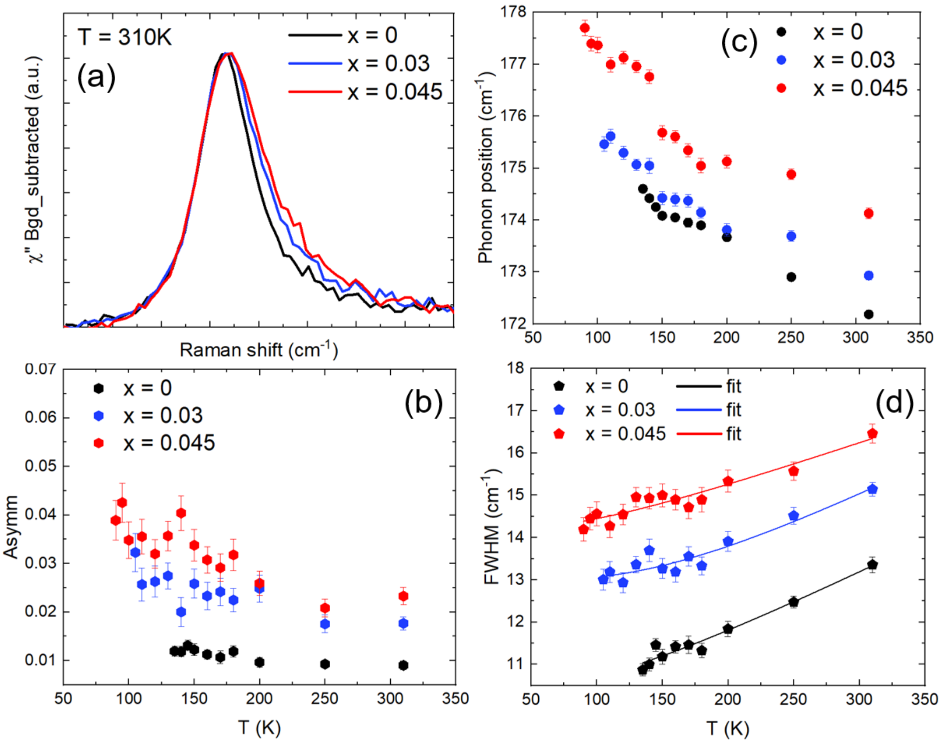

Figure 4.3.8: (a) Direct visualization of the doping dependence of the A_{1g} mode at 310 K. The spectra are shifted and scaled for comparison. The peak is clearly broadened and more asymmetric upon doping. (b) Asymmetric parameters extracted from the fitting results as functions of temperature and doping. (c) Temperature and doping dependencies of the A_{1g} phonon frequencies. (d) Temperature and doping dependencies of the A_{1g} phonon linewidth (FWHM). The solid lines are the fitting results based on the anharmonic model.

might suggest an alternative explanation based on a strong spin-phonon coupling effect, thus casting doubts on the role of electronic nematicity. The situation is much more clarified in the case of Ni-based compounds. To begin with,the E_{g1} phonon splitting was observed above T_{oth} in the high-temperature tetragonal phase. Secondly, no magnetism is present in this system. And finally, as already shown in Fig. 4.3.2, the splitting of nearly 30 cm^{-1} cannot be accounted for by the orthorhombic distortion on the scale of 10^{-3} Å. Therefore, the strong coupling between the doubly degenerate E_g mode with the charge/orbital nematic fluctuations appears to be the only possible origin for the observed phonon splitting.

We should also point out several differences in the temperature and doping dependencies of the splitting amplitude in the Fe- and Ni-based systems (Fig. 4.3.9). In the Fe-based compounds, the splitting amplitude follows the temperature dependence described by $\Delta w(T) = \Delta w(T = 0K) \times (1 - \frac{T}{T_{oth}})^{\beta}$ with β being the critical exponent ranging from 0.1 to 0.2 (represented by dashed lines in Fig. 4.3.9.(a)), and seems to reach saturation at the lowest temperatures. In $BaNi_2(As_{1-x}P_x)_2$, however, linear temperature dependence was observed with no sign of saturation.

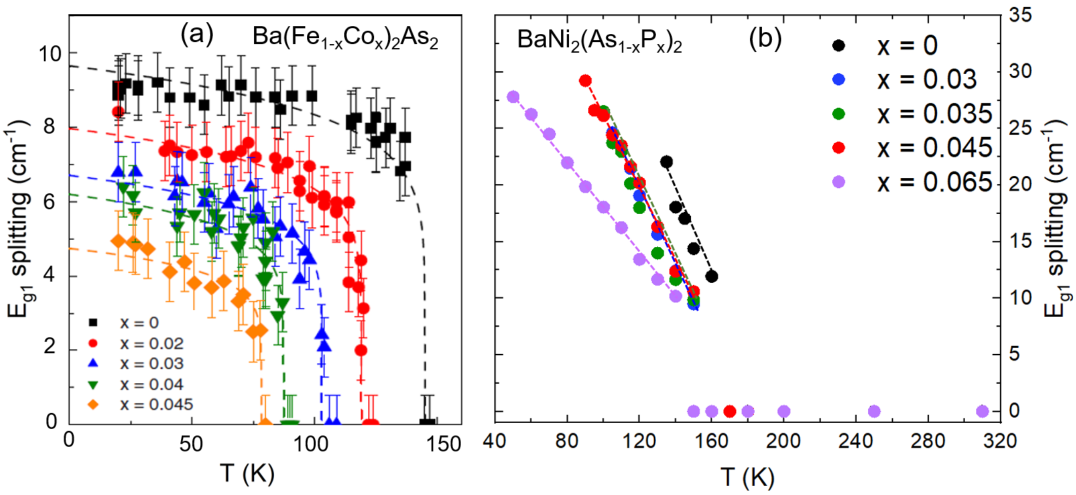

Figure 4.3.9: Temperature and doping dependencies of the E_{g1} splitting amplitude for (a) $Ba(Fe_{1-x}Co_x)_2As_2$ and (b) $BaNi_2(As_{1-x}P_x)_2$. The dashed lines in (a) are fitting results as described in the text. The dashed lines in (b) are to guide the eye.

On the other hand, cobalt doping in $BaFe_2As_2$ strongly suppresses T_{split}, from $\sim$ 137 K to 75 K between $x = 0$ to $x = 0.045$, while leaving the general temperature dependence unaltered. Such strong doping dependence of T_{split} was not detected in the P-doped $BaNi_2As_2$, as T_{split} only decreases from 160 K to 140 K between $x = 0$ to $x = 0.065$. Interestingly, P-doping appears to slow down the temperature dependence of the splitting amplitude, as indicated by the slops of the dashed lines in Fig. 4.3.9.(b).

Origin of the IC-CDW and orthorhombic transition

In Fig. 4.3.10.(a)-(d) we have plotted the temperature dependence of the E_g splitting amplitude for $BaNi_2(As_{1-x}P_x)_2$ with $x = 0$ and 0.035 in comparison with the amplitude of the two charge density waves as a function of temperature in corresponding samples. The amplitude of the CDWs is calculated by the integrated peak area squared. The triclinic and orthorhombic transition temperatures are marked by black and purple dashed lines, respectively. As we can see, in pure $BaNi_2As_2$, the E_g splitting precedes the emergence of IC-CDW, which occurs at a higher temperature than T_{oth}. The amplitude of IC-CDW grows further with cooling, and reaches a maximum at T_{tri}. Upon further cooling, the intensity of IC-CDW drops dramatically, while that of the C-CDW clearly starts to build up. This relationship remains largely the same in the doped system, except that the IC-CDW grows over a wider temperature window, and at T_{tri} its magnitude is considerably larger.

The IC-CDW has a unidirectional nature, which agrees with that of the Ising nematic order pointing along either a or b directions. Moreover, the magnitude of IC-CDW increases continuously until reaching T_{tri} in a similar manner as the E_g

splitting amplitude. We thus strongly suspect that the electronic nematicity also plays a significant role in the formation of this charge density wave. The reason why the IC-CDW propagates with an incommensurate wave vector is, however, not yet clear.

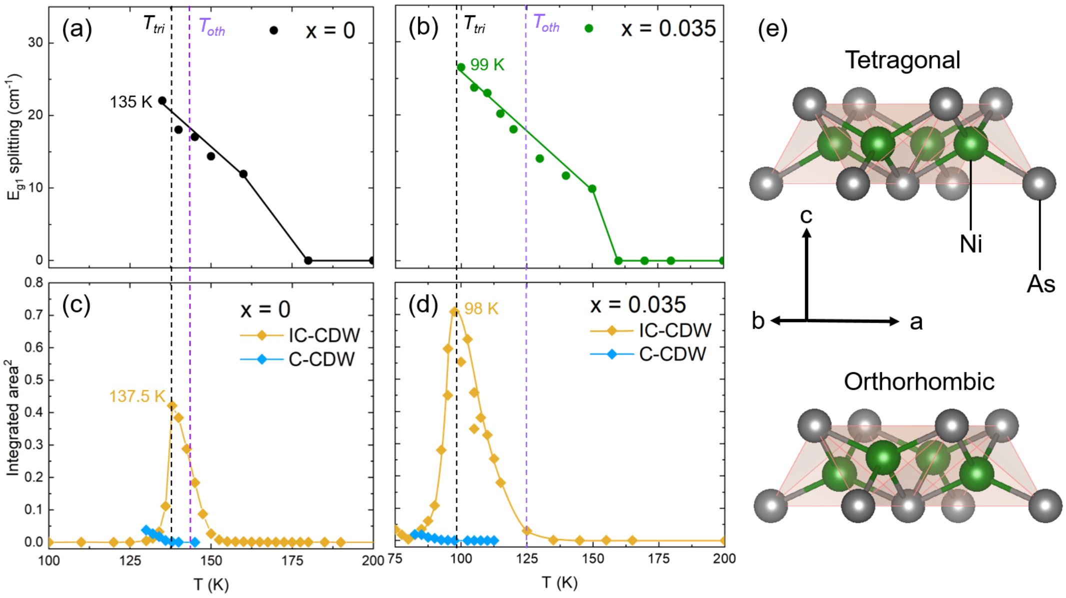

Figure 4.3.10: (a) (b) E_{g1} splitting amplitude as a function of temperature of $BaNi_2(As_{1-x}P_x)_2$ with $x = 0$ and 0.035. (c) (d) Temperature dependence of the amplitude of the two charge density waves in corresponding systems. T_{tri} and T_{oth} are marked by black and purple dashed lines, respectively. (e) Schematic representations of the NiAs tetrahedron in the same plane in the tetragonal and orthorhombic phase. The amplitude of the orthorhombic distortion is exaggerated for clarity.

As for the second-order orthorhombic transition, we remind ourselves first of some of its properties. First of all, the amplitude of the orthorhombic distortion which is usually marked by the difference between the lattice parameter a and b is negligibly small and does not increase upon doping (from the supplementary information of Ref. [64], for pure $BaNi_2As_2$, $|a-b|/a$ at 140 K is only 0.099%, and 0.058% at 110 K for the doped sample with $x = 0.035$). Such a small amplitude of distortion clearly suggests an electronic origin of the structural transition. Secondly, the effect of the orthorhombic distortion is more focused on shifting the positions of Ni and As atom along the crystallographic c-axis. As shown in Fig. 4.3.10.(e), in the tetragonal phase, all Ni atoms sit on the coordinates (1/2, 0, 1/4), and all Ni-As bond lengths within the tetrahedron are the same. Upon entering the orthorhombic phase, the Ni atoms leave the 1/4 position along c-axis, resulting in different Ni-As bond-lengths along a and b directions. This difference is only 0.085% for pure $BaNi_2As_2$, but increases to 0.98% for doped material with $x = 0.035$, in agreement with the larger orthorhombicity observed along $[100]_{tet}$

direction in thermal expansion measurements. The physical meaning of the different Ni-As bond lengths is clear: the d_{xz} and d_{yz} orbitals of the Ni atom are no longer degenerate. From the XRD measurements, we found that the bond lengths along a-axis is generally shorter than that along b-axis, thus indicating a favored occupation of the d_{xz} orbital in the orthorhombic phase. These above mentioned observations thus strongly suggest that this second-order structural transition is driven by the electronic nematic order.

Electronic nematic transition temperature

After obtaining the Raman response of the electronic nematic fluctuations in the B_{1g} channel (Fig. 4.3.5), we attempted to extract the corresponding nematic transition temperature T_{nem}. We started by calculating the static nematic susceptibility $\chi_0^{x^2-y^2}$ using the Kramers-Kronig relation:

$$\chi_0^{x^2-y^2} = \frac{2}{\pi}\int_0^{\infty} dw(\chi'')^{x^2-y^2}(w)/w. \tag{4.1}$$

The static nematic susceptibility is then governed by the Raman conductivity χ''/w, especially by the low-frequency part of χ''. The temperature dependence of the Raman conductivity is plotted in Fig. 4.3.11.(a), which shows that the broad peak is now centered at zero frequency.

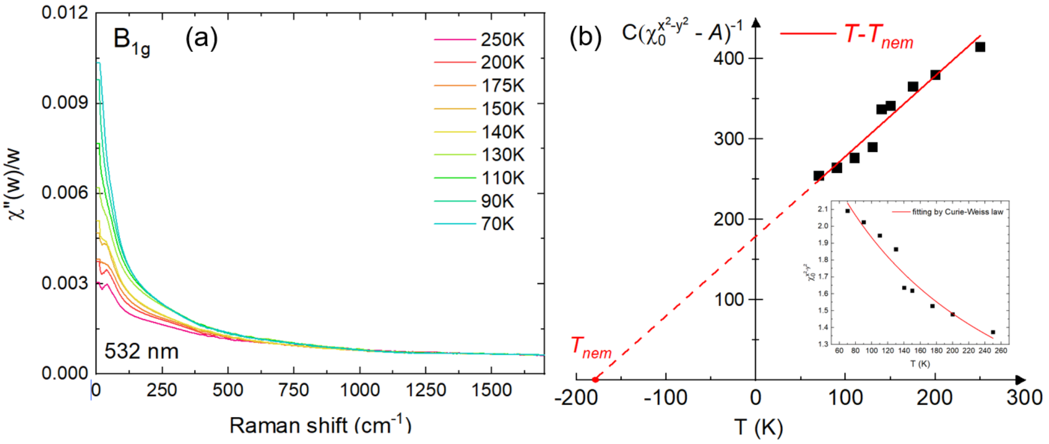

Figure 4.3.11: (a) Raman conductivity $\chi''(w)/w$ of $BaNi_2(As_{1-x}P_x)_2$ with x = 0.065 in the B_{1g} channel as a function of temperature. (b) $C(\chi_0^{x^2-y^2} - A)^{-1}$ as a linear function of T. The red line represents $T - T_{nem}$. The value of T_{nem} can be read from the intercept with the x-axis. In the inset the extracted static electronic nematic susceptibilities $\chi_0^{x^2-y^2}$ for different temperatures are plotted. The red line is the fitting result by the Curie-Weiss law.

Using Eq. 4.1 we performed a partial integration of χ''/w up to 1000 cm^{-1} to extract the static nematic susceptibility $\chi_0^{x^2-y^2}$. The cut-off of 1000 cm^{-1} was chosen since above this value the spectra appear to be temperature independent.

Before the integration the Raman spectra were extrapolated linearly from the lowest frequency experimentally accessible (10 cm^{-1}) to zero. The resulted $\chi_0^{x^2-y^2}$ as shown by the inset in Fig. 4.3.11.(b) increases continuously upon cooling, without any diverging behavior near T_{split} (140 K) or T_{oth} (110 K), until the triclinic transition sets in. Nevertheless, we fitted the points with the Curie-Weiss law of the form

$$(\chi_0^{x^2-y^2})^{-1}(T) = (A + \frac{C}{T - T_{nem}})^{-1}, \tag{4.2}$$

where A and C are constants and T_{nem} represents the electronic nematic transition temperature. In the end, we obtained T_{nem} = -178.65 K ± 29.50 K. The reverse susceptibility $C(\chi_0^{x^2-y^2} - A)^{-1}$ as a linear function of T is plotted in Fig. 4.3.11.(b), with the red line representing $T - T_{nem}$. T_{nem} is then marked as the intercept with the x-axis. This negative value surely appears to be rather odd, however, as already mentioned in Sec. 2.4, the extracted T_{nem} is systematically much lower than the actual thermodynamic structural transition temperature since any contribution of the lattice to the susceptibility is excluded. Such a large difference between T_{nem} and T_{oth} in return suggests a strong electron-phonon coupling effect in the Ni-based system. This also agrees with the overdamped profile of the quasi-elastic peak in the B_{1g} channel, as the large linewidth distinctively indicates stark interplay between the electronic and lattice degrees of freedom.

Theoretical model for the coupling between the E_g phonon and electronic nematic fluctuations

In order to reproduce the experimentally observed phonon splitting behavior, we adopted a preliminary theoretical model for the coupling between an Ising nematic degree of freedom to the doubly degenerate phonon with E_g symmetry at the Γ-point [187]. The E_g phonon is represented by a simple harmonic oscillator

$$H_{E_g} = \frac{p_x^2}{2M} + \frac{p_y^2}{2M} + \frac{M w_0^2}{2}(u_x^2 + u_y^2), \tag{4.3}$$

which reflects the degeneracy of the modes. p_i $(i = x, y)$ are the phonon momenta while u_i represent the ionic displacements, and w_0 gives the phonon frequency. Next we couple these modes to an Ising variable $\sigma \in \{|+\rangle = (1,0), |-\rangle = (0,1)\}$ that describes the nematic degree of freedom of the B_{1g} mode

$$H_{nem} = \lambda^2 \tau_z u_x u_y + \frac{\Omega}{2}\tau_x. \tag{4.4}$$

Here λ^2 is the coupling strength of the Ising nematic degree to the two phonons and the Pauli matrices τ_α act in the space of the pseudospin σ. We included the symmetry-allowed coupling for a nematic degree that transforms according to the B_{1g} symmetry. Ω is the rate at which the nematic state undergoes quantum fluctuations. When the Ising order parameter $\langle\tau_z\rangle$ is finite, the E_g modes would be split in $\sqrt{w_0^2 \pm \langle\tau_z\rangle\lambda^2}$, namely, the splitting is proportional to the order parameter for small $\frac{\lambda^2}{w_0^2}\langle\tau_z\rangle$. However, because of these quantum transitions the Ising nematic variable never condenses at finite Ω, *i.e.*, $\langle\tau_z\rangle = 0$. While non-local interactions of the Ising variable can induce a finite transition, here we focus on the above local problem without breaking any symmetry.

In order to analyze the coupled problem, we first added the two Hamiltonians from Eq. 4.3 and Eq. 4.4 together and evaluate the matrix elements of the obtained Hamiltonian in the harmonic oscillator basis. So far we have limited ourselves to the zero-temperature case and under the assumption that the B_{1g} nematic mode is a delta-peak. In the end, we have obtained the renormalized phonon frequencies

$$\epsilon_\pm = \mu_+ + \Omega/2 \pm \sqrt{\mu_-^2 + (\Omega/2)^2}, \tag{4.5}$$

where $\mu_\pm = (\nu_+ \pm \nu_-)/2$ and $\nu_\pm = \sqrt{w_0^2 \pm \lambda^2}$. Further improvements of the model, such as calculations at finite temperatures and with the coupling of the E_g modes to a dissipative nematic mode, which is closer to what observed experimentally, are under developments [187].

For now, we can already capture the interaction effect in a phenomenological way. By taking $w_0 = 45\ \text{cm}^{-1}$, $\Omega = 0.01$, the splitting of the E_g modes can be tuned close to the experimental results by changing the coupling strength λ^2 as shown in Fig. 4.3.12. As for the doping dependence, it is yet difficult to evaluate quantitatively due to the lack of calculations at finite temperatures. However, based on the less steep temperature dependence of the splitting amplitude upon doping as shown in Fig. 4.3.9.(b), it is highly suggestive that the coupling strength decreases at a higher doping level.

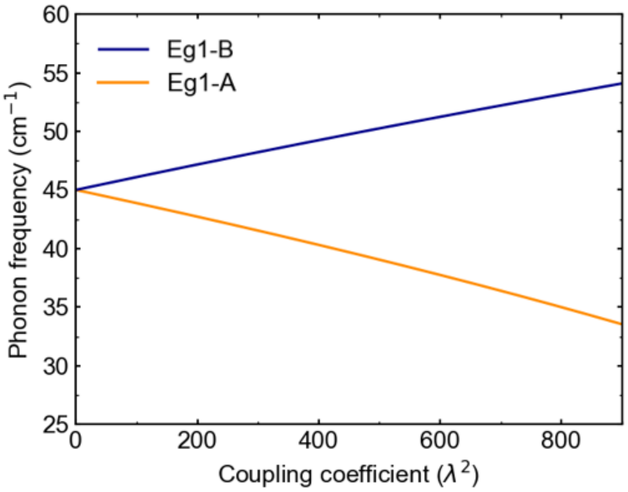

Figure 4.3.12: Calculated E_{g1} mode splitting as a function of λ^2.

In the end we present in Fig. 4.3.13 the phase diagram of $BaNi_2(As_{1-x}P_x)_2$ in which different phases and the corresponding transition temperatures are clearly marked.

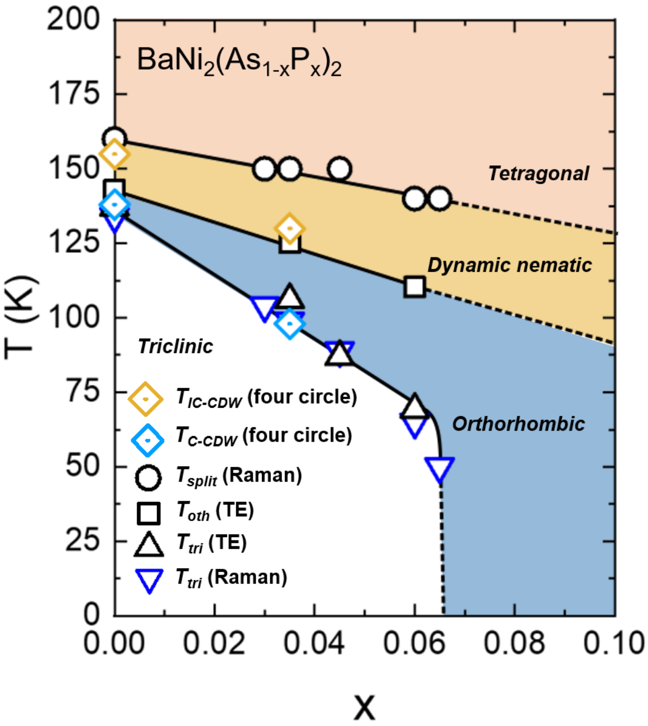

Figure 4.3.13: Phase diagram of BaNi$_2$(As$_{1-x}$P$_x$)$_2$. In the parenthesis behind each transition temperature is the associated experimental method.

Temperature and doping dependence of the A$_{1g}$ phonon mode

In the ZZ configuration, we observed a Fano lineshape of the A$_{1g}$ phonon, and such asymmetric lineshape has not been detected in the other three Raman-active modes. To explain this phenomenon, we have calculated the **q**-dependent electron-phonon coupling (EPC) strength by

$$\lambda_{v\mathbf{q}} = \frac{1}{\pi N(0)} \frac{\gamma_{v\mathbf{q}}}{w_{v\mathbf{q}}^2}, \tag{4.6}$$

where $N(0)$ denotes the density of states at the Fermi energy and $\gamma_{v\mathbf{q}}$ are the phonon linewidths with v represents different phonon branches [188]. The result is shown in the left panel of Fig. 4.3.14. The black curves are the calculated EPC-free phonon dispersions, and the red curves are EPC-modified ones. In the latter case, the dispersion curves remain qualitatively the same except for the absence of instability near (1/4 0 0), which is due to a larger smearing of the electronic states near the Fermi surface introduced manually for the calculations. Finally, the red vertical lines give the coupling strength. It is thus obvious from the figure that the A$_{1g}$ mode has the largest EPC effect among all the zone-center Raman-active phonons. The Eliashberg spectral function was also calculated according to [189]

$$\alpha^2 F(w) = \frac{1}{2\pi N(0)} \sum_{v\mathbf{q}} \delta(w - w_{v\mathbf{q}}) \frac{\gamma_{v\mathbf{q}}}{\hbar w_{v\mathbf{q}}}. \tag{4.7}$$

The results are shown in the right panel of Fig. 4.3.14, which is found to be in good agreement with that previously reported in Ref. [184].

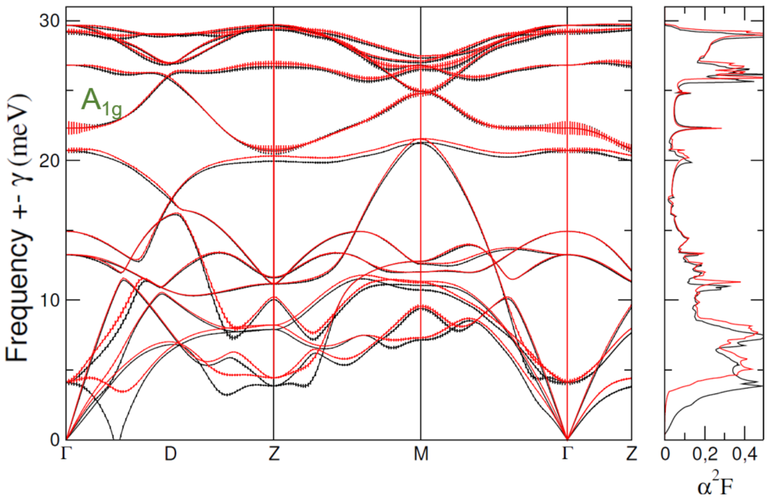

Figure 4.3.14: Left: Theoretically calculated phonon dispersions (black curves) and the modified dispersions due to electron phonon coupling (red curves). The red vertical lines indicate the coupling strength. Right: Calculated Eliashberg spectra function for both cases.

In order to understand the doping dependence of the A_{1g} phonon linewidth and lineshape, we refer to the transport measurements reported previously in Ref. [63], in which specific heat measurements on single crystals $BaNi_2(As_{1-x}P_x)_2$ from $x = 0$ to $x = 0.077$ have been performed. We show in Fig. 4.3.15 the specific heat divided by temperature as a function of T^2. The linear part is fitted by $C/T = \gamma + \beta T^2$ with γ the electronic specific heat coefficient and β the coefficient of phonon contributions from which the Debye frequency w_D is estimated. As we can see, the γ coefficient is almost independent of phosphorus doping, especially for the doping range $x = 0$ to $x = 0.049$ concerned in our experiment, indicating no large remodification of the Fermi surface upon doping. Although from these results we can only extract the electronic DOS in the triclinic phase, it was further pointed out that the DOS is not altered dramatically across the structural transition, as the calculated value from γ is around 6 eV^{-1} per formula unit, comparable to that from band calculation (3.57 eV^{-1}) for pure $BaNi_2As_2$ in the tetragonal phase [184]. We can thus speculate that the enhancement of the phonon asymmetric lineshape and larger linewidth with doping is mainly due to a stronger EPC strength. However, experimental data from which electronic DOS above the triclinic transition can be obtained are needed for a more rigorous explanation. As there are large phonon contributions to specific heat at high temperatures, other measurements such as ARPES or Hall effect on P-doped $BaNi_2As_2$ can provide valuable information.

As for the doping dependence of the phonon frequency, it seems that decreased atomic mass alone cannot explain the amplitude of hardening. If the phonon hardening is purely due to lighter phosphorus atoms, much stronger shift of A_{1g} frequency is expected between $x = 0$ and $x = 0.035$ than that between $x = 0.035$

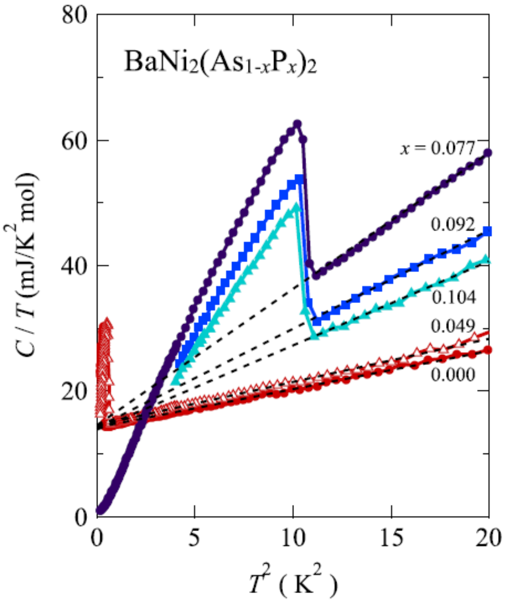

Figure 4.3.15: Specific heat divided by temperature, C/T, as a function of T^2 for $\mathrm{BaNi_2(As_{1-x}P_x)_2}$. The dashed lines are fits with $C/T = \gamma + \beta T^2$. The figure is taken from Ref. [63].

and $x = 0.045$. However, the experimental data show that between $x = 0$ and $x = 0.035$ the A_{1g} phonon frequency at 310 K increases only from 172.2 cm^{-1} to 172.93 cm^{-1}, but to a much higher value of 174.13 cm^{-1} for $x = 0.045$. Thus other degrees of freedom must be taken into account to understand this hardening effect. A similar anomalous situation has been observed in cobalt doped $\mathrm{BaFe_2As_2}$ [190], where the As mode was detected within the orthorhombic phase with in-plane polarization configuration (X′Y′) as a result of in-plane anisotropy of dielectric susceptibility tensor induced by the magnetic transition (The intensity of As mode is too small in the tetragonal phase to be detected). In their case, the phonon softens from 183 cm^{-1} to 178.5 cm^{-1} between $x = 0$ and $x = 0.045$. Although the phonon shifts in the right direction, the amplitude is too large to be accounted for by the structural effect alone, as the c lattice constant decreases by only 0.3% with doping, which would lead to a softening of less than 1 cm^{-1}. Since the strong spin-phonon coupling is ubiquitously found in the Fe-based superconductors [144, 191, 192], it was then suggested that the unusual phonon softening is due to a combined effect of the spin-phonon coupling and changes in the Fermi topology upon doping. In the case of the Ni-based compounds, however, no magnetism is present and the electronic structure at the Fermi level seems to show little doping dependence. Therefore, we strongly suspect that the hardening of the A_{1g} mode in $\mathrm{BaNi_2(As_{1-x}P_x)_2}$ is largely resulted from enhanced EPC strength upon doping.

4.4 Lattice and electronic dynamics below the triclinic transition

4.4.1 Experimental results

Dramatic renormalization of the electronic background across the triclinic transition

In the ZZ polarization configuration, significant renormalization of the electronic background across the triclinic transition was observed in the Raman response of all investigated samples (x = 0, 0.035, 0.045). Raman spectra with Raman shift up to 3625 cm^{-1} were collected to capture this phenomena. Representative spectra of the parent compounds are shown in Fig. 4.4.1.(a), in which a sudden drop in the electronic background across the triclinic transition ($T_{tri} \sim 130$ K-135 K) can be observed. The spectra are normalized at the end for clarity. In Fig. 4.4.1.(b) we plotted the spectral weight of the temperature-dependent part of the Raman response $\Delta\chi''(T) = \chi''(T) - \chi''(310K)$ of all investigated samples between 340 cm^{-1} to 3625 cm^{-1} (we chose the lower cut-off of the integration at 340 cm^{-1} to avoid contributions from the A_g phonons in the triclinic phase). We can see that similar decrease in spectral weight is also present in the doped samples, and such behavior has not been found in other polarization configurations.

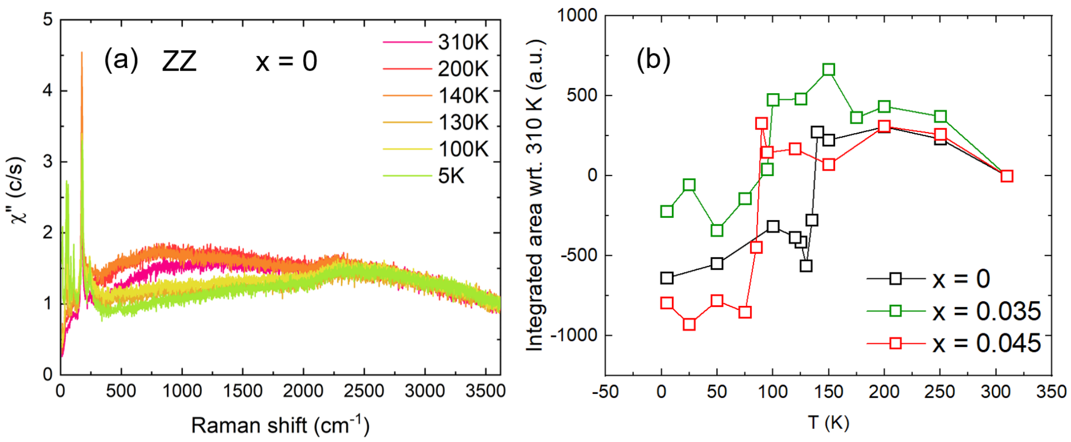

Figure 4.4.1: (a) Representative spectra of $\mathrm{BaNi_2As_2}$ in the ZZ configuration from 310 K to 5 K. The spectra are normalized at the end for clarity. (b) Integration of the temperature-dependent part of the Raman response between 340 cm^{-1} to 3625 cm^{-1} of $\mathrm{BaNi_2(As_{1-x}P_x)_2}$ with x = 0, 0.035 and 0.045. A sharp drop in spectral weight across the triclinic transition was observed in all investigated samples.

A_g phonon modes in the triclinic phase

Below the triclinic transition, we have observed surprisingly rich spectra in the low-temperature phase, which raises the question about the real symmetry of this phase.

As discussed in Sec. 4.2.3, only 6 Raman-active modes with the A_g symmetry are expected below the first-order triclinic transition. However, as can be seen in Fig. 4.4.2.(a), where representative spectra of the pure $BaNi_2As_2$ in the XX, YX, ZZ and YZ configurations at 50 K are plotted, much more modes can be resolved in the triclinic phase. The same phonon modes were also found in the doped samples as can be seen in Fig. 4.4.2.(b).

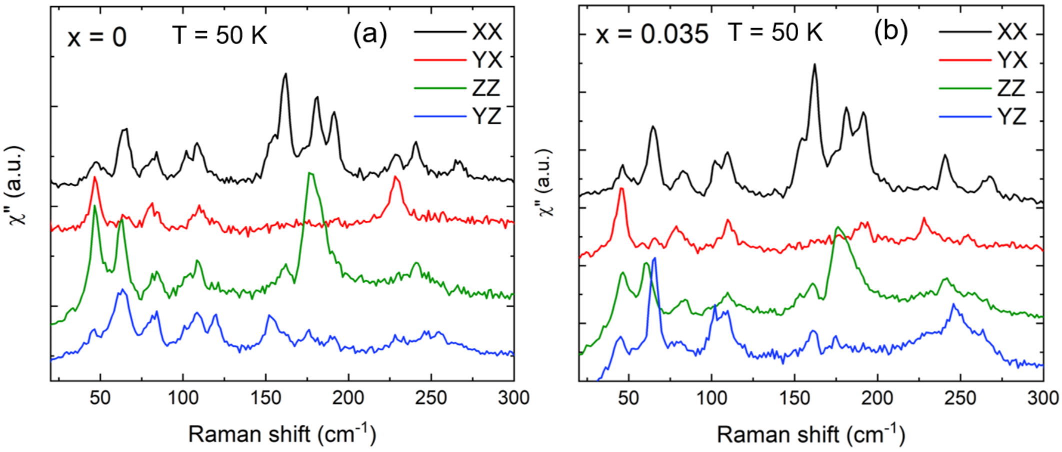

Figure 4.4.2: Raman spectra of $BaNi_2(As_{1-x}P_x)_2$ with (a) $x = 0$ and (b) $x = 0.035$ in the XX, YX, ZZ and YZ configurations at 50 K. All spectra are scaled and shifted vertically for clarity.

4.4.2 Discussions

Spectral weight loss across triclinic transition

As mentioned in Sec. 4.3.1, strong renormalization of the electronic background until relatively high energies across the triclinic transition has been detected in the ZZ configuration for all investigated samples. This decrease in spectral weight over such a broad range in $BaNi_2(As_{1-x}P_x)_2$ is different from that in the Fe-based counterpart [190], where the spectral weight redistribution occurs at low energies and is the strongest in the X′Y′ configuration, which was suggested as the result of an SDW gap opening at low frequencies. In the Ni-based systems, no CDW gap openning has ever been observed, therefore, we suspect that the reason behind this phenomenon lies in the Fermi surface reconstruction induced by the structural transition.

As previously reported in Ref. [193], the calculated band structure by local density-approximation above and below the triclinic transition shows strong remodifications of the band dispersions near the Z (Z') point and along the R (R')-X (X') direction, which has dominate contribution from the As-As $pp\sigma$ bonding and Ni-As $dp\sigma^*$ antibonding states (here the prime represents high symmetry point in the triclinic phase). These bands, while at high temperatures cross the Fermi level

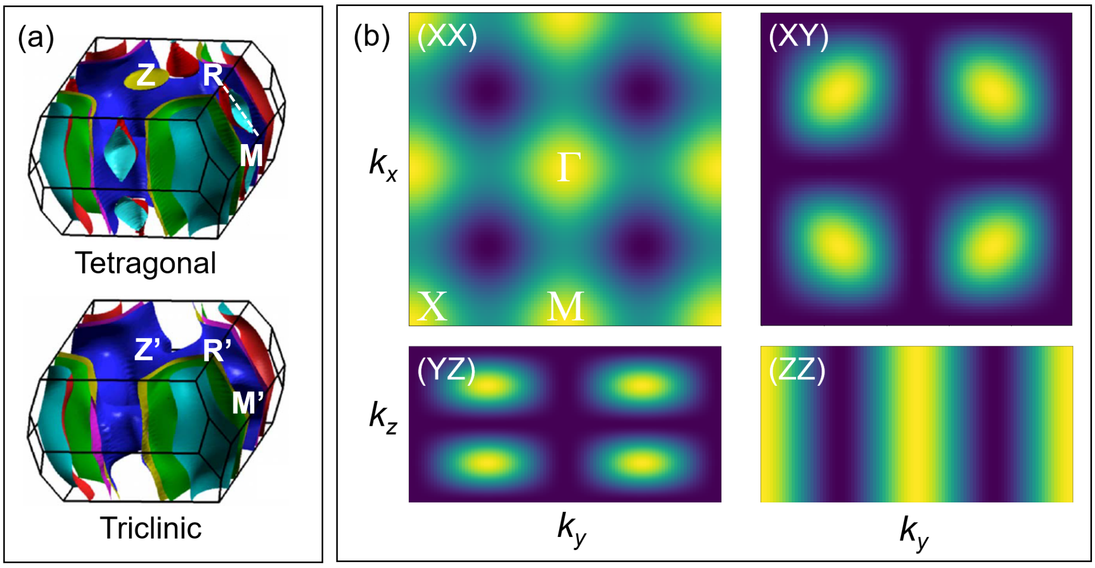

Figure 4.4.3: (a) The Fermi surface of $BaNi_2As_2$ in the tetragonal (top) and triclinic (bottom) phases, where the letters indicate high symmetry points, around which the band dispersions are significantly altered across the first-order structural transition. The figure is adapted from Ref. [193]. (b) Schematic illustrations of the weighted Raman response in different polarization configurations. The lighter the color is, the larger the magnitude is.

and form a very flat electron pocket around Z point and eight three-dimensional hole pockets along R-X line, vanish completely in the low-temperature phase as shown in Fig. 4.4.3.(a). In Fig. 4.4.3.(b) we plot the weighted Raman response in different polarization configurations which scales with $\sum_\mu \gamma_\mu^2$, where γ_μ is the Raman vertices introduced in Sec. 2.4. As we can see, different configurations selectively probe different regions of the Brillouin zone, and in this case, only XX and ZZ configurations are sensitive to the loss of several small Fermi sheets across the transition. As the eight hole pockets along R-X direction encircle a much larger area than the one electron pocket around the Z point, it is thus understandable why large spectral weight loss was only observed in the ZZ channel.

Origin of the phonon modes in the triclinic phase

As mentioned in Sec. 4.4.1, below the triclinic transition, we have observed unexpected amount of modes in the Raman spectra in both parallel and crossed polarization configurations. According to the polarization selection rules, A_g modes should only be active when the polarizations of the incident and scattered photons are parallel to each other, *i.e.*, in the XX, YY and ZZ configurations, and the reason behind this violation is likely to be the presence of multiple domains generated by the structural transition. The real problem remains with the origin of the additional modes.

To determine the exact numbers of the observed modes, we compared the Raman spectra of the pure $BaNi_2As_2$ in the XX, YX, ZZ and YZ configurations as the intensities of the modes show symmetry dependence. In total 19 modes have been detected, and they are marked by yellow dashed lines in Fig. 4.4.4.(a). Next we extracted the phonon frequencies manually (as many of them have very similar energies or very weak intensities, making rigorous fitting rather difficult) from the spectra at 100 K, and compared them with the calculated Raman-active phonon frequencies based on the structural parameters obtained by XRD measurements at 95 K. We found 6 out of the 19 modes that show good agreement with the theoretical calculations, thus naturally leaving many modes unassigned. Surprisingly, some of the unassigned modes have energies very close to that of the calculated infrared-active phonons as shown in Fig. 4.4.4.(b), in which the experimentally observed phonon frequencies are plotted together with the calculated (with and without relaxation of the internal parameter) Raman (R)-active (green) and infrared (IR)-active ones (red). The slop of the experimental data line is set to be 1, therefore, the closer are the dots to the line, the more accurate are the calculations. We can see that both calculated R- and IR-active modes fall nicely on the diagonal line. This observation thus suggests a possible violation of the rule of mutual exclusion that states no normal mode can be both Raman and infrared active when the structure possesses a center of inversion. If this is indeed the case, the real space group for the low-temperature triclinic phase of this system would be $P1$, instead of $P\bar{1}$, meaning that $BaNi_2As_2$ would be a nonmagnetic and noncentrosymmetric superconductor.

However, even with both R- and IR-active modes it is still not enough to account for all the observed modes. The unassigned modes are represented by black squares in Fig. 4.4.4.(b). On the other hand, strong CDW modulations could be an alternative origin for the additional modes. Although in $BaNi_2As_2$ no backfolding in the band structure has been observed, new modes can still be detected at the Γ point through the 'zone folding' mechanism due to a linear coupling between the electronic part of the order parameter (EOP) of the CDW modulation Δ and the phonon modes that sit on the same $\mathbf{q}$ wave vector [194, 195] in the low-temperature phase. The resulting thermodynamic potential takes the form of:

$$\phi = \phi_0 + \frac{1}{2}\alpha(T - T_{c0})\Delta^2 + \frac{1}{4}\beta\Delta^4 + \frac{\Omega_0^2}{2}\xi^2 - m\Delta\xi, \tag{4.8}$$

where ϕ_0 is the potential corresponding to the high-temperature phase, α and β (> 0) are the Ginzburg-Landau constants, ξ is generalized coordinates of ionic displacements, Ω_0 represents the bare phonon frequency, T_{c0} is the bare critical temperature without any coupling to the lattice, and finally m gives the coupling strength between the mode and Δ. If we assume small fluctuations near their equilibirum positions as $\Delta(t) = \Delta^{(0)} + x(t)$ and $\xi(t) = \xi^{(0)} + y(t)$, where $\Delta^{(0)} = \sqrt{\alpha(T_c - T)/\beta}$ and $\xi^{(0)} = \frac{m\Delta^{(0)}}{\Omega_0^2}$, the equations of motion of the EOP and the phonon mode can be derived. More detailed calculations are given in Ref. [194, 195]. Based on this model each phonon mode at $\mathbf{q}_{CDW}$ in the high-temperature phase generates one Raman-active and one infrared-active mode in the low-temperature phase, with frequencies close to $w(\mathbf{q}_{CDW})$. We are thus encouraged to check also the phonon frequencies at the CDW wave vector $\mathbf{q}$ =

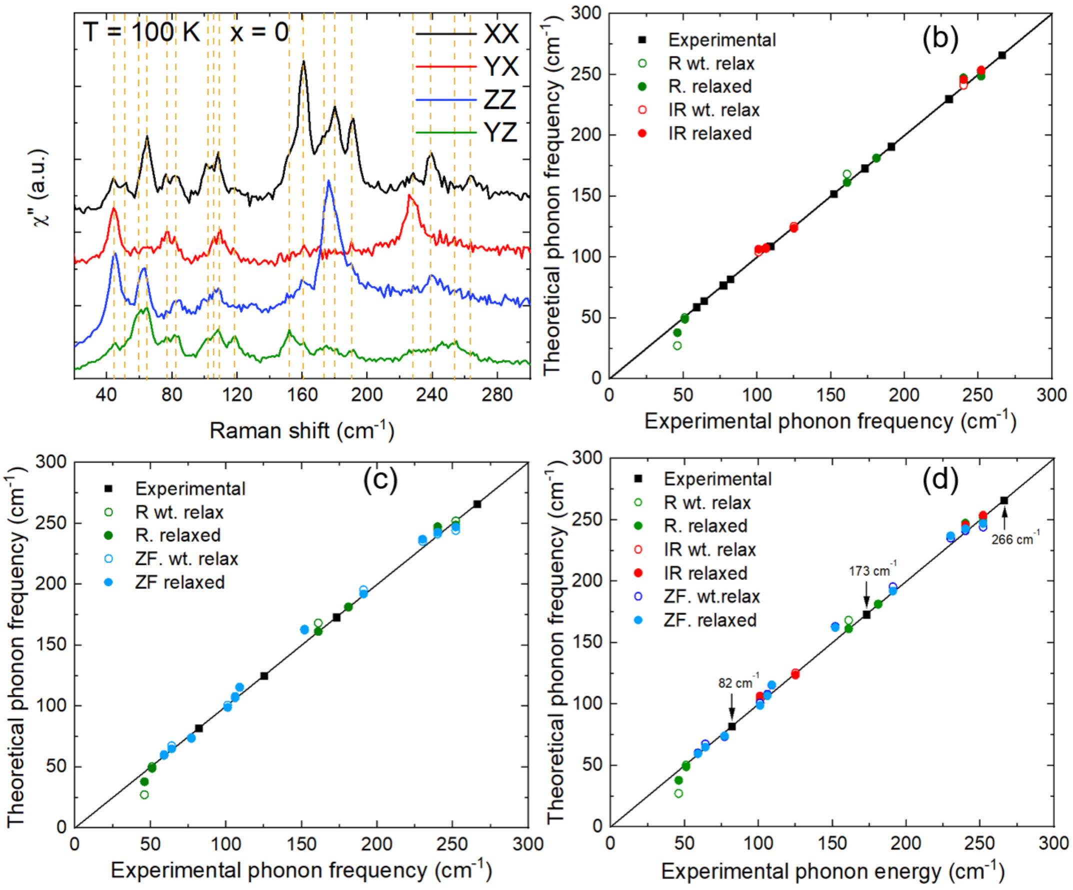

Figure 4.4.4: (a) Raman spectra of $BaNi_2As_2$ in the XX, YX, ZZ and YZ configurations at 100 K. The observed modes are marked with yellow dashed lines. (b) Comparison between experimental phonon energies with calculated ones of Raman-active (green) and infrared-active (red) modes with (solid circle) and without (open circle) relaxation of the internal parameter based on the structural parameters obtained by XRD at 95 K. The unassigned modes are represented by black squares. (c) Comparison between the measured phonon frequencies with calculated ones of Raman-active (green) modes and modes from 'zone folding' (blue). (d) Comparison between the measured phonon frequencies with all calculated ones. The slop of the experimental data line is set to be 1, therefore, the closer are the dots to the line, the more accurate are the calculations.

$(1/3, 0, 0)_{tri}$, which corrsponds approximately to $\mathbf{q} = (1/3, 0, 1/3)_{tet}$ in the tetragonal phase. The results (represented by blue circles) are plotted together with the Raman-active modes in Fig. 4.4.4.(c). As we can see, the phonon modes resulted from 'zone folding' show excellent agreement with the experimental data. However, still not all the observed modes can be accounted for.

Finally, we included all the theoretically calculated phonon frequencies in the Fig. 4.4.4.(d), and we found so far the best agreement with the experimental data. Nevertheless, we are still unable to confirm the absence of the inversion center in the low-temperature phase. On one hand, most of the calculated infrared-active modes have frequencies very close to that of the 'zone folding' modes. On the other hand, it might not be fully accurate to directly use the phonon frequencies from the calculated phonon dispersions at $\mathbf{q} = (1/3, 0, 0)_{tri}$, as there typically exists a renormalization effect due to the linear coupling that can shift the phonon energy slightly at the Γ point. Therefore, to fully tackle this problem, other experiments such as second-harmonic generation measurements are needed to provide further information. In the end, we summarized the experimentally observed phonon frequencies and all the calculated ones in Tab. 4.4.

Table 4.4: Experimental phonon frequencies at 100 K with theoretically calculated Raman-active, Infrared-active and backfolded phonon frequencies based on structural parameters obtained by XRD measurements at 95K.

Experimental results at 100 K (cm^{-1})	Calculated R-active phonon energies with (without) relaxation of internal parameter (cm^{-1})	Calculated IR-active phonon energies with (without) relaxation of internal parameter(cm^{-1})	Calculated phonon energies at $\mathbf{Q} = (\frac{1}{3}, 0, 0)_{tri}$ with (without) relaxation of internal parameter (cm^{-1})
46	37.9188 (27.2732)		
51	48.9963 (50.2902)		
59			59.5934 (60.1908)
64			65.0154 (67.5231)
77			74.1477 (73.5934)
82			
101		106.4941 (104.1255)	98.9352 (100.746)
106		107.0408 (107.6008)	106.8699 (107.9835)
109			115.746 (115.4112)
125		123.7168 (125.2981)	
152			162.4069 (163.1309)
161	161.3013 (168.2924)		
173			
181	181.4553 (181.4387)		
191			192.0797 (195.5116)
230			237.086 (235.1657)
240	247.3954 (244.4529)	245.9653 (241.2391)	242.7749 (241.3108)
252	248.7468 (252.0561)	253.6932 (253.5777)	247.1435 (244.1985)
266			

4.5 Conclusions and outlook

In summary, we have performed a detailed Raman scattering study of the lattice and electronic dynamics and their interplay as functions of temperature and doping in single crystals $BaNi_2(As_{1-x}P_x)_2$. The most important results of our work is the observation of a giant E_g phonon splitting that occurs already in the high-temperature tetragonal phase with a splitting magnitude pushing towards 30 cm^{-1} and a quasi-elastic peak in the B_{1g} Raman response associated with the electronic nematic fluctuations. The observed QEP is strongly overdamped, indicating a strong interplay with the lattice degree of freedom. More importantly, it has been demonstrated by a preliminary theoretical model that the enormous splitting of the doubly degenerate E_g mode could be well described by a strong symmetry-allowed coupling with the electronic nematic flutuations. In addition, we also suspect that this electronic nematic fluctuations are reponsible for the formation of the unidirectional IC-CDW and are the driving force of the extremely weak orthorhombic distortion above the first-order transition. The resulted orbital ordering in the orthorhombic phase in return suggests the presence of orbital nematic fluctuations.

The temperature and doping dependencies of the E_g splitting amplitude have been extracted. Upon approaching the critical phosphorus concentration x_c, where the triclinic transition is fully suppressed, the temperature dependence of the splitting amplitude is reduced, suggesting a weaker coupling with the electronic nematic fluctuations. Measurements on doped samples with $x > x_c$ are thus needed to follow the doping dependence of the coupling strength in order to verify the correlation between this coupling effect and the enhancement of superconductivity.

We have also observed strong doping dependence of the A_{1g} phonon behavior above the triclinic transition. With phosphorus substitution, enhanced asymmetric lineshape, broadened linewidth, and anomalous hardening of the A_{1g} phonon were detected, which is argued to arise from the strengthened electron-phonon coupling effect upon doping.

Across the triclinic transition, dramatic spectral weight loss of the electronic background has been detected, which can be well explained by partial renormalization of the Fermi surface induced by the phase transition. This good agreement again highlights the ability of electronic Raman scattering to selectively probe the Fermi surface.

Below the triclinic transition, unexpectedly rich spectra were collected. In total 19 modes have been observed instead of 6 as predicted by the *nuclear site group analysis*. The experimentally observed phonons can be best assigned when all calculated Raman-active, infrared-active, and ‘zone folding’ modes are taken into consideration, raising the question about the real symmetry of the low-temperature phase.

Despite the fact that further experiments are needed such as ARPES to map the electronic band structure of the high-temperature phase and second-harmonic generation to answer the question of the existence of the inversion center in the low-temperature phase, we have already demonstrated in this work that $BaNi_2As_2$

has an extremely rich phase diagram, and is a perfect playground to study strong electron-phonon coupling effect without the confusion from magnetism. Moreover, we have shown that Raman spectroscopy is an incredibly powerful tool which allows us to study simultaneously the electronic and lattice dynamics of strongly-correlated materials.

Summary

The current thesis has studied the lattice, spin and charge dynamics and the corresponding coupling effects in two novel superconducting systems, *i.e.*, CrAs and $BaNi_2(As,P)_2$, by means of Raman spectroscopy.

The lattice and magnetic excitations in single crystals CrAs were studied effectively by temperature-dependent Raman scattering. Dramatic changes of the phonon frequencies of all four A_g modes were detected across the first-order magnetostructural transition. The theoretical calculations aimed at explaining such phonon frequency renormalizations through first-principles lattice structure and dynamics calculations using the experimental lattice parameters have shown generally a better agreement with the experimental data when either ferromagnetic or antiferromagnetic order was taken into account. This observation suggests a sizable spin-phonon coupling effect in CrAs, which modifies the bond lengths and bond angles within the unit cell that are crucial for accurate predictions of phonon frequencies. In addition, an anomalous temperature dependence of the linewidth of the strongest A_g mode that shows an unusual broadening persistent into the magnetic phase down to 125 K, much lower than T_N, has been observed, which could also be explained by the strong spin-phonon coupling effect that opens additional decaying channel of the optical modes, resulting in a shorter lifetime of the phonon mode. Finally, we have also found signatures of magnetic light scattering in this system. This work has thus laid the foundation for future investigations on CrAs where hydrostatic-, uniaxial- or chemical-pressure can be used to study the impact of structural fine-tuning on the magnetic order, and more importantly, the superconductivity.

Next we have investigated the lattice and charge dynamics in $BaNi_2As_2$, a nonmagnetic analogy of the famous $BaFe_2As_2$, by detailed Raman spectroscopy as functions of both temperature and phosphorus substitution. Above the triclinic transition temperature T_{tri}, we have observed a giant E_g phonon splitting that occurs already in the high-temperature tetragonal phase and develops until the onset of the triclinic phase with a splitting magnitude pushing towards 30 cm^{-1}. Moreover, the development of a low-frequency quasi-elastic peak in the B_{1g} Raman response approaching T_{tri} has been detected, which is generally considered as the characteristic signature of electronic nematic fluctuations. Through a preliminary theoretical model that is limited to the zero-temperature case we have proven that the electronic nematic fluctuations could give rise to the enormous E_g phonon splitting by a strong symmetry-allowed coupling with the doubly degenerate phonon mode. The coupling strength seems to decrease upon phosphorus substitution, although further theoretical calculations in finite-temperature scenario are needed for confirmation. Besides the giant phonon splitting, the unidirectional nature of the IC-CDW and the extremely weak magnitude of the orthorhombic distortion that results in subsequent orbital ordering lead us to speculate that the electronic nematic fluctuations are also the driving force of these two transitions. Above the triclinic transition, we have also observed strong doping dependence of the phonon lineshape, linewidth and frequency of the A_{1g} phonon mode, which was argued to arise from a stronger electron-phonon coupling strength upon doping. Across the triclinic transition, dramatic electronic background renormalization in the ZZ configuration was detected, which could be the result of the removal of small Fermi sheets induced by the phase transition. Finally, below the triclinic transition, we have observed unexpectedly rich spectra, where in total 19 modes were detected instead of the predicted 6. Possible assignments of the additional modes could come from both 'zone folding' modes and infrared-active modes, which raises the question about the existence of the inversion center in the low-temperature phase. Although other measurements are needed, such as to map out the electronic structure of this system in the high-temperature phase and to study the real lattice symmetry of the low-temperature phase, we have shown in this work that $BaNi_2As_2$ has an extremely rich phase diagram, and provides an ideal platform to study the strong electron-phonon coupling effect without the confusion from magnetism. Last but not least, we have shown in this work that Raman spectroscopy is an incredibly powerful tool to study strongly-correlated systems. Not only can we simultaneously and selectively study lattice and electronic dynamics by simply adjusting the polarizations of the incident and scattered light, but we can also obtain valuable information of the coupling effects between different degrees of freedom which are manifested by anomalous behaviors of the optical phonon and electronic background.

Appendices

Appendix A

Experimental structural parameters

The structural parameters of CrAs single crystals at 295 K and 95 K is summarized in Tab. A.1. U_{ii} are the atomic displacement factors, and the refinement of the site occupancy factor (SOF) of Cr shows that the sample is stoichiometric within error bars. SOF of As was fixed to be 1. The experimental details to obtain such data is introduced in Sec. 3.2.1.

Table A.1: Structural parameters of CrAs single crystal at 295 K and 95 K.

		295 (K)	95 (K)
	a (Å)	5.6535 (5)	5.6095 (6)
	b (Å)	3.4737 (4)	3.5905 (5)
	c (Å)	6.2042 (6)	6.1384 (6)
Cr	x	0.0064 (2)	0.0073 (2)
	z	0.2012 (1)	0.2056 (1)
	U_{11} (Å^2)	0.0048 (5)	0.0024 (4)
	U_{22} (Å^2)	0.0107 (5)	0.0052 (5)
	U_{33} (Å^2)	0.0064 (5)	0.0044 (4)
	U_{13} (Å^2)	0.0001 (3)	-0.0004 (3)
	U_{eq} (Å^2)	0.0073 (3)	0.0040 (2)
	SOF	0.9988 (55)	0.9984 (52)
As	x	0.2022 (1)	0.2054 (1)
	z	0.5770 (1)	0.5836 (1)
	U_{11} (Å^2)	0.0075 (3)	0.0048 (3)
	U_{22} (Å^2)	0.0076 (3)	0.0026 (3)
	U_{33} (Å^2)	0.0075 (3)	0.0028 (3)
	U_{13} (Å^2)	0.0010 (3)	0.0004 (2)
	U_{eq} (Å^2)	0.0075 (2)	0.0034 (2)
$U_{12}[Cr] = U_{23}[Cr] = U_{12}[As] = U_{23}[As] = 0$			
	wR_2	4.15	3.98
	R_1	1.90	1.66

Appendix B

Raman spectra from the six facets of one single crystal CrAs

In Fig. B.0.1 the Raman spectra in XX geometry from the six facets of one CrAs single crystal is shown. Regardless of on which facet the experiment was performed, we always observed only A_g modes, in good agreement with the polarization selection rules.

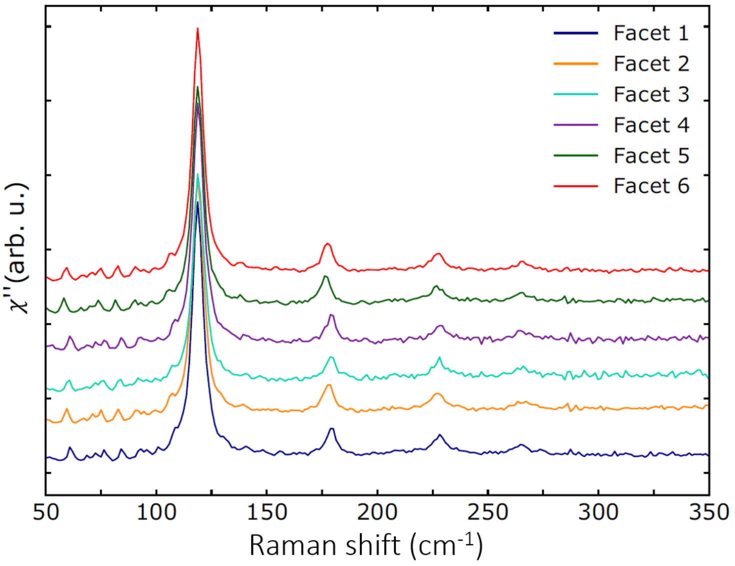

Figure B.0.1: Raman scattering in parallel polarization configuration on six facets of one CrAs single crystal at room temperature.

Appendix C

Analysis of Fleury-Loudon Hamiltonian

In Sec. 2.3 we have introduced the effective two-magnon Raman scattering operators (see Eq. 2.46). The relevant magnetic sites are marked in Fig. 3.4.5.(c). Since the incoming radiation is parallel to the crystallographic a-axis, the angle between $\mathbf{E}_{in}$ and Cr1-Cr2 or Cr1-Cr3 is very close to 90°, therefore, the projections of $\mathbf{d}_{12}$ and $\mathbf{d}_{13}$ vectors on a-axis can be neglected, which leaves us the main contribution from the scattering across the Cr1-Cr4 bond ($\mathbf{d}_{14}$).

In parallel (XX) geometry, we obtain

$$\hat{\mathcal{O}}_{\mathrm{XX}} \sim n_{14}\cos^2(\theta_{14})\mathbf{S}_1 \cdot \mathbf{S}_4, \tag{C.1}$$

where θ_{14} ($\approx 11°$) is the angle between a-axis and $\mathbf{d}_{14}$. And in crossed (XY) geometry, we get

$$\hat{\mathcal{O}}_{\mathrm{XY}} \sim n_{14}\cos(\theta_{14})\sin(\theta_{14})\cos^2(\alpha)\mathbf{S}_1 \cdot \mathbf{S}_4, \tag{C.2}$$

where $\alpha \approx 30°$ as the orientation of the measureed facet is along (011).

The ratio between the magnetic scattering intensities of these two channels can then be calculated

$$\frac{I_{\mathrm{XY}}}{I_{\mathrm{XX}}} \sim \left|\tan(\theta_{14})\cos^2(\alpha)\right|^2 \sim 2 \times 10^{-2}. \tag{C.3}$$

Such a small ratio is found consistent with the absence of any magnetic scattering signal in the crossed polarization configuration.

Appendix D

T_{split} determination for E_{g1} phonon splitting

In the Raman scattering measurements on single crystals $BaNi_2(As_{1-x}P_x)_2$ in the YZ configuration, the E_{g1} phonon broadens with decreasing temperature and gradually splits into two peaks. Due to the second-order nature of the phase transition and the relatively large temperature step (10 K), we cannot precisely pinpoint where does the splitting starts. Therefore, here we merely give our criteria on the determination of T_{split}. In Fig. D.0.1 we plot the low-energy part of the Raman response of pure $BaNi_2As_2$ in the YZ configuration. All spectra are scaled to have the same intensity and shifted horizontally for clarity. As we can see, upon cooling from 310 K to 180 K, the E_{g1} mode softens and broadens but still keeps its single peak profile. When the temperature reaches 160 K, a broad shoulder develops on the lower-energy side of the phonon as indicated by the red arrow, and the spectrum cannot be fitted with one single DHO anymore. Upon further cooling, this shoulder gets softer and higher in intensity, thus the two-peak profile becomes unambiguous. Thus we set T_{split} as the temperature where this shoulder was first observed.

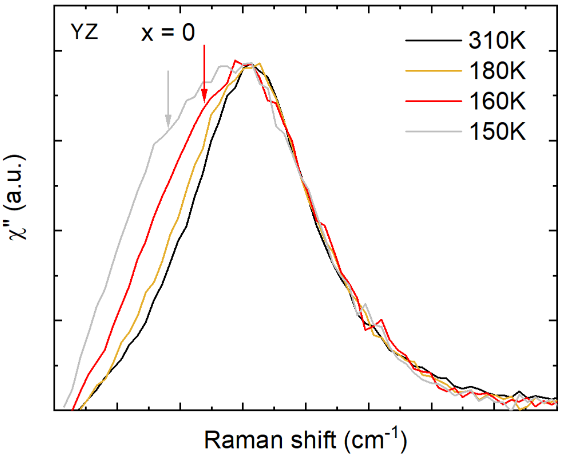

Figure D.0.1: Low-energy part of the Raman response of pure $BaNi_2As_2$ from 310 K to 150 K. All spectra are scaled to have the same intensity and shifted horizontally for clarity. The shoulder develops at the lower-energy side of the phonon upon cooling is marked with arrows.

Appendix E

Raman measurements on strained $BaNi_2As_2$ in YZ configuration

The behavior of E_g modes in pure $BaNi_2As_2$ under strain was also investigated. A relatively big crystal of $BaNi_2As_2$ was broken in half, and we glued one on a glass-fiber-reinforced plastic (GFRP) substrate that was used to detwine $BaFe_2As_2$ in thermal expansion measurements [196]. The glue was chosen to be the Devcon 5 Minute Epoxy to ensure strong adhesion. For the other half we glued it on a copper piece with only high-vacuum Apiezon N Grease as strainless reference. The mounting configuration is shown in Fig. E.0.1. The sample was required to be very flat and thin for a homogeneous strain field along the crystallographic c-axis. The width and height of the fiberglass are specifically cut to 1 mm, and the whole piece was glued on the cold finger with Apiezon to ensure good thermal contact. The solid lines in Fig. E.0.1.(a) indicate the fiber direction. The thermal expansion coefficient along this direction is larger than that perpendicular to it as shown in the insert of Fig. E.0.1.(c), thus under cooling, the sample is subjected to a symmetry-breaking strain $|\epsilon_a - \epsilon_b| = |\Delta L_{\parallel}/L_{\parallel}^{300K} - \Delta L_{\perp}/L_{\perp}^{300K}|$ with magnitude of $\sim 10^{-3}$.

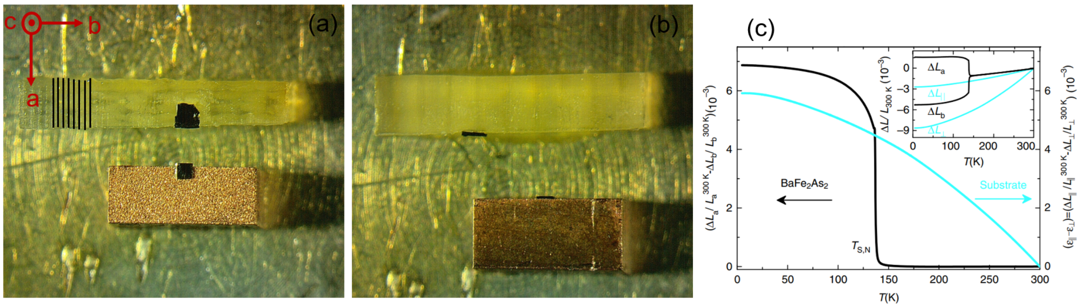

Figure E.0.1: Schematic diagram of the crystal mounting on the fiberglass and copper stage. (a) In-plane demonstration. The vertical lines indicate the direction of the fibers. (b) Edge measurement configuration for the YZ polarization. (c) The anisotropic strain of the GFRP substrate in comparison to the in-plane orthorhombic distortion of a free-standing $BaFe_2As_2$. The thermal expansion is plotted in the inset. The figure is taken from Ref. [196].

Not surprisingly we also observed E_{g1} phonon splitting for the strained $BaNi_2As_2$.

By fitting the spectrum with two DHO profiles we extracted the temperature dependence of the phonon frequencies and phonon linewidth. In Fig. E.0.2 we plot them together with that of the freestanding $BaNi_2As_2$ and that of the doped sample with $x = 0.035$. As we can see, for the phonon frequencies, at high temperatures (above 180 K), there is almost no difference between strained and non-strained $BaNi_2As_2$. With further cooling, we observed the splitting of E_{g1} mode and also the triclinic transition a bit later ($5 \sim 10$ K) in the strained sample than in the freestanding one. We also noted that the temperature dependence of the E_{g1}-B is more similar to that of the doped sample. On the other hand, for the phonon linewidth, no dramatic change has been observed, except that at high temperatures, the temperature dependence of the FWHM of the strained sample is closer to that of the doped material than that of the pure $BaNi_2As_2$.

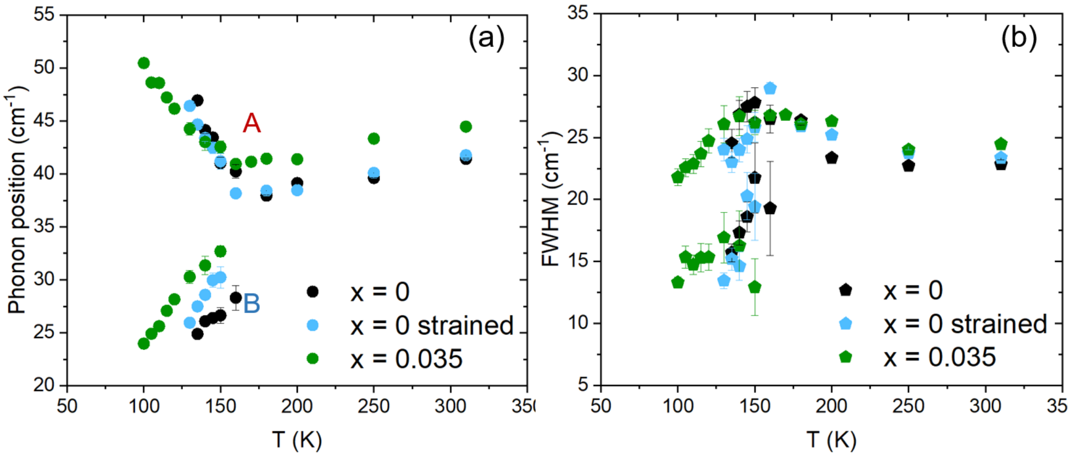

Figure E.0.2: (a) Phonon position as functions of temperature and doping for pure $BaNi_2As_2$ free standing and under strain, together with doped material with $x = 0.035$. (b) Phonon linewidth as functions of temperature and doping for the same materials.

From these experimental results, it appears that the strain effect from the fiberglass influences the system in qualitatively the same way as chemical doping. The strain field from the fiberglass is clearly not tunable and not linear with temperature [196], and the resulted effect is obviously very small. However, as a preliminary trial to probe the system response to an external strain we have certainly succeeded. To systematically apply fine-tuning of the structure, experiments with piezoelectric controlled Razorbill as used in Ref. [14] is further required.

List of Figures

Bibliography

[1] H. KAMERLINGH ONNES, Comm. Phys. Lab. Univ. Leiden **122**, 122 (1911).

[2] L. N. Cooper, Phys. Rev. **104**, 1189 (1956).

[3] J. Bardeen, L. N. Cooper, and J. R. Schrieffer, Phys. Rev. **108**, 1175 (1957).

[4] G. M. Eliashberg, Journal of Experimental and Theoretical Physics **11**, 696 (1960).

[5] M. R. Norman, Science **332**, 196 (2011).

[6] G. R. Stewart, Advances in Physics **66**, 75 (2017).

[7] F. Steglich, J. Aarts, C. D. Bredl, W. Lieke, D. Meschede, W. Franz, and H. Schäfer, Phys. Rev. Lett. **43**, 1892 (1979).

[8] G. R. Stewart, Rev. Mod. Phys. **56**, 755 (1984).

[9] D. Jérome, A. Mazaud, M. Ribault, and K. Bechgaard, Journal de Physique Lettres **41**, 95 (1980).

[10] K. Bechgaard, K. Carneiro, M. Olsen, F. B. Rasmussen, and C. S. Jacobsen, Phys. Rev. Lett. **46**, 852 (1981).

[11] K. Murata, M. Tokumoto, H. Anzai, H. Bando, G. Saito, K. Kajimura, and T. Ishiguro, Journal of the Physical Society of Japan **54**, 2084 (1985).

[12] A. M. Kini, U. Geiser, H. H. Wang, K. D. Carlson, J. M. Williams, W. K. Kwok, K. G. Vandervoort, J. E. Thompson, and D. L. a. Stupka, Inorganic Chemistry **29**, 2555 (1990).

[13] M. K. Wu, J. R. Ashburn, C. J. Torng, P. H. Hor, R. L. Meng, L. Gao, Z. J. Huang, Y. Q. Wang, and C. W. Chu, Phys. Rev. Lett. **58**, 908 (1987).

[14] H.-H. Kim, S. M. Souliou, M. E. Barber, E. Lefrançois, M. Minola, M. Tortora, R. Heid, N. Nandi, R. A. Borzi, G. Garbarino, A. Bosak, J. Porras, T. Loew, M. König, P. J. W. Moll, A. P. Mackenzie, B. Keimer, C. W. Hicks, and M. Le Tacon, Science **362**, 1040 (2018).

[15] J. Tranquada, B. Sternlieb, and J. t. Axe, Nature **375**, 561 (1995).

[16] M. Fujita, H. Goka, K. Yamada, J. M. Tranquada, and L. P. Regnault, Phys. Rev. B **70**, 104517 (2004).

[17] J. Chang, E. Blackburn, and A. t. Holmes, Nature Phys **8** (2012).

[18] G. Ghiringhelli, M. Le Tacon, M. Minola, S. Blanco-Canosa, C. Mazzoli, N. B. Brookes, G. M. De Luca, A. Frano, D. G. Hawthorn, F. He, T. Loew, M. M. Sala, D. C. Peets, M. Salluzzo, E. Schierle, R. Sutarto, G. A. Sawatzky, E. Weschke, B. Keimer, and L. Braicovich, Science **337**, 821 (2012).

[19] N. Ni, M. E. Tillman, J.-Q. Yan, A. Kracher, S. T. Hannahs, S. L. Bud'ko, and P. C. Canfield, Phys. Rev. B **78**, 214515 (2008).

[20] M. Rotter, M. Tegel, and D. Johrendt, Phys. Rev. Lett. **101**, 107006 (2008).

[21] S. Jiang, H. Xing, G. Xuan, C. Wang, Z. Ren, C. Feng, J. Dai, Z. Xu, and G. Cao, Journal of Physics: Condensed Matter **21**, 382203 (2009).

[22] M. Rotter, C. Hieke, and D. Johrendt, Phys. Rev. B **82**, 014513 (2010).

[23] J. Paglione and R. L. Greene, Nature Physics **6**, 645 (2010).

[24] A. Chubukov and P. J. Hirschfeld, Physics Today **68**, 46 (2015).

[25] Q. Huang, Y. Qiu, W. Bao, M. A. Green, J. W. Lynn, Y. C. Gasparovic, T. Wu, G. Wu, and X. H. Chen, Phys. Rev. Lett. **101**, 257003 (2008).

[26] M. A. McGuire, A. D. Christianson, A. S. Sefat, B. C. Sales, M. D. Lumsden, R. Jin, E. A. Payzant, D. Mandrus, Y. Luan, V. Keppens, V. Varadarajan, J. W. Brill, R. P. Hermann, M. T. Sougrati, F. Grandjean, and G. J. Long, Phys. Rev. B **78**, 094517 (2008).

[27] M. Tegel, M. Rotter, V. Weiß, F. M. Schappacher, R. Pöttgen, and D. Johrendt, Journal of Physics: Condensed Matter **20**, 452201 (2008).

[28] P. Chandra, P. Coleman, and A. I. Larkin, Phys. Rev. Lett. **64**, 88 (1990).

[29] C. Fang, H. Yao, W.-F. Tsai, J. Hu, and S. A. Kivelson, Phys. Rev. B **77**, 224509 (2008).

[30] C. Xu, M. Müller, and S. Sachdev, Phys. Rev. B **78**, 020501 (2008).

[31] J. Davis and P. Hirschfeld, Nature Phys **10**, 184 (2014).

[32] M. A. Tanatar, E. C. Blomberg, A. Kreyssig, M. G. Kim, N. Ni, A. Thaler, S. L. Bud'ko, P. C. Canfield, A. I. Goldman, I. I. Mazin, and R. Prozorov, Phys. Rev. B **81**, 184508 (2010).

[33] J. J. Ying, X. F. Wang, T. Wu, Z. J. Xiang, R. H. Liu, Y. J. Yan, A. F. Wang, M. Zhang, G. J. Ye, P. Cheng, J. P. Hu, and X. H. Chen, Phys. Rev. Lett. **107**, 067001 (2011).

[34] E. Blomberg, M. Tanatar, and R. t. Fernandes, Nat Commun **4** (2013).

[35] S. Ishida, M. Nakajima, T. Liang, K. Kihou, C. H. Lee, A. Iyo, H. Eisaki, T. Kakeshita, Y. Tomioka, T. Ito, and S. Uchida, Phys. Rev. Lett. **110**, 207001 (2013).

[36] S. Jiang, H. S. Jeevan, J. Dong, and P. Gegenwart, Phys. Rev. Lett. **110**, 067001 (2013).

[37] A. Dusza, A. Lucarelli, F. Pfuner, J.-H. Chu, I. R. Fisher, and L. Degiorgi, EPL (Europhysics Letters) **93**, 37002 (2011).

[38] M. Nakajima, T. Liang, S. Ishida, Y. Tomioka, K. Kihou, C. H. Lee, A. Iyo, H. Eisaki, T. Kakeshita, T. Ito, and S. Uchida, Proceedings of the National Academy of Sciences **108**, 12238 (2011).

[39] M. Nakajima, S. Ishida, Y. Tomioka, K. Kihou, C. H. Lee, A. Iyo, T. Ito, T. Kakeshita, H. Eisaki, and S. Uchida, Phys. Rev. Lett. **109**, 217003 (2012).

[40] C. Mirri, A. Dusza, S. Bastelberger, J.-H. Chu, H.-H. Kuo, I. R. Fisher, and L. Degiorgi, Phys. Rev. B **89**, 060501 (2014).

[41] C. Mirri, A. Dusza, S. Bastelberger, J.-H. Chu, H.-H. Kuo, I. R. Fisher, and L. Degiorgi, Phys. Rev. B **90**, 155125 (2014).

[42] L. W. Harriger, H. Q. Luo, M. S. Liu, C. Frost, J. P. Hu, M. R. Norman, and P. Dai, Phys. Rev. B **84**, 054544 (2011).

[43] X. Lu, J. T. Park, R. Zhang, H. Luo, A. H. Nevidomskyy, Q. Si, and P. Dai, Science **345**, 657 (2014).

[44] M. Yi, D. Lu, J.-H. Chu, J. G. Analytis, A. P. Sorini, A. F. Kemper, B. Moritz, S.-K. Mo, R. G. Moore, M. Hashimoto, W.-S. Lee, Z. Hussain, T. P. Devereaux, I. R. Fisher, and Z.-X. Shen, Proceedings of the National Academy of Sciences **108**, 6878 (2011).

[45] Y. Kim, H. Oh, C. Kim, D. Song, W. Jung, B. Kim, H. J. Choi, C. Kim, B. Lee, S. Khim, H. Kim, K. Kim, J. Hong, and Y. Kwon, Phys. Rev. B **83**, 064509 (2011).

[46] R. M. Fernandes, L. H. VanBebber, S. Bhattacharya, P. Chandra, V. Keppens, D. Mandrus, M. A. McGuire, B. C. Sales, A. S. Sefat, and J. Schmalian, Phys. Rev. Lett. **105**, 157003 (2010).

[47] M. Yoshizawa, D. Kimura, T. Chiba, S. Simayi, Y. Nakanishi, K. Kihou, C.-H. Lee, A. Iyo, H. Eisaki, M. Nakajima, and S.-i. Uchida, Journal of the Physical Society of Japan **81**, 024604 (2012).

[48] Y. Gallais, R. M. Fernandes, I. Paul, L. Chauvière, Y.-X. Yang, M.-A. Méasson, M. Cazayous, A. Sacuto, D. Colson, and A. Forget, Phys. Rev. Lett. **111**, 267001 (2013).

[49] R. M. Fernandes, E. Abrahams, and J. Schmalian, Phys. Rev. Lett. **107**, 217002 (2011).

[50] C.-C. Chen, J. Maciejko, A. P. Sorini, B. Moritz, R. R. P. Singh, and T. P. Devereaux, Phys. Rev. B **82**, 100504 (2010).

[51] W. Lv and P. Phillips, Phys. Rev. B **84**, 174512 (2011).

[52] S. Nandi, M. G. Kim, A. Kreyssig, R. M. Fernandes, D. K. Pratt, A. Thaler, N. Ni, S. L. Bud'ko, P. C. Canfield, J. Schmalian, R. J. McQueeney, and A. I. Goldman, Phys. Rev. Lett. **104**, 057006 (2010).

[53] H. Watanabe, N. Kazama, Y. Yamaguchi, and M. Ohashi, Journal of Applied Physics **40** (1969).

[54] K. Selte, Acta Chemica Scandinavica **25**, 1703 (1971).

[55] H. Boller and A. Kallel, Solid State Communications **9**, 1699 (1971).

[56] A. Kallel, H. Boller, and E. Bertaut, Journal of Physics and Chemistry of Solids **35**, 1139 (1974).

[57] W. Wu, J. Cheng, K. Matsubayashi, P. Kong, F. Lin, C. Jin, N. Wang, Y. Uwatoko, and J. Luo, Nature Communications **5** (2014).

[58] H. Kotegawa, S. Nakahara, H. Tou, and H. Sugawara, Journal of the Physical Society of Japan **83**, 093702 (2014).

[59] M. Matsuda, F. K. Lin, R. Yu, J.-G. Cheng, W. Wu, J. P. Sun, J. H. Zhang, P. J. Sun, K. Matsubayashi, T. Miyake, T. Kato, J.-Q. Yan, M. B. Stone, Q. Si, J. L. Luo, and Y. Uwatoko, Phys. Rev. X **8**, 031017 (2018).

[60] F. Ronning, N. Kurita, E. D. Bauer, B. L. Scott, T. Park, T. Klimczuk, R. Movshovich, and J. D. Thompson, Journal of Physics: Condensed Matter **20**, 342203 (2008).

[61] K. Kothapalli, F. Ronning, E. D. Bauer, A. J. Schultz, and H. Nakotte, Journal of Physics: Conference Series **251**, 012010 (2010).

[62] S. Lee, G. De La Penã, S. Sun, M. Mitrano, Y. Fang, H. Jang, J. Lee, C. Eckberg, D. Campbell, J. Collini, J. Paglione, F. De Groot, and P. Abbamonte, Physical Review Letters **122** (2019).

[63] K. Kudo, M. Takasuga, Y. Okamoto, Z. Hiroi, and M. Nohara, Physical Review Letters **109** (2012).

[64] M. Merz, L. Wang, T. Wolf, P. Nagel, C. Meingast, and S. Schuppler, submitted (2020).

[65] F. Kretzschmar, *Nematic Fluctuations, Fermiology and the Pairing Potential in Iron-based Superconductors*, Ph.D. thesis, Technische Universität München (2015).

[66] L. D. Landau and E. M. Lifshitz, *Electrodynamics of Continuous Media* (Pergamon, Oxford, 1960).

[67] T. P. Devereaux and R. Hackl, Rev. Mod. Phys. **79**, 175 (2007).

[68] W. Hayes and R. Loudon, *Scattering og light by crystals* (JOHN WILEY SONS, 1978).

[69] D. A. Long, *The Raman Effect* (JOHN WILEY SONS, 2002).

[70] M. Cardona and G. Güntherodt, *Light Scattering in Solids II* (Springer, 1982).

[71] M. Cardona, *Raman Scattering in Materials Science* (Springer, 2000).

[72] S.-M. Souliou, *High Pressure Study of High-Temperature Superconductors*, Ph.D. thesis, Universität Stuttgart (2014).

[73] Y. Um, *A Study of Lattice Dynamics in Iron-based Superconductors by Inelastic Light Scattering*, Ph.D. thesis, Universität Stuttgart (2013).

[74] M. H. Bakr, *Electronic and Phononic Raman Scattering in Twin-Free YBa2Cu3O6+x*, Ph.D. thesis, Universität Stuttgart (2010).

[75] G. Lucazeau, Journal of Raman Spectroscopy **34**, 478 (2003).

[76] Y. P and M. Cardona, *Fundamentals of Semiconductors* (Springer, 2005).

[77] D. Tuschel, Spectroscopy **29**, 14 (2014).

[78] M. Hepting, *Ordering phenomena in nickelate heterostructures studies by elastic and inelastic phonon scattering*, Ph.D. thesis, Universität Stuttgart (2016).

[79] D. L. Rousseau, R. P. Bauman, and S. P. S. Porto, Journal of Raman Spectroscopy **10**, 253 (1981).

[80] T. Strohm, *Electronic Raman scattering in high-temperature superconductors*, Ph.D. thesis, Universität Stuttgart (1999).

[81] J. Menéndez and M. Cardona, Phys. Rev. B **29**, 2051 (1984).

[82] P. G. Klemens, Phys. Rev. **148**, 845 (1966).

[83] R. A. Cowley, Reports on Progress in Physics **31**, 123 (1968).

[84] U. Fano, Phys. Rev. **124**, 1866 (1961).

[85] H. Kuzmany, *Solid-State Spectroscopy* (Springer, 2009).

[86] P. A. Fleury and R. Loudon, Phys. Rev. **166**, 514 (1968).

[87] C. Kittel, *Quantum theory of solids* (New York: Wiley, 1963).

[88] M. I. K. F. G. Bass, Journal of Experimental and Theoretical Physics **10**, 986 (1960).

[89] R. Elliott and R. Loudon, Physics Letters **3**, 189 (1963).

[90] P. A. Fleury, S. P. S. Porto, L. E. Cheesman, and H. J. Guggenheim, Phys. Rev. Lett. **17**, 84 (1966).

[91] E. Meloche, M. G. Cottam, V. P. Gnezdilov, and D. J. Lockwood, Phys. Rev. B **81**, 024426 (2010).

[92] S. L. Gleason, T. Byrum, Y. Gim, A. Thaler, P. Abbamonte, G. J. MacDougall, L. W. Martin, H. D. Zhou, and S. L. Cooper, Phys. Rev. B **89**, 134402 (2014).

[93] H. Gretarsson, J. Sauceda, N. H. Sung, M. Höppner, M. Minola, B. J. Kim, B. Keimer, and M. Le Tacon, Phys. Rev. B **96**, 115138 (2017).

[94] P. Lemmens, G. Güntherodt, and C. Gros, Physics Reports **375**, 1 (2003).

[95] Y. Tanabe, T. Moriya, and S. Sugano, Phys. Rev. Lett. **15**, 1023 (1965).

[96] P. A. Fleury, S. P. S. Porto, and R. Loudon, Phys. Rev. Lett. **18**, 658 (1967).

[97] T. Moriya, Journal of Applied Physics **39**, 1042 (1968).

[98] C.-C. Chen, C. J. Jia, A. F. Kemper, R. R. P. Singh, and T. P. Devereaux, Physical Review Letters **106** (2011).

[99] V. G. Ivanov, M. V. Abrashev, N. D. Todorov, V. Tomov, R. P. Nikolova, A. P. Litvinchuk, and M. N. Iliev, Phys. Rev. B **88**, 094301 (2013).

[100] K. B. Lyons, P. A. Fleury, J. P. Remeika, A. S. Cooper, and T. J. Negran, Phys. Rev. B **37**, 2353 (1988).

[101] H. Gretarsson, N. H. Sung, M. Höppner, B. J. Kim, B. Keimer, and M. Le Tacon, Phys. Rev. Lett. **116**, 136401 (2016).

[102] N. W. Ashcroft and N. D. Mermin, *Solid State Physics* (Springer, 1976).

[103] T. P. Devereaux and D. Einzel, Phys. Rev. B **51**, 16336 (1995).

[104] M. V. Klein and S. B. Dierker, Phys. Rev. B **29**, 4976 (1984).

[105] H. Monien and A. Zawadowski, Phys. Rev. B **41**, 8798 (1990).

[106] B. S. Shastry and B. I. Shraiman, International Journal of Modern Physics B **05**, 365 (1991).

[107] A. Yamanaka, T. Kimura, F. Minami, K. Inoue, and S. Takekawa, Japanese Journal of Applied Physics **27**, L1902 (1988).

[108] T. P. Devereaux, D. Einzel, B. Stadlober, R. Hackl, D. H. Leach, and J. J. Neumeier, Phys. Rev. Lett. **72**, 396 (1994).

[109] X. K. Chen, J. C. Irwin, H. J. Trodahl, T. Kimura, and K. Kishio, Phys. Rev. Lett. **73**, 3290 (1994).

[110] M. Kang, G. Blumberg, M. V. Klein, and N. N. Kolesnikov, Phys. Rev. B **56**, R11427 (1997).

[111] G. Blumberg, M. V. Klein, and S.-W. Cheong, Phys. Rev. Lett. **80**, 564 (1998).

[112] A. Sacuto, J. Cayssol, P. Monod, and D. Colson, Phys. Rev. B **61**, 7122 (2000).

[113] Y. Gallais, A. Sacuto, and D. Colson, Physica C: Superconductivity **408-410**, 785–788 (2004).

[114] Y. Gallais and I. Paul, Comptes Rendus Physique **17**, 113 (2016), iron-based superconductors / Supraconducteurs à base de fer.

[115] H. Yamase and R. Zeyher, Phys. Rev. B **88**, 125120 (2013).

[116] H. Kontani and Y. Yamakawa, Physical review letters **113**, 047001 (2014).

[117] K. F, B. T, and K. U. *et al*, Nature Phys **12** (2016).

[118] P. Massat, D. Farina, I. Paul, S. Karlsson, P. Strobel, P. Toulemonde, M.-A. Méasson, M. Cazayous, A. Sacuto, S. Kasahara, and *et al.*, Proceedings of the National Academy of Sciences **113**, 9177–9181 (2016).

[119] J.-H. Chu, H.-H. Kuo, J. G. Analytis, and I. R. Fisher, Science **337**, 710 (2012).

[120] G. K. Wertheim, M. A. Butler, K. W. West, and D. N. E. Buchanan, Review of Scientific Instruments **45** (1974).

[121] T. Suzuki and H. Ido, Journal of Applied Physics **73** (1993).

[122] A. G. Christy, Acta Crystallographica Section B **51**, 753 (1995).

[123] R. Blachnik, G. Kudermann, F. Grønvold, A. Alles, B. Falk, and E. Westrum, The Journal of Chemical Thermodynamics **10**, 507 (1978).

[124] L. Keller, J. S. White, M. Frontzek, P. Babkevich, M. A. Susner, Z. C. Sims, A. S. Sefat, H. M. Rønnow, and C. Rüegg, Physical Review B **91** (2015).

[125] Y. Shen, Q. Wang, Y. Hao, B. Pan, Y. Feng, Q. Huang, L. W. Harriger, J. B. Leao, Y. Zhao, R. M. Chisnell, J. W. Lynn, H. Cao, J. Hu, and J. Zhao, Phys. Rev. B **93**, 060503 (2016).

[126] É. A. Zavadskiĭ and I. A. Sibarova, Soviet Journal of Experimental and Theoretical Physics **51**, 542 (1980).

[127] K. Jin, N. Butch, and K. t. Kirshenbaum, Nature **476** (2011).

[128] G. M. Zhang, Y. H. Su, Z. Y. Lu, Z. Y. Weng, D. H. Lee, and T. Xiang, EPL (Europhysics Letters) **86**, 37006 (2009).

[129] H. Kotegawa, S. Nakahara, R. Akamatsu, H. Tou, H. Sugawara, and H. Harima, Phys. Rev. Lett. **114**, 117002 (2015).

[130] L. C. Hebel and C. P. Slichter, Phys. Rev. **113**, 1504 (1959).

[131] E. I. t. Khasanov R., Guguchia Z., Sci Rep **5** (2015).

[132] Y. Z. t. Wu W, Zhang X, SCIENCE CHINA Physics, Mechanics and Astronomy **53**, 1207 (2010).

[133] T. Moriya, *Spin fluctuations in itinerant electron magnetism* (Springer, 1985).

[134] T. Moriya and T. Takimoto, J. Phys. Soc. Jpn. **64**, 960 (1995).

[135] Y. K. t. Niu Q., Yu W., Nature Communications **8** (2017).

[136] S. G. Louie, K.-M. Ho, and M. L. Cohen, Phys. Rev. B **19**, 1774 (1979).

[137] R. Heid and K.-P. Bohnen, Phys. Rev. B **60**, R3709 (1999).

[138] J. P. Perdew, K. Burke, and M. Ernzerhof, Phys. Rev. Lett. **77**, 3865 (1996).

[139] S. Baroni, S. de Gironcoli, A. Dal Corso, and P. Giannozzi, Rev. Mod. Phys. **73**, 515 (2001).

[140] K. Sen, Y. Yao, R. Heid, A. Omoumi, F. Hardy, K. Willa, M. Merz, A. A. Haghighirad, and M. Le Tacon, Phys. Rev. B **100**, 104301 (2019).

[141] J. M. Ziman, *Principles of the theory of solids* (Cambridge Unversity Press, 1972).

[142] V. Gnezdilov, Y. G. Pashkevich, P. Lemmens, D. Wulferding, T. Shevtsova, A. Gusev, D. Chareev, and A. Vasiliev, Phys. Rev. B **87**, 144508 (2013).

[143] C. Autieri and C. Noce, Philosophical Magazine **97**, 3276 (2017).

[144] D. Reznik, K. Lokshin, D. C. Mitchell, D. Parshall, W. Dmowski, D. Lamago, R. Heid, K.-P. Bohnen, A. S. Sefat, M. A. McGuire, B. C. Sales, D. G. Mandrus, A. Subedi, D. J. Singh, A. Alatas, M. H. Upton, A. H. Said, A. Cunsolo, Y. Shvyd'ko, and T. Egami, Phys. Rev. B **80**, 214534 (2009).

[145] T. Yildirim, Physica C: Superconductivity **469**, 425 (2009), superconductivity in Iron-Pnictides.

[146] J. Łażewski, P. Piekarz, J. Toboła, B. Wiendlocha, P. T. Jochym, M. Sternik, and K. Parlinski, Phys. Rev. Lett. **104**, 147205 (2010).

[147] W. Z. Hu, J. Dong, G. Li, Z. Li, P. Zheng, G. F. Chen, J. L. Luo, and N. L. Wang, Phys. Rev. Lett. **101**, 257005 (2008).

[148] M. Rahlenbeck, G. L. Sun, D. L. Sun, C. T. Lin, B. Keimer, and C. Ulrich, Phys. Rev. B **80**, 064509 (2009).

[149] E. Granado, A. García, J. A. Sanjurjo, C. Rettori, I. Torriani, F. Prado, R. D. Sánchez, A. Caneiro, and S. B. Oseroff, Phys. Rev. B **60**, 11879 (1999).

[150] J. Laverdière, S. Jandl, A. A. Mukhin, V. Y. Ivanov, V. G. Ivanov, and M. N. Iliev, Phys. Rev. B **73**, 214301 (2006).

[151] S. Issing, A. Pimenov, V. Y. Ivanov, A. A. Mukhin, and J. Geurts, Phys. Rev. B **81**, 024304 (2010).

[152] R. Gupta, G. V. Pai, A. K. Sood, T. V. Ramakrishnan, and C. N. R. Rao, Europhysics Letters (EPL) **58**, 778 (2002).

[153] V. S. Bhadram, B. Rajeswaran, A. Sundaresan, and C. Narayana, EPL (Europhysics Letters) **101**, 17008 (2013).

[154] M. El Amrani, M. Zaghrioui, V. Ta Phuoc, F. Gervais, and N. E. Massa, Journal of Magnetism and Magnetic Materials **361**, 1 (2014).

[155] C. M. Canali and S. M. Girvin, Phys. Rev. B **45**, 7127 (1992).

[156] E. Fawcett, Rev. Mod. Phys. **60**, 209 (1988).

[157] S. Toth and B. Lake, Journal of Physics: Condensed Matter **27**, 166002 (2015).

[158] A. V. Chubukov, Zh. Eksp. Teor. Fiz **85**, 1319 (1983).

[159] T. Nguyen, L. Sandilands, and C. t. Sohn, Nat Commun **8** (2017).

[160] M. E. Valentine, S. Koohpayeh, M. Mourigal, T. M. McQueen, C. Broholm, N. Drichko, S. E. Dutton, R. J. Cava, T. Birol, H. Das, and C. J. Fennie, Phys. Rev. B **91**, 144411 (2015).

[161] M. N. Iliev, A. P. Litvinchuk, V. G. Hadjiev, M. M. Gospodinov, V. Skumryev, and E. Ressouche, Phys. Rev. B **81**, 024302 (2010).

[162] N. Perkins and W. Brenig, Phys. Rev. B **77**, 174412 (2008).

[163] N. B. Perkins, G.-W. Chern, and W. Brenig, Phys. Rev. B **87**, 174423 (2013).

[164] Y. Kamihara, T. Watanabe, M. Hirano, and H. Hosono, Journal of the American Chemical Society **130**, 3296 (2008).

[165] R. Zhi-An, L. Wei, Y. Jie, Y. Wei, S. Xiao-Li, L. Zheng-Cai, C. Guang-Can, D. Xiao-Li, S. Li-Ling, Z. Fang, and Z. Zhong-Xian, Chinese Physics Letters **25**, 2215-2216 (2008).

[166] X. Chen, T. Wu, and G. t. Wu, Nature Phys **453** (2008).

[167] G. F. Chen, Z. Li, D. Wu, G. Li, W. Z. Hu, J. Dong, P. Zheng, J. L. Luo, and N. L. Wang, Phys. Rev. Lett. **100**, 247002 (2008).

[168] T. Park, E. Park, H. Lee, T. Klimczuk, E. D. Bauer, F. Ronning, and J. D. Thompson, Journal of Physics: Condensed Matter **20**, 322204 (2008).

[169] P. L. Alireza, Y. T. C. Ko, J. Gillett, C. M. Petrone, J. M. Cole, G. G. Lonzarich, and S. E. Sebastian, Journal of Physics: Condensed Matter **21**, 012208 (2008).

[170] T. Terashima, M. Kimata, H. Satsukawa, A. Harada, K. Hazama, S. Uji, H. S. Suzuki, T. Matsumoto, and K. Murata, Journal of the Physical Society of Japan **78**, 083701 (2009).

[171] L. F. Feiner, J. H. Jefferson, and R. Raimondi, Phys. Rev. B **53**, 8751 (1996).

[172] P. A. Lee, N. Nagaosa, and X.-G. Wen, Rev. Mod. Phys. **78**, 17 (2006).

[173] V. Cvetkovic and Z. Tesanovic, Phys. Rev. B **80**, 024512 (2009).

[174] V. Cvetkovic and Z. Tesanovic, EPL (Europhysics Letters) **85**, 37002 (2009).

[175] L. J. Li, Y. K. Luo, Q. B. Wang, H. Chen, Z. Ren, Q. Tao, Y. K. Li, X. Lin, M. He, Z. W. Zhu, G. H. Cao, and Z. A. Xu, New Journal of Physics **11**, 025008 (2009).

[176] A. Mani, N. Ghosh, S. Paulraj, A. Bharathi, and C. S. Sundar, EPL (Europhysics Letters) **87**, 17004 (2009).

[177] P. C. Canfield and S. L. Bud'ko, Annual Review of Condensed Matter Physics **1**, 27 (2010).

[178] L. Chauvière, Y. Gallais, M. Cazayous, A. Sacuto, M. A. Méasson, D. Colson, and A. Forget, Phys. Rev. B **80**, 094504 (2009).

[179] A. S. Sefat, M. A. McGuire, R. Jin, B. C. Sales, D. Mandrus, F. Ronning, E. D. Bauer, and Y. Mozharivskyj, Physical Review B **79** (2009).

[180] C. Eckberg, D. J. Campbell, and T. t. Metz, Nat. Phys. **16**, 346 (2020).

[181] T. Park, H. Lee, E. D. Bauer, J. D. Thompson, and F. Ronning, Journal of Physics: Conference Series **200**, 012155 (2010).

[182] J. P. Carbotte, Rev. Mod. Phys. **62**, 1027 (1990).

[183] Z. Hiroi, S. Yonezawa, Y. Nagao, and J. Yamaura, Phys. Rev. B **76**, 014523 (2007).

[184] A. P. Subedi and D. J. Singh, Physical Review B **78** (2008).

[185] T. L. Lacmann, "Elastic tuning of properties of 122 ni-based superconductors," (2020).

[186] R. M. Martin, Phys. Rev. B **1**, 4005 (1970).

[187] J. Schmalian and W. Roland, *unpublished theoretical calculations* (2020).

[188] L. Boeri, O. Dolgov, and A. Golubov, Physical review letters **101**, 026403 (2008).

[189] A. Durajski, Sci Rep **6** (2016).

[190] L. Chauvière, Y. Gallais, M. Cazayous, M. A. Méasson, A. Sacuto, D. Colson, and A. Forget, Physical Review B **84** (2011).

[191] M. Le Tacon, T. R. Forrest, C. Rüegg, A. Bosak, A. C. Walters, R. Mittal, H. M. Rønnow, N. D. Zhigadlo, S. Katrych, J. Karpinski, J. P. Hill, M. Krisch, and D. F. McMorrow, Phys. Rev. B **80**, 220504 (2009).

[192] M. Zbiri, R. Mittal, S. Rols, Y. Su, Y. Xiao, H. Schober, S. L. Chaplot, M. R. Johnson, T. Chatterji, Y. Inoue, S. Matsuishi, H. Hosono, and T. Brueckel, Journal of Physics: Condensed Matter **22**, 315701 (2010).

[193] Z. Chen, G. Xu, W. Hu, X. Zhang, P. Zheng, G. Chen, J. Luo, Z. Fang, and N. Wang, Physical Review B **80**, 094506 (2009).

[194] M. J. Rice, Phys. Rev. Lett. **37**, 36 (1976).

[195] H. Schäfer, V. V. Kabanov, M. Beyer, K. Biljakovic, and J. Demsar, Phys. Rev. Lett. **105**, 066402 (2010).

[196] M. He, L. Wang, and F. t. Ahn, Nat Commun **8** (2017).

Ackowledgements

This thesis would not have been possible without the help and support of so many people. Here I would like to express my gratitude.

First and foremost I would like to express my deepest gratitude to Prof. Matthieu Le Tacon for giving me the chance of becoming a member of his group and carry out my doctorate study in such a scientifically inspiring environment. With a previous background in Materials Science, my understanding of some physics problems is sometimes very limited, but Matthieu has shown nothing but patience and trust in me. Despite his busy schedule, he would always find time to discuss with me about the work, and offer me valuable advice on how to improve the experiment. For that I am truly grateful.

I sincerely thank Prof. Jörg Schmalian, Dr. Rolf. Heid, and Dr. Roland Willa, who, as marvelous theoreticians, have helped me so much in the interpretation of the experimental results.

I deeply thank Dr. Kaushik Sen for introducing me to Raman spectroscopy and every little part in the Raman lab, and Dr. Michaela Sofia Souliou for her help in the high pressure studies. Most importantly, I thank their day-to-day guidance throughout my doctorate study.

I am thankful to Dr. Christoph Meingast, Dr. Amir Haghighirad, Dr. Frederic Hardy, Dr. Michael Merz, Dr. Kristin Willa, Dr. Robert Eder, Dr. Kai Grube, Tom Lacmann, Anahita Omoumi for their professional help for this thesis work.

Many thanks to our patient secretary Carmen Dörflinger for her frequent help. I thank the technicians of the workshop for their great help with their skills and rich experience during this thesis work.

It has also been a great pleasure for me to work with other members of IQMT: Dr. Anna Böhmer, Dr. Dirk Fuchs, Dr. Frank Weber, Dr. Stefan Schuppler, Dr. Peter Nagel, Dr. Roland Schäfer, Dr. Paul Waymouth Wiecki, Dr. Roland Hott, Dr. David Hunger, Dr. Mehdi Frachet, Fatemeh Ghorbani, Daniel Arnold, Amir Ghiami, Arun Kumar Jaiswal, Lars Lauke. Thank you all for your scientific collaboration and pleasant company. Special thanks to Dr. Marie-Aude Measson and Dr. Amit Pawbake from the Néel Institute in Grenoble for their warm welcome and valuable help during our staying.

Last but not least, I deeply thank my parents for their love and support for all the years.